

Cite this: *Chem. Soc. Rev.*, 2012, **41**, 5313–5360[www.rsc.org/csr](http://www.rsc.org/csr)

## CRITICAL REVIEW

## High surface area crystalline titanium dioxide: potential and limits in electrochemical energy storage and catalysis†

T. Fröschl,<sup>a</sup> U. Hörmann,<sup>b</sup> P. Kubiak,<sup>c</sup> G. Kučerová,<sup>b</sup> M. Pfanzelt,<sup>c</sup> C. K. Weiss,<sup>d</sup> R. J. Behm,<sup>b</sup> N. Hüsing,<sup>a</sup> U. Kaiser,<sup>b</sup> K. Landfester<sup>d</sup> and M. Wohlfahrt-Mehrens<sup>c</sup>

Received 16th January 2012

DOI: 10.1039/c2cs35013k

Titanium dioxide is one of the most intensely studied oxides due to its interesting electrochemical and photocatalytic properties and it is widely applied, for example in photocatalysis, electrochemical energy storage, in white pigments, as support in catalysis, *etc.* Common synthesis methods of titanium dioxide typically require a high temperature step to crystallize the amorphous material into one of the polymorphs of titania, *e.g.* anatase, brookite and rutile, thus resulting in larger particles and mostly non-porous materials. Only recently, low temperature solution-based protocols gave access to crystalline titania with higher degree of control over the formed polymorph and its intra- or interparticle porosity. The present work critically reviews the formation of crystalline nanoscale titania particles *via* solution-based approaches without thermal treatment, with special focus on the resulting polymorphs, crystal morphology, surface area, and particle dimensions. Special emphasis is given to sol–gel processes *via* glycolated precursor molecules as well as the miniemulsion technique. The functional properties of these materials and the differences to chemically identical, non-porous materials are illustrated using heterogeneous catalysis and electrochemical energy storage (battery materials) as example.

<sup>a</sup> Paris-Lodron University Salzburg, Hellbrunner Str. 34, A-5020 Salzburg, Austria

<sup>b</sup> Ulm University, D-89069 Ulm, Germany

<sup>c</sup> ZSW – Zentrum für Sonnenenergie und Wasserstoff Forschung, Helmholtzstraße 8, D-89081 Ulm, Germany

<sup>d</sup> Max-Planck-Institut für Polymerforschung, Ackermannweg 10, D-55128 Mainz, Germany

† Part of a web theme on the topic of nanomaterials (Deutsche Forschungsgemeinschaft SPP1181/Nanomaterials program).

## 1. Introduction

Metal oxides are of high importance and the most commonly used catalysts or catalyst supports in heterogeneous catalysis because of their interesting acid–base and redox properties.<sup>1</sup> Among the different metal oxides, titanium dioxide plays one of the most prominent roles due to its promising electrochemical properties, high photocatalytic activity, high chemical



R. J. Behm

R. Jürgen Behm is a Professor of Physical Chemistry at Ulm University, Germany. After studying chemistry at the Ludwig-Maximilians-University (LMU) in Munich, he received his PhD in the area of surface science. Following a post-doc at the IBM Research Laboratory in San José, USA, he held positions at different research and academic institutions and obtained his habilitation in Physical Chemistry at the LMU. In 1992, he assumed his current position, heading the

Institute of Surface Chemistry and Catalysis. His research interests focus on the mechanistic understanding of catalytic/electrocatalytic surface reactions on the molecular scale. In 2012, he was appointed Fellow of the International Society of Electrochemistry.



N. Hüsing

Nicola Hüsing is a Professor of Materials Chemistry at the Paris-Lodron University of Salzburg, Austria. After receiving her PhD in chemistry in 1997 from the University of Würzburg, she was awarded a post-doctoral fellowship with C. J. Brinker (Albuquerque, USA) on nanostructured thin films. Returning to the Vienna University of Technology she gained her lecturing qualification in 2003, became a full professor of Inorganic Chemistry at the University

of Ulm in 2004 and was appointed as a professor for materials chemistry in Salzburg in 2010. In 2011 she was elected as a corresponding member of the Austrian Academy of Science.

stability and being commercially available and non-toxic.<sup>2,3</sup> It has been extensively used in a variety of applications, such as white pigment in paints, cosmetics or toothpastes,<sup>4</sup> in photocatalysis,<sup>2,5</sup> as catalytic support,<sup>6,7</sup> photovoltaics<sup>8</sup> and more recently as electrode material in lithium ion batteries,<sup>9–11</sup> to name only a few.

In various technologically relevant applications, such as catalysis, solar cells, *etc.*, nanosized materials have shown beneficial properties related not only to their chemical composition, but also to the small dimensions, *i.e.* the large surface to volume ratio, special reactivity and so on. Nanoscale titania is one of the materials that has been extensively studied in the past decades and it has been shown that the performance in certain applications is largely influenced by the size of the building blocks.<sup>12,13</sup> Many new synthesis protocols have been established not only focusing on the accessibility of nanosized particles, but also on how to control the size distribution of *e.g.* nanoparticles, the formation of a certain polymorph, the surface properties, or even the morphological anisotropy, *e.g.* in nanorods, -wires or -tubes. In addition, parameters such as the assembly of the

nanoscale particles into larger aggregates, the degree of crystallinity, the yields and applicability of the synthesis protocols have been considered. In addition, several research groups concentrated their efforts on the synthesis of porous titania materials with high specific surface areas, such as inverse opal structures, mesoporous titania or titania aerogels, very often displaying pore walls in the nanometre regime.<sup>14–17</sup>

It would be beyond the scope of the present review to summarise all the achievements made in the last few decades in the synthesis of nanoscale titania. A more comprehensive overview has recently been by Chen and Mao.<sup>13</sup> Here we will instead focus on novel solution-based synthesis routes or precursor systems towards crystalline titania particles exhibiting still rather high specific surface areas. The main topic will be novel approaches *via* glycolated precursors and miniemulsion processes. The application of titania in photocatalytic applications has been recently reviewed<sup>18</sup> and we instead focus on applications in energy storage, *e.g.* as electrodes in Li-ion batteries, and as support material in catalysis. Here, the materials prepared *via* the glycolated precursor approach are compared to other nanoscale materials.



**U. Kaiser**

*Ute Kaiser is a Professor of Materials Science Electron Microscopy at the University of Ulm, Germany. After receiving her PhD in crystallography in 1993 from the Humboldt University of Berlin, she received a post-doctoral position at the Friedrich-Schiller University Jena and was working on transmission electron microscopy of semiconductors and optical thin films. In 2002 she received her habilitation and gained her lecturing qualification.*

*In 2004, she became a full professor of Electron Microscopy at the University of Ulm.*

## 2. Synthesis routes to titanium dioxide nanostructures

Titanium dioxide is industrially produced from its minerals, such as ilmenite or rutile by the sulphate or the chloride process.<sup>19</sup> In view of the importance of titanium dioxide it is not surprising that numerous processes have been developed and reported for the synthesis of the different titanium oxide polymorphs rutile and anatase as well as amorphous phases. In addition, three metastable modifications of TiO<sub>2</sub> can be synthesized: monoclinic phase TiO<sub>2</sub> (B), a hollandite type tetragonal phase TiO<sub>2</sub> (H) and a ramsdellite type orthorhombic phase.<sup>20–22</sup> TiO<sub>2</sub> (B) has also been found in submicroscopic quantities in natural minerals.<sup>23</sup>

The synthesis processes to amorphous and typical titania polymorphs (anatase/rutile/brookite) include amongst others the hydrolysis of TiCl<sub>4</sub>, flame pyrolysis of TiCl<sub>4</sub>, electrodeposition, solvo- or hydrothermal methods, microwave treatments,



**K. Landfester**

*Katharina Landfester studied chemistry at the TU Darmstadt. In 1995, she received her PhD in Physical Chemistry from the University of Mainz. After a postdoctoral stay at the Lehigh University, where she first came in contact with the miniemulsion technique, she returned to Germany in 1998 joining the group of Prof. M. Antonietti (MPI of Colloids and Interfaces). In 2002, she obtained her habilitation in Physical Chemistry at the University of Potsdam,*

*accepted a chair (C4) of Macromolecular Chemistry at the University of Ulm (2003) and since 2008, she has been a director at the Max Planck Institute for Polymer Research.*



**M. Wohlfahrt-Mehrens**

*Margret Wohlfahrt-Mehrens studied chemistry at the University of Bonn. In 1989, she received her PhD in chemistry from the University of Witten-Herdecke. She joined ZSW in Ulm in 1990 and since 1995, she has been the head of the department of Accumulators Materials Research at ZSW.*

**Table 1** Selected synthesis methods towards titanium dioxide nanomaterials

Synthesis method	Phases formed					BET specific surface area <sup>f</sup>	Ref.
	Am <sup>a</sup>	A <sup>b</sup>	R <sup>c</sup>	A + R <sup>d</sup>	B <sup>e</sup>		
Room temperature hydrolysis and precipitation of TiCl <sub>4</sub>	X						29, 30
Oxidation of Ti(III)-precursors (precipitation)	X	X	X	X	X	200 m <sup>2</sup> g <sup>-1</sup>	31
Room temperature sol-gel synthesis (typically alkoxides and chlorides)	X	X	X	X	X	~110–150 m <sup>2</sup> g <sup>-1</sup>	10, 32–37
Emulsions (mini/micro)	X	X	X	X		~100–300 m <sup>2</sup> g <sup>-1</sup>	38
Flame pyrolysis of TiCl <sub>4</sub> (combustion)		X		X		1–80 m <sup>2</sup> g <sup>-1</sup>	39, 40
Solvothermal/hydrothermal precipitation at elevated temperatures		X	X	X	X	~215 m <sup>2</sup> g <sup>-1</sup> /~40–110 m <sup>2</sup> g <sup>-1</sup>	41–48
Microwave-induced synthesis	X	X	X			~250 m <sup>2</sup> g <sup>-1</sup>	49, 50
Sonochemical synthesis		X	X			230–400 m <sup>2</sup> g <sup>-1</sup>	51–54
Chemical vapour deposition/gas phase deposition (Ti(OR) <sub>4</sub> )	X	X	X	X		3–300 m <sup>2</sup> g <sup>-1</sup>	55–57
Physical vapour deposition	X	X	X	X			58, 59

<sup>a</sup> Am = amorphous. <sup>b</sup> A = anatase. <sup>c</sup> R = rutile. <sup>d</sup> A + R = anatase and rutile. <sup>e</sup> B = brookite. <sup>f</sup> For crystalline materials only.

sonochemical approaches, chemical- or physical vapour deposition, (micro/mini)emulsion techniques and sol-gel processes.<sup>13</sup> Table 1 gives an overview of selected synthesis routes and the titania polymorphs that are typically accessible *via* this approach. The deliberate synthesis of brookite remains a challenging task and only very few reports can be found.<sup>24–27</sup> In addition, one has to keep in mind that many of the protocols listed below require a calcination step at higher temperatures to obtain the crystalline polymorphs. Crystalline rutile is thermodynamically more stable than crystalline anatase or brookite, but it is not necessarily the resulting product from the synthesis. This depends largely on the pH-value, the precursor concentration and temperature of the system. If a material consists of several crystalline phases kinetic effects can play a decisive role. Thus, it is not unlikely that a metastable phase develops at first that can then eventually transform, *e.g.* by aging or heating, into the thermodynamically favoured phase.<sup>28</sup>

In addition to the polymorph of titania, the crystallite size and the specific surface area are crucial parameters for high performance applications. High surface area materials provide a large interface for any type of reaction, *e.g.* (photo)catalysis, and guarantee good accessibility and contact with the electrolyte in lithium ion batteries. Small primary crystals offer short diffusion paths for lithium and are beneficial for short charging-discharging times in batteries. Therefore, it is essential to develop synthetic approaches that allow for a systematic selection of the crystalline phase, particle size, particle size distribution, and porosity. If this deliberate tailoring of chemical and physical properties, such as the polymorph, specific surface area or particle size, is accomplished, a better control of chemical reactivity and/or stability for a given application can be achieved.<sup>60</sup>

Table 1 gives the specific surface area of the crystalline polymorphs for some arbitrarily chosen examples from the literature regardless of the phase and in most cases taken from gas sorption measurements and evaluation with the Brunauer, Emmett and Teller model (BET). Unfortunately many authors do not give any information on the specific surface area or porosity. As a principle trend, amorphous titania typically shows BET surface areas higher than the crystalline counterparts with values obtained from N<sub>2</sub>-sorption measurements higher than 250 m<sup>2</sup> g<sup>-1</sup>.

The synthetic approaches described in Table 1 not only result in the different polymorphs, but also in various morphologies, such as (nano)particles, films, nanotubes, nanowires, nanoribbons,<sup>61,62</sup> or even monolithic systems.<sup>63,64</sup> As mentioned above, for

many applications the accessible interface plays an important role, and synthetic approaches resulting in high surface area or porous, but crystalline materials become increasingly more relevant. In recent years different protocols have been developed resulting in nanoscale or porous materials exhibiting specific surface areas up to 200 m<sup>2</sup> g<sup>-1</sup> for a crystalline anatase material.<sup>65</sup> Amorphous mesoporous titania with a periodic ordering of the pores was first reported in 1995 *via* a modified sol-gel process applying an alkyl phosphate surfactant.<sup>66</sup> Since then, there have been many reports on the synthesis of mesoporous titania by controlling the high reactivity of Ti(IV) with the addition of stabilizing and/or structure-directing agents, such as phosphates, amines, ionic and non-ionic surfactants and block copolymers.<sup>13,67–71</sup> Only in the last decade, protocols were developed to yield meso/macro-porous, crystalline titania with a periodic ordering of the mesopores.<sup>17,72–74</sup>

However, only very few publications focus on a systematic comparison of the properties of titania structures from different synthetic strategies, which is nevertheless necessary to finding the “optimal” synthetic protocol for a certain application. The vital importance of this, especially in view of the later application, was demonstrated only recently by Hartmann *et al.*<sup>75</sup> They explored potential correlations between preparation, microstructure, and photo-electrochemical water splitting efficiency of TiO<sub>2</sub> based nanostructures in coatings and emphasized the critical importance of electronic conductivity across the oxidic matrix. Another study, in which gas-phase and solution-based protocols were compared, was recently published by Baumann *et al.* focusing on solid-solid interface formation in titania nanoparticle arrangements and the paramagnetic properties of the network.<sup>65</sup>

In this review, we restrict ourselves to low temperature, solution-based processes towards crystalline titania nanostructures. For processes, such as hydrothermal, microwave or sonochemical approaches – even being very relevant in the synthesis of titania nanomaterials – selected relevant publications from the last few years are given. Sol-gel processing (aqueous and non-aqueous) plays a very important role in the synthesis of titania nanostructures with high specific surface areas, however in most cases amorphous materials are obtained. Here, novel sol-gel approaches towards crystalline titania are presented in more detail in the following chapters.



## 2.1 Hydrothermal, sonochemical and microwave processing towards nanosized titania polymorphs

Hydro- or solvothermal processing are interesting approaches to directly prepare micro- and nanometre-sized crystalline powders with high level of control of the shape.<sup>43,76–78</sup> In recent years, large research efforts were devoted to the synthesis of micrometer-sized single crystal TiO<sub>2</sub> materials, *e.g.* anatase, with deliberately chosen exposed facets of the crystal, since it is assumed that the chemical reactivity of the material can be tailored in this manner. Typical synthesis pathways are hydrothermal approaches, *e.g.* in the presence of TiF<sub>4</sub> or fluoride ions.<sup>79–81</sup> In hydrothermal processes, the synthesis is typically carried out at rather high temperatures, resulting in agglomerated nanocrystals. Many different reaction conditions, precursors, catalysts, and even structure-directing agents have been successfully employed to improve the properties of the final product. In some cases additives, such as stabilizing agents, have been used to prevent agglomeration. A detailed description would be beyond the scope of this review article. To name only one more recent example, Cozzoli *et al.* demonstrated the controlled growth of anatase nanocrystals and high aspect ratio TiO<sub>2</sub> anatase nanorods by hydrolysis of titanium alkoxides in the presence of a surfactant (oleic acid) and amines as crystallization promoters in very mild hydrothermal conditions with temperatures of 80–100 °C.<sup>82,83</sup>

Microwave-assisted hydrothermal or even sol–gel approaches become increasingly popular in recent years due to several advantages, such as shorter reaction times, in many cases smaller particles sizes, and that high purity materials can be obtained.<sup>84</sup> In the presence of a structure-directing agent, such as a triblock copolymer, even anatase nanorods with mesopores and rather high specific surface areas of larger than 250 m<sup>2</sup> g<sup>−1</sup> have been synthesized.<sup>85</sup> However, an amorphous material was obtained from the synthesis, which resulted in anatase nanorods only after calcination at 400 °C. Direct crystallization of anatase TiO<sub>2</sub> nanocrystals with exposed {001} facets was successfully demonstrated by Zheng *et al.* at 200 °C for 30 min in a microwave digestion system in HF solutions.<sup>49</sup>

Ding *et al.* demonstrated a facile synthesis towards size-controlled cube-like anatase nanocrystals in ionic liquids with only 40 minutes of microwave treatment.<sup>86</sup> A similar approach by using ionic liquids as structure-directing agents resulted in porous single-crystal like anatase TiO<sub>2</sub> structures with excellent lithium storage properties.<sup>87</sup>

Combinations of different processes, such as sol–gel processing combined with microwave treatment of the resulting powders, allow for the conversion of a nanoparticulate sol–gel product with particle sizes of around 9 nm and specific surface areas of larger than 550 m<sup>2</sup> g<sup>−1</sup> to nanocrystalline anatase TiO<sub>2</sub> tubes with a diameter of about 5 nm.<sup>88</sup>

Sonochemical approaches require the application of powerful ultrasonic radiation (20 kHz–10 MHz) in the synthesis protocol. Nanophased, crystalline titania has been synthesized *via* this approach already some years ago and research in this area is still ongoing.<sup>51</sup> It was stated that a better dispersion of the nanoparticles, a marginally higher surface area, a better thermal stability and phase purity can be obtained by the sonication.<sup>54,89</sup> Recently, highly crystalline, spherical titania nanoparticles were

synthesized by Gedanken *et al.* by reacting transition metal chloride with benzyl alcohol using ultrasonic irradiation under an argon atmosphere in a non-aqueous solvent. The sonochemical process was conducted at a relatively low temperature of 363 K and no further calcination step was required.<sup>90</sup>

## 2.2 Sol–gel processing

As described above, many methods have been established for generating titania particles.<sup>13,91</sup> Among all techniques, the sol–gel approach based on the controlled hydrolysis and condensation of appropriate precursors, mostly titanium alkoxides or chlorides, is of particular interest, because it gives a very good compositional and morphological control over the product properties, such as specific surface area, nanoparticle size, degree of aggregation, *etc.*<sup>92</sup> In sol–gel processes, the final product morphology is strongly influenced by the reactivity of the precursor, but also by the reaction conditions, such as the pH of the reaction medium, the water to precursor ratio and the reaction temperature.<sup>65</sup>

**2.2.1 Sol–gel processing of titanium alkoxides.** Titanium alkoxides react vigorously with water and ill-defined titanium-oxo/hydroxo species are formed. The presence of chemical additives, which coordinate to the titanium centre, such as bidentate ligands, lowers the rate of hydrolysis and allows for the preparation of transparent sols, particles and gels.<sup>93,94</sup> The precipitates or gels that are obtained by sol–gel processing are typically amorphous, exhibiting a rather high specific surface area and are in some cases even (meso)porous (see above). A transition from the amorphous to the crystalline phase is generally induced by an annealing step with temperatures higher than 300 °C, leading in most cases to a collapse of the pore system and an increase of the particle size concomitant with a decrease of the specific surface area. Only very low pH-values can give crystalline titania polymorphs *via* sol–gel processing.<sup>95</sup> So far, very few groups reported a low temperature synthesis approach towards crystalline titania (anatase) with high specific surface areas or porosity based on aqueous sol–gel processes.<sup>96,97</sup> The direct synthesis of rutile is even more difficult and rather harsh reaction conditions, such as very low pH-values below zero, are typically applied.<sup>77</sup> Palmqvist *et al.* synthesized nanoparticulate anatase and rutile at low temperatures in microemulsion systems in the presence of a template Pluronic F127.<sup>98</sup> Han *et al.* published the synthesis of highly crystalline anatase and rutile titania nanocrystals from titanium alkoxide solutions in the presence of P123.<sup>99</sup> And only recently, Kröger *et al.* reported the ability of recombinant silaffin to induce the formation of rutile from a titania(IV) complex in buffered aqueous solution under ambient conditions and higher pH-values.<sup>100</sup> Often non-aqueous solution-based synthesis routes are applied, if titania nanoparticles with higher crystallinity are required.<sup>101</sup> In this case, metal halides, *e.g.* titanium tetrachloride, can be reacted with benzylalcohol, but also with titanium alkoxides.<sup>102,103</sup>

**2.2.2 Sol–gel processing of titanium glycolates.** In the synthesis of well-defined nanostructured materials, glycols and polyols are becoming increasingly important in recent years for several reasons. On the one hand, they can be used as coordinating ligands to control hydrolysis rates of transition metal alkoxides,<sup>10,38,104,105</sup> on the other hand they are versatile



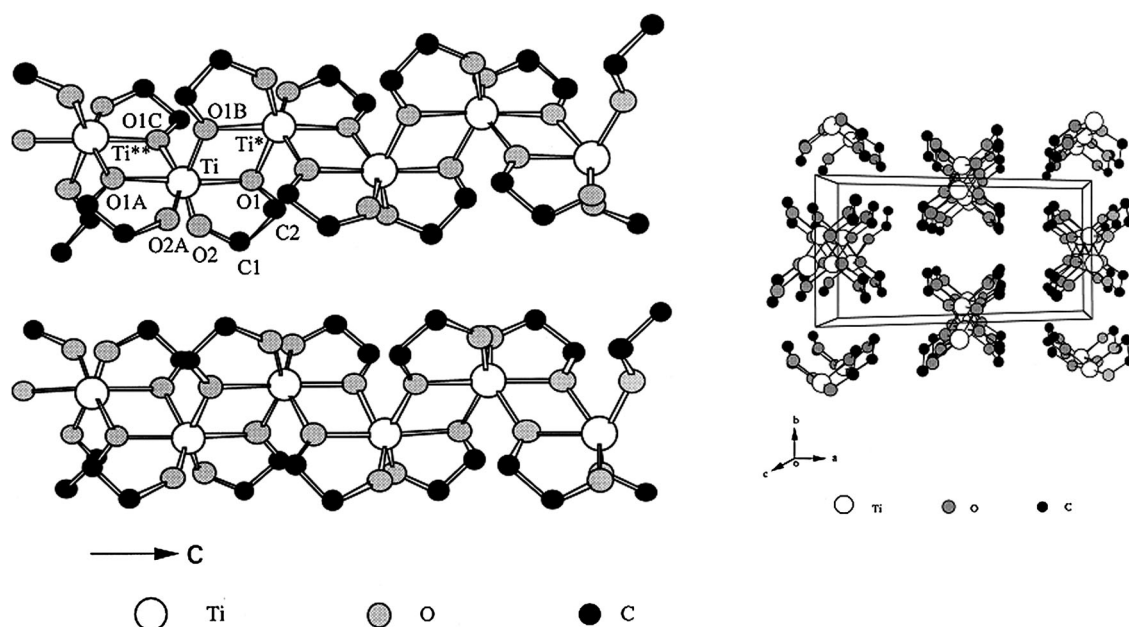


**Fig. 1** View on the one-dimensional chains of  $\text{Ti}(\text{OCH}_2\text{CH}_2\text{O})_2$  along the  $c$ -axis (left), and view with the unit cell outlined showing the pack along the  $c$ -axis (right); (taken with permission from Wang *et al.*<sup>110</sup>).

solvents in the synthesis of nanostructured materials, especially metals, a process which is also termed the “polyol” process.<sup>106–108</sup> For titanium-based materials, ethylene glycol and titanium alkoxides react sufficiently well to give the glycoxides in good yields, *e.g.*  $\text{Ti}(\text{OCH}_2\text{CH}_2\text{O})_2$  can be prepared by reaction of a titanium alkoxide with ethylene glycol.<sup>109</sup> Performing the reaction in an autoclave and the presence of an amine allowed to obtain single crystals.<sup>110</sup> The structure was solved in the  $C$ -centred monoclinic space group  $C2/c$  and consists of an infinite one-dimensional chain structure with edge-sharing  $\text{TiO}_6$  tetrahedra in the  $c$ -direction (Fig. 1).

This reaction is not only limited to ethylene glycol, but also other diol/polyols can be used. 2-Ethylhexane-1,3-diol, butane-2,3-diol, and 2-methylpentane-2,4-diol have been reported already in the 1950s and many more have been used in recent years, such as octane-1,8-diol, pentane-1,5-diol, naphthalene-2,3-diol or even poly(methylene glycol).<sup>109,111–114</sup> One major advantage of these glycolated precursors is their outstanding stability not only in alcohol but also in water and in a humid atmosphere. Because of this high stability, only very few groups report the synthesis of titania from these precursors by hydrolysis and condensation reactions, but rather focus on the thermolysis at higher temperatures.<sup>108,113–115</sup> One interesting example was published by Xia *et al.*<sup>108</sup> For the reaction of titanium alkoxides with ethylene glycol at elevated temperatures of 170 °C, the formation of titanium glycolate nanowires was reported with an average diameter of  $50 \pm 8$  nm (Fig. 2).<sup>108</sup> Thermal treatment in air at 350 °C, 500 °C or 850 °C resulted in amorphous, anatase and rutile phases, respectively, but allowed for the preservation of the 1D nanostructure.

Besides the thermolysis to  $\text{TiO}_2$  (anatase and rutile), also composite materials, such as  $\text{TiO}_2$ -C, can be obtained by keeping the one-dimensional rod-like structure.<sup>115,116</sup>

As already mentioned above, only very few reports comment on the sol-gel processing of these titanium glycolates.<sup>10,38,104,105</sup>

However, with an increasing interest in water-soluble precursors and the aim of developing non-toxic, environmentally benign systems, the glycolated titanium centres are very promising in the solution-based synthesis of titania. In one of the first reports of the application of these molecules as water-soluble precursors, three different diolates of titanium ( $[\text{Ti}(\text{OCHRCH}_2\text{O})_2]$  with  $\text{R} = -\text{H}$ ,  $-\text{CH}_3$ ,  $-\text{CH}_2\text{CH}_3$ ) were converted to anatase by microwave heating in boiling water.<sup>117</sup> Pal *et al.* converted titanium glycolates *via* controlled hydrolysis to amorphous nanoparticles, which could be calcined to anatase and rutile.<sup>118</sup> The influence of the presence of surfactants and the pH-value on the formation of titania nanostructures was also reported recently.<sup>10,105,119</sup> Bis(2-hydroxyethyl)titanate was employed in a low temperature sol-gel synthesis in the presence of a nonionic surfactant (Brij56) to obtain mesoporous anatase particles aggregates with a crystallite size of 9 nm and a specific surface area of  $110 \text{ m}^2 \text{ g}^{-1}$ . In the TEM images (Fig. 3) interparticulate pores (indicated by white arrows) formed between the aggregated particles are observed. No heat treatment is required to obtain anatase.

A glycerol-modified titanium precursor was used to synthesize rutile  $\text{TiO}_2$  in the presence of an anionic surfactant at low temperature *via* a hydrolytic sol-gel route by Kubiak *et al.*<sup>119</sup> The phase purity of the obtained material was determined by XRD and nitrogen sorption measurements gave a high specific surface area of  $181 \text{ m}^2 \text{ g}^{-1}$  with an observed interparticle porosity. HRTEM and SEM measurements revealed growth anisotropy with whiskers showing a high aspect ratio. Radial organized aggregates of these needles with a diameter of approximately 4–5 nm and a length of 50 nm forming cauliflower-like nanowhisker arrangements (Fig. 4) are observed.

From these examples it can be seen that in recent years new low temperature synthetic protocols towards nanoscale, crystalline, porous and high surface area titania have been developed. More exciting results can be expected in the next years.

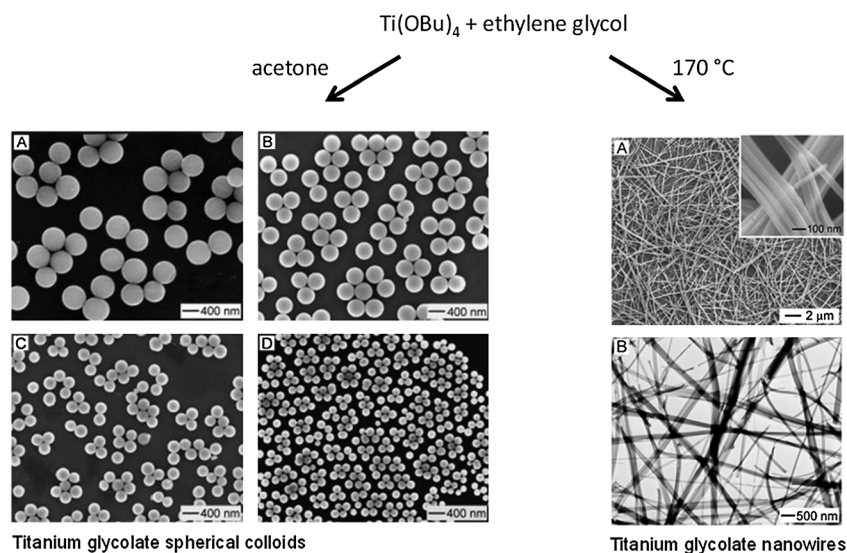


**Fig. 2** (left) SEM images of spherical colloids of titania glycolates that were prepared with different molar concentrations of titanium butoxide in acetone; (right) SEM and TEM images of titanium glycolates after heating the precursor mixture to 170 °C. (reprinted and adapted with permission from Jiang *et al.*<sup>108,395</sup>).

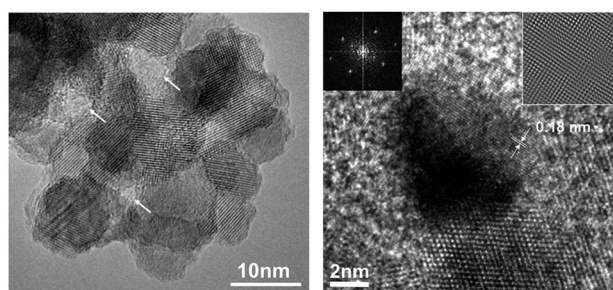


**Fig. 3** TEM images of anatase TiO<sub>2</sub> aggregates. Inset: electron diffraction pattern (reprinted with permission from Kubiak *et al.*<sup>10</sup>).

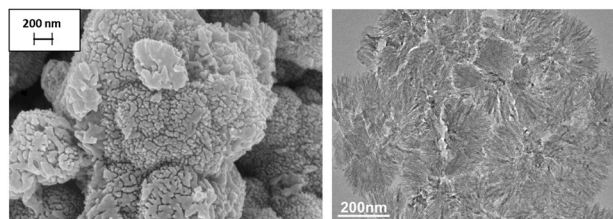


**Fig. 4** SEM image (left) and TEM micrograph (right) of nanosized rutile TiO<sub>2</sub> (reprinted with permission from Kubiak *et al.*<sup>119</sup>).

### 2.3 Synthesis in miniemulsion

In addition to conventional sol–gel processing, the inverse miniemulsion process is a very suitable technique for the preparation of monodisperse TiO<sub>2</sub> nanoparticles. In this system, uniformly sized droplets of an aqueous sol–gel precursor solution are reacted to metal oxide nanoparticles. A miniemulsion aiming at the synthesis of inorganic oxide materials is typically generated by the dispersion of an aqueous precursor solution, *e.g.* by ultrasonication, in an inert hydrocarbon.<sup>10,38,120–122</sup> Droplet collision and coalescence are prevented by a surfactant added to the system. Additionally, an osmotic pressure agent is present in the droplets. As this

agent is only soluble in the dispersed phase and extremely insoluble in the continuous phase an osmotic pressure is established, which counteracts particle degradation by diffusion processes (Ostwald ripening). Unlike in a microemulsion, in which diffusion processes take place, leading to an exchange of reactants among the droplets, in a miniemulsion, each droplet acts as an individual nanoreactor. Exclusively localized there, hydrolysis and condensation of the precursor take place. During the process the droplet size, droplet number and the concentrations in each droplet are preserved. Thus, the final particle size can be easily tuned by the droplet size. Moreover, the composition of the particles is determined by the composition of the dispersed phase before homogenization.<sup>123,124</sup>

Pure titania nanoparticles were prepared in miniemulsion using the water soluble precursor titanium glycolate (EGMT).<sup>38</sup> The influence of several preparation parameters (composition of dispersed phase, reaction temperature, surfactant concentration) on the crystal phase, crystallite size, morphology, and specific surface area of the titania nanoparticles was investigated.

As presented in Fig. 5, the sol–gel reaction was induced by acid catalyzed hydrolysis of EGMT at increased temperature. Thus, different ratios of HCl:EGMT were used for the preparation. The ratio of HCl:EGMT determined the polymorph of the products. According to the relative amounts, pure anatase or a mixture of rutile/anatase was isolated. Only with large amounts of HCl, exclusively anatase was generated. Irrespective of the phase compositions the products were of particulate structure with a diameter of 150–300 nm (Fig. 5). Transmission electron micrographs showed that these nanoparticles are aggregates of individual titania crystallites with sizes around 10 nm. The variation of the reaction temperature is another possibility to adjust the phase composition of the titania nanoparticles. While only an amorphous material was obtained, using a ratio HCl:EGMT of 5.4:1 and a temperature of 20 °C, an increasing reaction temperature gave a mixture of anatase and rutile. Single phase anatase is generated at reaction temperatures of more than 100 °C. The crystallite size was estimated as 5 nm



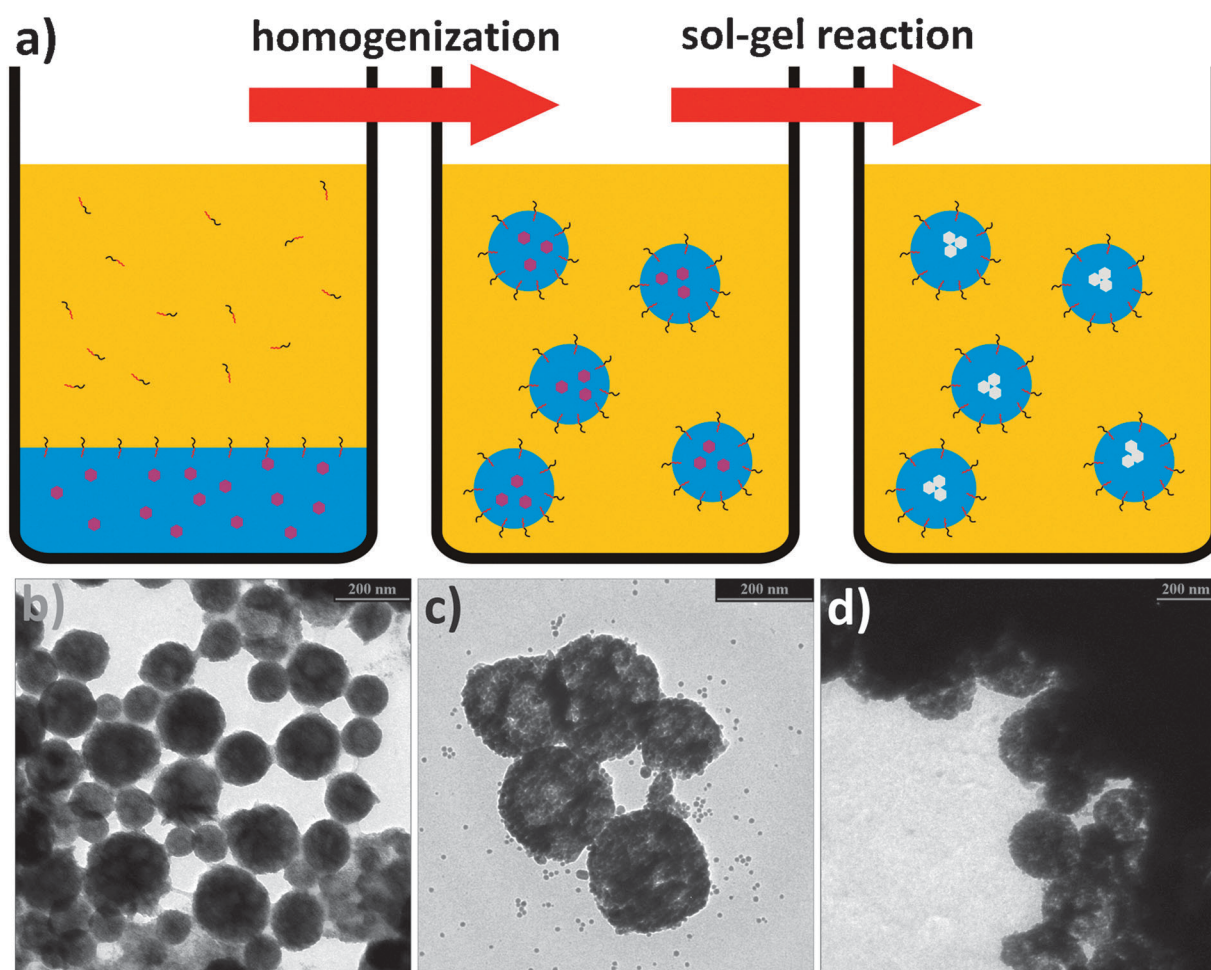


**Fig. 5** (a) A typical inverse miniemulsion process is schematically shown. A two phase mixture from an aqueous solution of a sol-gel precursor (purple) and an organic surfactant solution is homogenized to form a stable miniemulsion of droplets with uniform size and composition. By increasing the temperature, the sol-gel reaction is induced to generate aggregates of oxide nanoparticles (light grey). (b–d) Nanoscaled aggregates of titania crystallites, synthesized at different ratios HCl:EGMT. (b) EGMT:HCl = 1:5.4, as synthesized, (c) EGMT:HCl = 1:3.2, after calcination at 400 °C, and (d) EGMT:HCl = 1:4.3 after calcination at 400 °C. (b)–(d) (adapted with permission from Rossmanith *et al.*<sup>38</sup> Copyright (2008) American Chemical Society).

using the Scherrer equation. Typically, the phase composition was retained after calcination at 400 °C, although the amount of rutile in the samples slightly increased. This was accompanied by an increased crystallite size with estimated values of 9 nm. The transformation of anatase to rutile starts with calcination temperatures of 500 °C. Here, the crystallite size further increases due to sintering effects. This is consistent with the above-mentioned thermodynamic stability of nanoscale titania.<sup>19</sup>

A typical feature of a miniemulsion is the ability to tune the droplet size by the amount of surfactant in the system. More surfactant leads to smaller droplets as more interfacial area can be stabilized. In the investigated system, the variation of the surfactant had several effects. First, the diameter of the droplets in the miniemulsion significantly decreases from nearly 1 µm when using the smallest amount of surfactant, which is still able to stabilize the droplets (0.7 wt%) down to 340 nm with 5 wt% of surfactant. Moreover, the size of the titania particles after completed reaction and evaporation of the water decreases from 220 nm to 70 nm. Interestingly, the size of the individual anatase crystallites also decreases from

8 to 5 nm with increasing surfactant concentration. This means that the surfactant is participating in the crystallite formation. Most important, regarding potential applications, however, the specific surface area is increased from 140 m<sup>2</sup> g<sup>-1</sup> to more than 300 m<sup>2</sup> g<sup>-1</sup> after calcination. This is an extraordinarily high value for anatase.

Other heterophase systems are also reported for the generation of nanoparticulate titania, most notably direct and inverse microemulsions. Typically, water-in-oil (inverse) microemulsions are used. Here, an aqueous precursor solution is dispersed in an inert hydrocarbon, as *e.g.* cyclohexane or hexane. The precursor, its mode of addition, the presence of a co-surfactant, the type and amount of surfactant are varied as well as the reaction temperature and time. There are few reports on the use of oil-in-water microemulsions<sup>125</sup> and the use of supercritical CO<sub>2</sub> as continuous phase.<sup>126,127</sup> The most frequently used precursors are TiCl<sub>3</sub>,<sup>128</sup> TiCl<sub>4</sub>,<sup>129–132</sup> and pre-hydrolyzed titanium alkoxides, as titanium isopropoxide<sup>126,127,133,134</sup> or titanium butoxide.<sup>48,98,133,135,136</sup> Nonionic (Triton X-100,<sup>48,128,135–137</sup> PEO-alkylethers,<sup>129</sup> Pluronic<sup>98</sup>), anionic



(AOT<sup>131,133,134</sup>) as well as cationic (CTAB<sup>130,132</sup>) surfactants were reported.

Despite all of the differences, there are some general features to be stated. The initial hydrolysis and condensation of the precursor lead to small amorphous or crystalline entities, which are restricted to the water pools and are of roughly their size. This means that by increasing the water–surfactant ratio, the structures become larger. The observed range is 3–6 nm.<sup>133,136</sup> The titania phase is controlled by several parameters as the concentration of the precursor,<sup>129,131,134</sup> the type and concentration of catalyst (acid, base),<sup>135</sup> the presence and concentration of ions (sulfate)<sup>48</sup> or other additives as urea,<sup>128</sup> as well as reaction temperature and time.<sup>129,135,136</sup> If the reaction temperature is such that amorphous titania is generated, an annealing or calcination step has to be performed after initial reaction to transform the material into a crystalline phase. Again, the modification is dependent on various process parameters. The as prepared nanoparticles (<5 nm) typically have a high to very high specific surface area of up to 300 m<sup>2</sup> g<sup>−1</sup>, which is reduced to values of 150 m<sup>2</sup> g<sup>−1</sup> and below after calcination or annealing, accompanied by a growth of the crystallite size to 15–20 nm.<sup>48,125–127,136</sup>

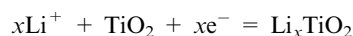
Depending on the reaction conditions, these primary building blocks can assemble to larger micro- or nanoparticulate structures of various morphologies. In systems where predominantly rutile is generated, elongated, needlelike structures are created.<sup>136</sup> These assemble to micron-sized polycrystalline structures with shapes of cauliflowers, dumbbells or bricks.<sup>128,130</sup> Aggregates of anatase are typically spherical. These aggregates do not form within the micelles, as their size is in the lower nanometer range.

Adding gelatin to the droplet in a microemulsion, the hydrolysis rate of the precursor TiCl<sub>4</sub> is reduced and the reaction is restricted to the interface of the droplet and the continuous phase. Thus, capsules of about 25–30 nm in diameter with a shell of amorphous titania (5 nm thickness) were generated. However, after calcination at 400 °C resulting in the generation of anatase crystallites of 8–10 nm the capsules lose their integrity.<sup>132</sup>

The microemulsion technique was also used for the creation of polymer–titania hybrid nanoparticles by employing precursors which were functionalized to be an ATRP initiator and subsequent controlled polymerization from the titania particles.<sup>137</sup>

### 3. Electrochemical behaviour of anatase and rutile TiO<sub>2</sub> polymorphs

Anode materials based on titanium oxides are promising candidates as alternative materials to carbonaceous anodes due to advantages in terms of cost, safety and toxicity.<sup>11,138</sup> Among the several polymorphs of TiO<sub>2</sub>, TiO<sub>2</sub> (B), anatase and rutile are promising anode materials for lithium-ion batteries.<sup>138–141</sup> Typically the Li<sup>+</sup> insertion–extraction reaction for TiO<sub>2</sub> polymorphs occurs in the potential range of 1.4–1.8 V vs. Li–Li<sup>+</sup>, according to the following reaction:



The maximum theoretical capacity is 335 mAh g<sup>−1</sup> which corresponds to  $x = 1$ , and to the complete reduction of Ti<sup>4+</sup> to Ti<sup>3+</sup>. This makes TiO<sub>2</sub> a highly competitive alternative

to graphite anodes having a theoretical capacity of 372 mAh g<sup>−1</sup>. The relatively high operating potential (about 1.5 V vs. Li<sup>+</sup>–Li) improves safety and long term stability of the lithium ion cell. In contrast to graphite with a working potential below 0.2 V vs. Li–Li<sup>+</sup> no metallic lithium dendrite formation occurs during fast charge and overcharge conditions and SEI formation is reduced.

The concrete working potential of the cell depends on the TiO<sub>2</sub> polymorph used.

Among the TiO<sub>2</sub> polymorphs, anatase and TiO<sub>2</sub> (B) are considered as the most promising candidates for the use as anode material for Li-ion batteries due to their fast Li<sup>+</sup> insertion–extraction reactions and high insertion capacity. From the practical viewpoint, reversible insertion into anatase TiO<sub>2</sub> is about 0.6 Li (*i.e.* 200 mAh g<sup>−1</sup>) at 1.78 V vs. Li<sup>+</sup>–Li.<sup>9,142,143</sup> On the other hand, the rutile TiO<sub>2</sub> polymorph has been considered a poor Li-insertion material for a long time. It is only recently that excellent capacities at high rates have been reported for TiO<sub>2</sub> rutile with nanosized dimensions and higher specific surface areas.<sup>119,144,145</sup> TiO<sub>2</sub> (B) has an insertion potential of about 1.6 V vs. Li<sup>+</sup> associated with the Li<sup>+</sup> insertion into the structure. A composition of Li<sub>0.91</sub>TiO<sub>2</sub> corresponding to 305 mAh g<sup>−1</sup> has been reported for the first cycle with a reversible intercalation of approximately 0.7 mol Li<sup>+</sup> per mol TiO<sub>2</sub>.<sup>146–149</sup>

TiO<sub>2</sub> (B), which is a monoclinic metastable phase of titanium dioxide, is another promising high voltage anode material for lithium ion batteries. TiO<sub>2</sub> (B) has an insertion potential of about 1.6 V vs. Li<sup>+</sup> associated with the Li<sup>+</sup> insertion into the structure. A composition of Li<sub>0.91</sub>TiO<sub>2</sub> corresponding to 305 mAh g<sup>−1</sup> has been reported for the first cycle with reversible capacities of 200–300 mAh g<sup>−1</sup> with good cyclability.<sup>146–149</sup>

TiO<sub>2</sub> (B) has a more open structure than anatase and rutile with accessible channels for Li<sup>+</sup>-transport perpendicular to the (010) face, which leads to fast lithium ion transport within the structure. The electrochemical performance of TiO<sub>2</sub> (B) highly depends on the crystallite size, crystallographic orientation and particle size of the materials. Especially one dimensional nanostructured materials like nanorods and nanotubes demonstrate excellent lithium insertion–extraction when compared to bulk material or nanoparticles of TiO<sub>2</sub> (B). Theoretical calculations as well as recent experimental results demonstrate that the lithium insertion–extraction process can be accelerated by reducing the extension of the unit cell of the crystals along the *b*- and *c*-axis. Therefore, the control of particle size and crystallographic orientation of nanotubes and nanorods is extremely important to get high rate performance and high reversible capacity.<sup>150–162</sup> Nanotubes and nanowires of TiO<sub>2</sub> (B) are usually prepared *via* hydrothermal synthesis routes. Inaba *et al.* have reported the synthesis of nanosized needle shaped TiO<sub>2</sub> (B) *via* a precursor route starting with K<sub>2</sub>Ti<sub>4</sub>O<sub>9</sub>. The TiO<sub>2</sub> (B) was obtained by ion exchange and following dehydration of the intermediate product. The discharge capacity and high rate capability (106 mAh g<sup>−1</sup> at 10 °C) was comparable with data reported for hydrothermal prepared materials in the literature.<sup>150</sup>

Very few reports of electrochemical lithium insertion into TiO<sub>2</sub> brookite polymorph have been published.<sup>163,164</sup> Reddy *et al.* have reported a reversible capacity of 160–170 mAh g<sup>−1</sup> at 1.7 V vs. Li–Li<sup>+</sup> for nanosized brookite samples.<sup>164</sup>

In this review, we summarize the latest developments obtained for the anatase and rutile polymorphs. We report the mechanism of lithium insertion–extraction into both structures and especially focus on the electrochemical performance obtained of both materials in terms of capacity, rate capabilities and stability. It can clearly be demonstrated that the optimization of  $\text{TiO}_2$  morphology with higher specific surface areas and to the nanometre regime is a key point to obtain an excellent electrochemical lithium insertion–extraction performance.

### 3.1 $\text{TiO}_2$ anatase

**3.1.1 Li insertion–extraction mechanism.** The reaction of lithium insertion into/from anatase  $\text{TiO}_2$  has been extensively studied both theoretically and experimentally.<sup>9,165–171</sup> During the Li insertion the tetragonal  $\text{TiO}_2$  anatase phase (space group  $I4_1/amd$ ) is transformed into an orthorhombic one,  $\text{Li}_{0.5}\text{TiO}_2$  (space group  $Imma$ ). A spontaneous phase separation into lithium-poor  $\text{Li}_{0.01}\text{TiO}_2$  and lithium-rich  $\text{Li}_{0.5}\text{TiO}_2$  occurs and this process is characterized by a constant voltage. Wagemaker *et al.* showed that the two phases were in equilibrium with a continuous Li flux operating between them.<sup>168,170,171</sup> The voltammogram shown in Fig. 6 presents a pair of peaks at about 1.75 V (cathodic) and 2.0 V (anodic) corresponding to the faradaic insertion and extraction of lithium into anatase  $\text{TiO}_2$ . The maximum insertion capacity  $x$  of 0.5 mol of Li per 1 mol of anatase is given by the number of vacant 4b sites for Li ions, corresponding to one-half of interstitial sites in the anatase structure.<sup>9,165–171</sup>

Besides the main process of the two-phase Li insertion into the tetragonal phase, an additional insertion process takes place at insertion depths exceeding that of anatase. The other types of surface storage mechanisms, connected with pseudo-capacities, have been studied and appear to be strictly related to the dimensions, the porosity, and the surface area of the material.<sup>172</sup> A complete picture of the lithium insertion–extraction into/from anatase  $\text{TiO}_2$  is given by the galvanostatic curve in Fig. 7.

The voltage profile of first discharge of the three investigated materials presents three distinct regions:

- The first region (I) before a constant voltage plateau ( $>1.78$  V) is characterized by a potential drop attributed to the formation of the conductive  $\text{Li}_x\text{TiO}_2$  in solid-solution domain.<sup>173</sup>

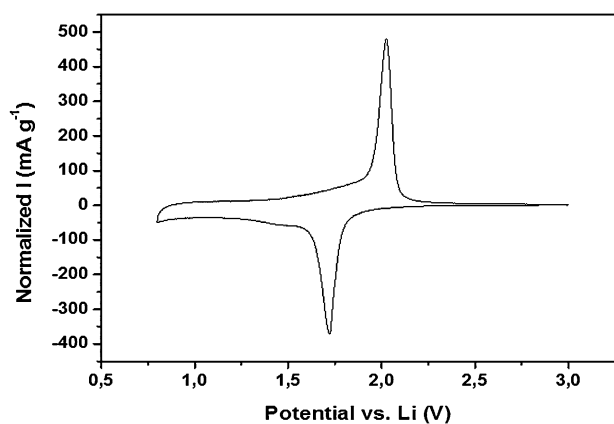


**Fig. 6** Cyclic voltammetry of anatase  $\text{TiO}_2$  between 0.8 and 3 V in 1 M  $\text{LiPF}_6$  EC/DMC (1–1 wt); scan rate  $0.1 \text{ mV s}^{-1}$  (reprinted from Kubiak *et al.*<sup>105</sup> with permission from Elsevier).

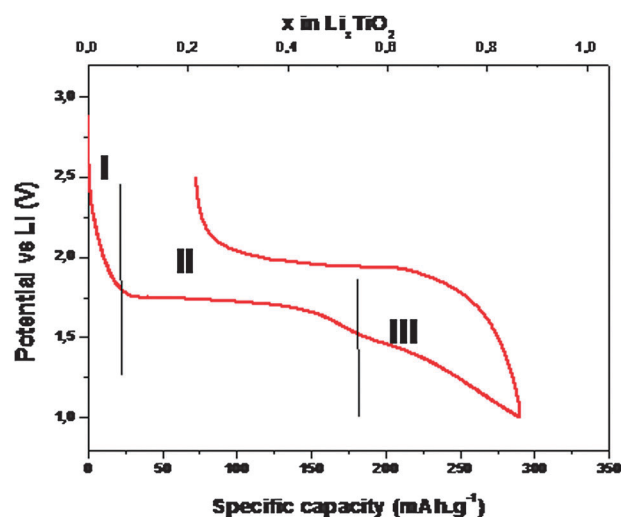


**Fig. 7** First galvanostatic Li insertion–extraction curves of  $\text{TiO}_2$  anatase obtained at C rate between 1 and 3 V.

The extent of this domain is directly proportional to the specific surface area of the materials.<sup>10</sup>

- The second region (II) shows a plateau at 1.78 V which is attributed to a well-known two-phase mechanism described above.

- The third region (III) at potentials below 1.5 V exhibits a sloped curve. This process involves surface lithium storage. The extent of this domain depends on the surface area of the material.<sup>10</sup>

Finally, the amount of lithium that can be inserted in anatase  $\text{TiO}_2$  is strictly connected to the morphology of the material. It has been demonstrated that the fully lithiated phase with a composition of  $\text{Li}_1\text{TiO}_2$  can be obtained from nanosized anatase  $\text{TiO}_2$  with particle size lower than 7 nm.<sup>146</sup>

#### 3.1.2 Electrochemical performance of anatase $\text{TiO}_2$ .

Among the  $\text{TiO}_2$  polymorphs, anatase is considered as the most promising candidate for the use as anode material for Li-ion batteries due to its fast  $\text{Li}^+$  insertion–extraction reactions and high insertion capacity.<sup>171,173–175</sup> However, the reversible capacity reported for bulk anatase is  $x = 0.5$  Li ( $168 \text{ mAh g}^{-1}$ ).<sup>139,165,167,176</sup> To improve the performance and increase the capacity, considerable research effort has been devoted to nanosized, high surface area materials. It is well known that nanosized materials exhibit a superior electrochemical performance compared to bulk ones.<sup>177–179</sup> For nanosized materials small crystallite sizes lead to faster lithium insertion–extraction together with a large specific surface area that provides a better accessible electrode–electrolyte interface. This strategy has been successfully applied for anatase  $\text{TiO}_2$ , and an excellent electrochemical performance has been reported by several groups. For example, Jiang *et al.* studied three different commercially available anatase nanopowders with crystallite sizes of 6, 15 and 30 nm, respectively.<sup>174</sup> They reported a first discharge capacity of more than  $350 \text{ mAh g}^{-1}$  and  $209 \text{ mAh g}^{-1}$  for the first charge with the 6 nm material. Moreover, they obtained very good capacities at ultra fast regime ( $0.41$  Li per  $\text{TiO}_2$  at  $40 \text{ A g}^{-1}$ ;  $\sim 239 \text{ C}$ ). The use of nanosized materials is not without complications, however.

Reports of a decrease of the volumetric energy density due to a possible loss of connectivity between particles by parasitic reactions with the electrolyte are well known.<sup>180</sup> Therefore, controlling the morphology appears to be crucial in determining the electrochemical performance of TiO<sub>2</sub> materials in Li-ion batteries. In this context, mesoporous materials have received particular attention since they exhibit an optimal morphology for increasing electrode stability and Li insertion capacity, especially at high charge/discharge rates.<sup>105,181–184</sup> As described above, Kubiak *et al.* synthesized mesoporous anatase TiO<sub>2</sub> *via* a sol–gel method from an ethylene glycol-based titanium precursor in the presence of a non-ionic surfactant at pH 2. They reported excellent rate capability (184 mAh g<sup>−1</sup> at C/5, 158 mAh g<sup>−1</sup> at 2 C, 127 mAh g<sup>−1</sup> at 6 C, and 95 mAh g<sup>−1</sup> at 30 C) and a very good cycling stability.<sup>183</sup> Saravanan *et al.* prepared mesoporous anatase TiO<sub>2</sub> with narrow pore size distribution and high surface area *via* a sol–gel method using various cationic surfactants. They reported excellent electrochemical behaviour in terms of rate capabilities (107 mAh g<sup>−1</sup> at 30 C) and cycling stability.<sup>184</sup> The good performance is attributed to the small crystallite size and to the nanopores, which favour the complete wetting of the TiO<sub>2</sub> by the liquid electrolyte so that rapid Li<sup>+</sup> insertion–extraction can be achieved. The superior electrochemical performance of mesoporous titania has been confirmed by Kubiak *et al.*<sup>10</sup> The authors compared the respective performance of a mesoporous material (TiO<sub>2</sub>-a) obtained by a sol–gel method with a glycolated precursor, bulk TiO<sub>2</sub> (TiO<sub>2</sub>-b) prepared by a sol–gel method with octadecylamine and a nanosized one (TiO<sub>2</sub>-c) prepared by a miniemulsion process (Fig. 8). They found that the electrochemical behaviour is strongly influenced by the morphology of the materials as well as by the cycling conditions, *i.e.* charging rate and working potential window. The nanosized material exhibited higher irreversible capacity loss and lower cycling stability than the mesoporous one. This effect is emphasized by broadening the potential window (Fig. 8). Using a broad potential window permits to obtain large capacities but it is detrimental to the cycling stability. Nanosized TiO<sub>2</sub> showed better rate capabilities especially at very high rates. This can be explained by its higher specific surface area which involves a better contact between the electrode material and the electrolyte. The comparison of the electrochemical behaviour of these materials is given in Fig. 8.

Finally, the electrochemical performance of anatase TiO<sub>2</sub> anodes is strongly linked to the optimization of the active material's morphology. A mesoporous arrangement is a key morphology to optimize surface kinetics while retaining electrode stability, as demonstrated by the rate capabilities and capacity retention of electrodes with this morphology.

Besides the control of morphology, different strategies have been studied to improve the electrochemical performance of mesoporous anatase (see below).

**3.1.3 Carbon coating.** The carbon coating method has been proven to be very efficient to improve the electrochemical performance of LiFePO<sub>4</sub> or Li<sub>4</sub>Ti<sub>5</sub>O<sub>12</sub>, for example. In the case of anatase, the efficiency of the process is limited by the anatase to rutile transformation. Pfanzelt *et al.* prepared carbon-coated titania *via* a simple impregnation method and

observed a positive effect. A better cycling stability and high rate capacity could be achieved with the coated materials, and in addition, the TiO<sub>2</sub> crystallite growth is strongly reduced due to the presence of the carbon shell. However, the preparation of a pure anatase sample with an efficient carbon coating could not be implemented satisfactorily.<sup>185</sup>

Another approach has been studied by Ishii *et al.*<sup>186</sup> by introducing a triblock copolymer (Pluronic F127 (PEO<sub>106</sub>PPO<sub>70</sub>–PEO<sub>106</sub>)) during the precipitation step and using it as a carbon source. In this case no rutile formation has been observed and the composite maintained a high reversible capacity of 109 mAh g<sup>−1</sup> even at high current densities of 1000 mA g<sup>−1</sup>.

A similar approach has been presented by Park *et al.* to obtain carbon-coated TiO<sub>2</sub> nanotubes by hydrothermal reaction followed by post-calcination.<sup>187</sup> The complete crystallization of anatase was observed at 600 °C. The carbon coating suppressed the agglomeration of TiO<sub>2</sub> nanotubes and allowed better contact with the electrolyte leading to a better electrochemical performance.

Moriguchi *et al.*<sup>188</sup> also utilized carbon materials to enhance the performance of anatase TiO<sub>2</sub> materials. A c-SWNT-containing mesoporous TiO<sub>2</sub> sample was synthesized by a bicontinuous microemulsion-aided process. An aqueous HCl dispersion of c-CNTs as the water phase of the microemulsion and titanium tetrabutoxide as the Ti source was applied. The obtained composite exhibited a very high capacity at high rate. The authors were working in a narrow potential range (1.5–3 V) which made it difficult to compare their results with literature data.

Wang *et al.* combined TiO<sub>2</sub> anatase with functionalised graphene sheets in a self-assembly approach. The high rate capabilities were much higher with the composite electrode (96 mAh g<sup>−1</sup> at 30 C) in comparison to anatase electrodes (25 mAh g<sup>−1</sup>) with Super P as a conductive agent.<sup>189</sup>

**3.1.4 Conductive networks.** He *et al.* prepared TiO<sub>2</sub> nanotubes by using a hydrothermal process and coated the material with silver nanoparticles as the anode materials for lithium ion batteries by the traditional silver mirror reaction.<sup>190</sup> The results showed that the Ag additive decreased the polarization of the anode, and improved the high rate discharge capacity and cycling stability of TiO<sub>2</sub> nanotubes.

Guo *et al.* reported superior electrochemical performance of nanostructured mesoporous anatase TiO<sub>2</sub> incorporating an efficient hierarchical mixed conducting network.<sup>191</sup> The composite material was prepared with RuO<sub>2</sub>, providing highly conducting paths for electrons in a three-dimensional network. This nanosized network resulted in negligible diffusion times, enhanced local conductivities, faster phase transformation reactions, and hence appeared to be the key to the good power performance for the material. After 20 cycles at C/5 charging rate, a specific charge capacity of 214 mAh g<sup>−1</sup> has been observed. The specific charge capacity was still 91 mAh g<sup>−1</sup> at the very high rate of 30 C, which was nine times larger than that of mesoporous anatase spheres without inferior electronic wiring.

**3.1.5 Glassy-like phase.** Zhou *et al.* introduced a new concept in the design of an electrode material consisting of a self-organized, crystalline-glass mesoporous nanocomposite (CGMN).<sup>192</sup> The 5 nm frameworks of the CGMN were



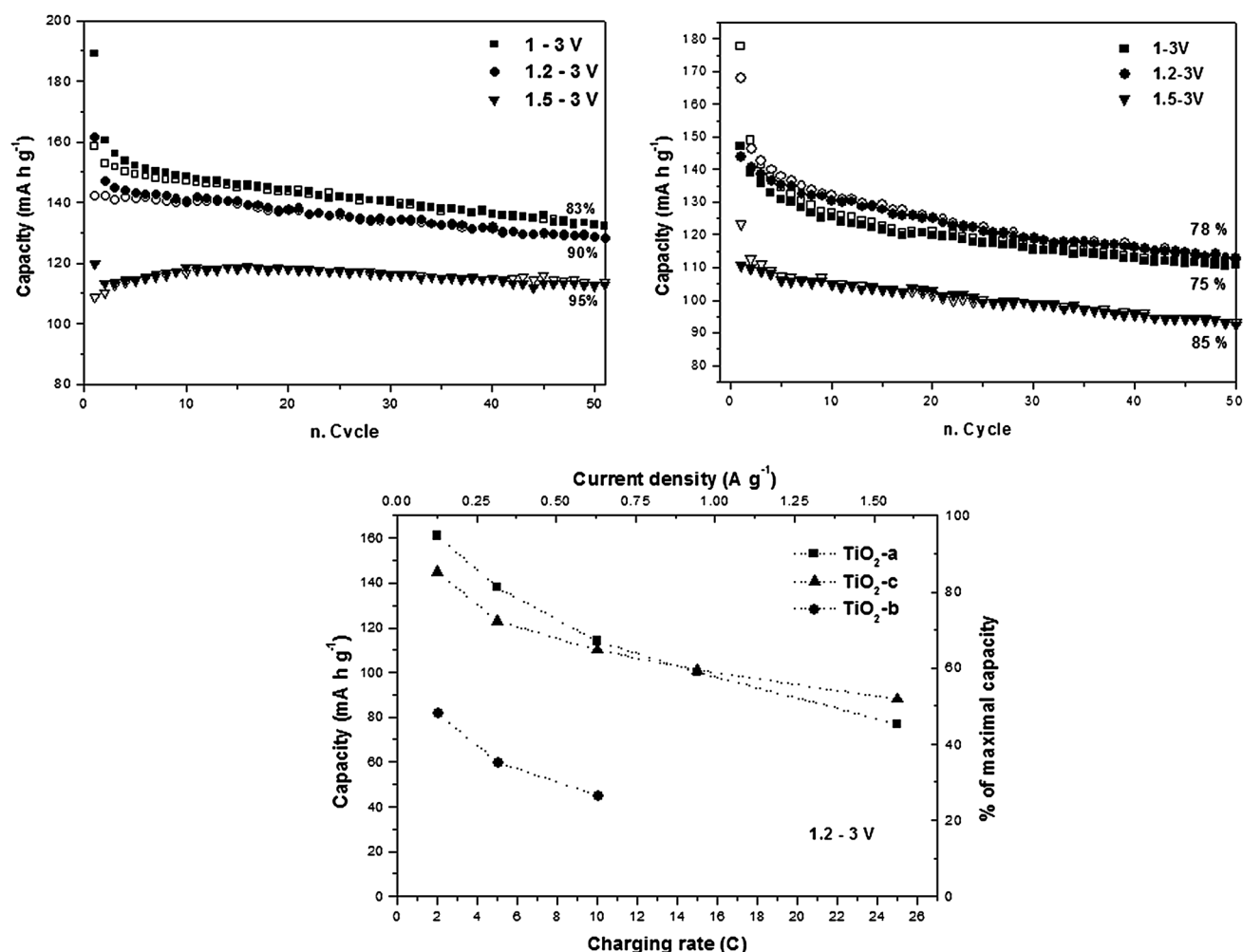


**Fig. 8** Top: Capacity of lithium insertion–extraction vs. charging-rate for mesoporous TiO<sub>2</sub> (left), TiO<sub>2</sub>-c (right) using 1.5–3 V; 1.2–3 V and 1–3 V potential windows. Bottom: Rate capabilities of mesoporous (TiO<sub>2</sub>-a), bulk (TiO<sub>2</sub>-b) and nanosized (TiO<sub>2</sub>-c) anatase TiO<sub>2</sub> materials using 1.2–3 V potential range (reprinted with permission from Kubiak *et al.*<sup>10</sup>).

assembled in a compact arrangement from electrode-active nanocrystals with a small quantity of glass phase. The 4 nm uniform mesochannels of the CGMN were filled with electrolyte solution to provide electrolyte and lithium-ion transport pathways throughout the material. The nanocomposites demonstrated a significant improvement in specific energy capacities at high current densities.

Erjavec *et al.* used two additives in order to improve the electrochemical performance of anatase TiO<sub>2</sub>.<sup>193</sup> The previously mentioned RuO<sub>2</sub> nanowiring as electron conductive material and silica as a suppressant of particle growth during heat treatment. The authors showed that both approaches improved the performance of anatase at high rates. The combination of both methods leads to an improvement of more than 70 mAh g<sup>-1</sup> at 60 C. The RuO<sub>2</sub> acted as an electron conductor and the silica played the role of a spacer between the titania nanoparticles allowing for better contact between the active material and the electrolyte.

**3.1.6 Metal coating.** Mancini *et al.* proposed an optimization of the electrochemical properties of mesoporous anatase electrodes in lithium-ion batteries by coating the electrodes

with a thin metallic Cu or Sn layer *via* physical vapour deposition (PVD).<sup>194,195</sup> The new metal–anatase composite electrodes show improved kinetics for the Li insertion–extraction reactions and excellent electrochemical performances in terms of capacity, stability and fast-cycling abilities. The surface modification leads to a significant enhancement in the electrochemical behaviour regarding higher reversible capacities, less polarization, lower irreversible capacity during the first cycle, and higher high rate performances. Experimental evidences show that the main effect of the surface layer is related to an enhanced lithium insertion–extraction on the plateau, *i.e.*, the diffusion-controlled two-phase mechanism (Fig. 9, right). At the faster charge–discharge rate (30 C, 5 A g<sup>-1</sup>) the delivered capacities were 94, 132 and 143 mAh g<sup>-1</sup> for the uncoated, the Cu- and the Sn-coated anatase electrodes, respectively.

The authors focus also on the long-term stability. The capacities after 200 cycles at 4 C (1.34 A g<sup>-1</sup>) were 123, 147 and 142 mAh g<sup>-1</sup> for the uncoated, the Cu- and the Sn-coated anatase electrode, respectively, with capacity retention of about 80% for all electrodes. The better electrochemical performances are probably related to favourable surface interactions and faster lithium dissolution rate that improves the

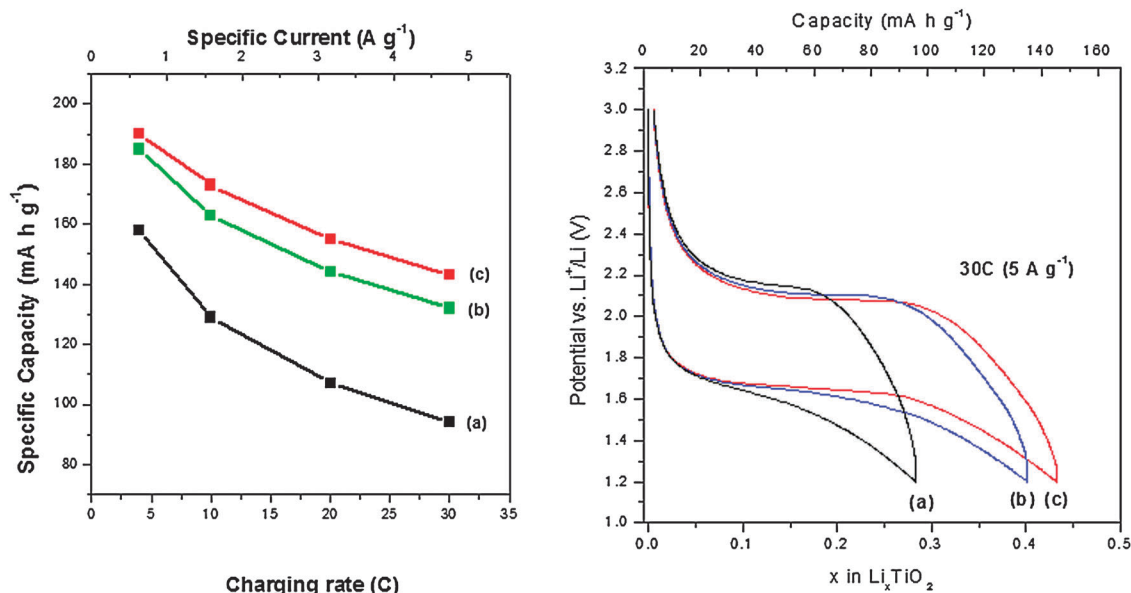


**Fig. 9** Variation of reversible capacity of uncoated (a), Cu (b) and Sn (c) coated TiO<sub>2</sub> electrode as a function of charge/discharge rate. Potential range 1.2–3 V (left). Comparison of galvanostatic Li insertion–extraction of uncoated (a), Cu (b) and Sn (c) coated mesoporous TiO<sub>2</sub> electrodes at 30 C (right) (reprinted with permission from Mancini *et al.*<sup>195</sup>).

lithium transfer at the interface. Moreover, PVD is an easy modification procedure, which appears to be a very promising optimization method for the development of high rates performance materials for lithium-ion batteries.

As discussed, anatase appears to be a very promising anode material for Li-ion batteries with a strong connection of the performance to its morphological properties. In this context mesoporous materials have been paid particular attention since they are effective in increasing the electrode stability and the Li insertion capacity especially at high charge–discharge rates. In addition different approaches have been developed in order to improve the electrochemical performance. Recently, different groups have investigated TiO<sub>2</sub> anatase as anode material in combination with LiFePO<sub>4</sub> as cathode material.<sup>196,197</sup> The full cell operated at an average potential of 1.6 V and demonstrated negligible fade after more than 700 cycles at measured 1 C rate.<sup>196</sup> Although the Li-ion batteries based on LiFePO<sub>4</sub>–TiO<sub>2</sub> combination exhibit lower energy density compared to traditional Li-ion batteries, they offer long life times and high safety, which are critical for stationary applications.

### 3.2 TiO<sub>2</sub> rutile

**3.2.1 Experimental and theoretical studies of the lithium insertion mechanism of rutile.** The lithium insertion–extraction into/from rutile is highly anisotropic. Along the *c*-axis the lithium diffusion is fast while it proceeds very slow in the *ab* plane.<sup>198</sup> The theoretically calculated diffusion coefficients of lithium along the *c*-axis and in the *ab*-plane are 10<sup>-6</sup> cm<sup>2</sup> s<sup>-1</sup> (*D<sub>c</sub>*) and 10<sup>-14</sup>–10<sup>-15</sup> cm<sup>2</sup> s<sup>-1</sup> (*D<sub>ab</sub>*), respectively.<sup>199–201</sup> In micron-sized rutile the very slow diffusion in the *ab*-plane impedes the lithium ions to access the thermodynamically favourable octahedral sites. Additionally Li<sup>+</sup> pairs can block the *c*-channels and hinder further lithiation because of the poor diffusion in the *ab*-plane.<sup>200,202</sup> This kinetic restriction is

reported to be the reason why micron-sized rutile can only insert little amounts of lithium at room temperature and it was additionally suggested that this kinetic limitation is linked with mechanical strains reduced with decreasing particle size.<sup>138,203</sup> Experimental results of the lithium diffusion coefficient by Bach *et al.*<sup>204</sup> using impedance spectroscopy were in between 7 × 10<sup>-8</sup> and 10<sup>-9</sup> cm<sup>2</sup> s<sup>-1</sup> for low lithium contents (Li<sub>x</sub>TiO<sub>2</sub>, *x* ≤ 0.4) and 5 × 10<sup>-10</sup> cm<sup>2</sup> s<sup>-1</sup> at higher ones (0.4 < *x* < 0.8). At higher temperatures (~120 °C) the lithium diffusion in the *ab*-plane is enhanced (*D<sub>ab</sub>* = 10<sup>-12</sup> cm<sup>2</sup> s<sup>-1</sup>) leading to a reversible insertion of ~0.5 lithium per TiO<sub>2</sub>.<sup>140,200,205,206</sup>

Three distinct regions can be observed during the first discharge (Fig. 10). The first step of lithium insertion is an initial potential drop from open circuit voltage to about 1.4 V. After the first initial potential drop a plateau can be observed at 1.4 V. The third part corresponds to a second plateau at 1.1 V.<sup>119</sup> Structural changes have been observed at 1 V by different groups, which are still under controversial discussion in different theory- and experiment-based publications. During charge the galvanostatic curve evidences a slope like behaviour which remains upon further charge–discharge cycles.

The main reason for the uncertainty in the lithium insertion mechanism is the lack of proper analytical *in situ* or *ex situ* analysis techniques that can detect the changes in the material, *e.g.* regarding the phases formed during electrochemical lithium insertion. Especially the fact that nanosized rutile loses crystallinity during the lithium insertion makes it difficult to get reliable data from XRD. Therefore many groups applied chemical lithiation techniques to characterize the lithiated Li<sub>x</sub>TiO<sub>2</sub> formed.<sup>5,8,207,208</sup> However, it has to be considered that the chemical lithiation may lead to different structures compared to the electrochemical lithium insertion process in the lithium ion cell. In Section 4 investigations regarding the mechanism of the lithium insertion–extraction are described in more detail.

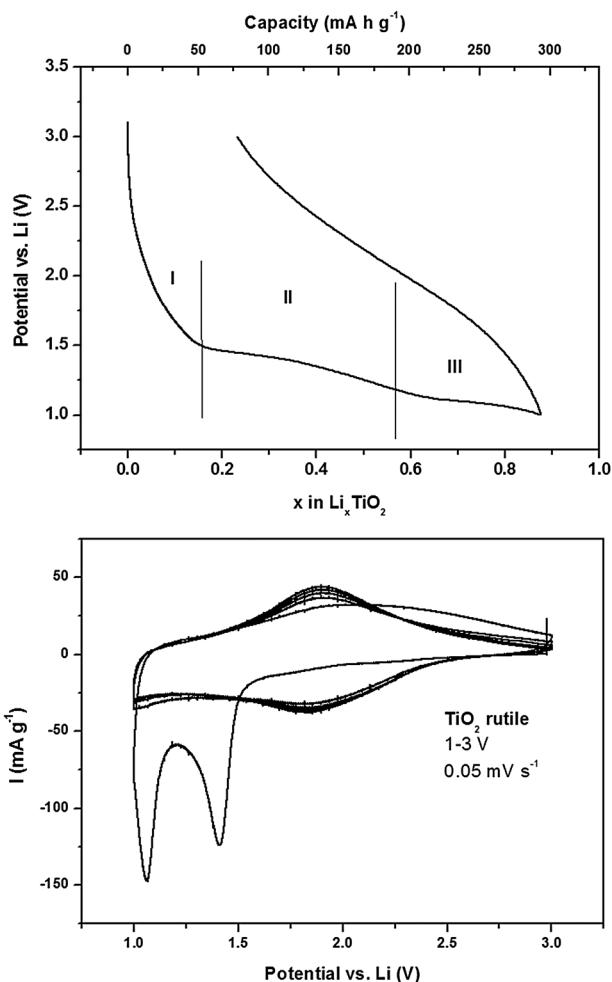


**Fig. 10** (Top) Galvanostatic curves of  $\text{TiO}_2$  rutile C/5 between 1 and 3 V vs.  $\text{Li}^+ - \text{Li}$ . 1st cycle. (Bottom) Cyclic voltammetry for rutile  $\text{TiO}_2$  in 1 M  $\text{LiPF}_6$  EC/DMC (1–1, w/w), scan rate  $0.05 \text{ mV s}^{-1}$  (reprinted from Kubiak *et al.*<sup>119</sup> with permission from Elsevier).

**3.2.2 Performance and properties of  $\text{TiO}_2$  rutile as anode material for lithium ion batteries.** The earliest investigations of lithium insertion into  $\text{TiO}_2$  rutile were reported by Ohzuku *et al.* in 1979.<sup>209</sup> They used rutile as cathode material in lithium primary batteries in simple discharge tests but abandoned the material in favour of anatase, which exhibited a higher cell voltage and capacity. Bonino *et al.*<sup>210</sup> only performed preliminary experiments with  $\text{TiO}_2$  rutile and anatase in secondary lithium ion cells and decided to discard rutile for the same reasons, although a considerable amount of lithium ions ( $\sim 0.38$  mol lithium per mol  $\text{TiO}_2$ ) could be inserted in the potential window of 1–3 V. These two publications in addition to the findings of Macklin and Neat<sup>205</sup> and Zachau-Christiansen *et al.*,<sup>140</sup> who reported a negligible capacity of rutile electrodes at room temperature while rutile worked quite well at elevated temperatures ( $120^\circ\text{C}$ ), led to the assumption that rutile is not suitable or less attractive for lithium ion batteries than anatase. Therefore a lot more research was devoted to anatase, while only few publications investigated the properties of rutile. Till 2005 only few experimental data were published. Kavan *et al.* reported a lithium

insertion into mesoscopic rutile of 0.35 mol lithium per  $\text{TiO}_2$  (1.2–3 V), while Wagemaker *et al.* reported of a  $\text{Ti}^{+3.6}$  oxidation state detected by XANES, which indicates the formation of a  $\text{Li}_{0.4}\text{TiO}_2$  phase.

In 2006, Hu *et al.* showed that the amount of inserted lithium into rutile could be significantly increased by using nanomaterials.<sup>144</sup> They reported a lithium insertion of 0.8 mol lithium into nanosized needle-like rutile crystals (10 nm diameter, 40 nm length) at room temperature in the first cycle in contrast to 0.1–0.25 mol lithium for micron-sized materials. The reversible lithium insertion–extraction in the following cycles was about 0.5 mol, which is comparable to  $\text{TiO}_2$  anatase. After 50 cycles at C/20 the capacity slightly decreased from 160 to 150  $\text{mAh g}^{-1}$ . The finding that the lithium insertion capability of rutile is strongly dependent on the crystallite size aroused a lot of interest followed by many publications in the following years.

The excellent lithium storage properties of nanosized rutile were confirmed by Reddy *et al.*<sup>145</sup> who evidenced a lithium insertion of 1 mol lithium per  $\text{TiO}_2$  in the first cycle discharge and 0.55 mol in the following charge using sol–gel synthesized nanosized rutile. Additionally, the results were compared with commercial bulk rutile which evidenced a poor electrochemical behaviour and inserted only 0.06 mol lithium.

Jiang *et al.*<sup>211</sup> reported an excellent reversible insertion–extraction of 0.6–0.7 mol lithium cycling with  $0.05 \text{ A g}^{-1}$  (about C/6) using commercial rutile nanopowders with a particle size of 15 nm, while bigger particles with 30 and 300 nm only insert about 0.4 and 0.15 mol lithium, respectively. Additionally, the nanopowder exhibits 132 and 118  $\text{mAh g}^{-1}$  after 100 cycles at 5 and 10  $\text{A g}^{-1}$  (about 16 and 32 C).

Baudrin *et al.*<sup>203</sup> investigated the different lithium insertion–extraction behaviour of nanosized and bulk rutile materials as well as the mechanism by *in situ* XRD. While the bulk material inserted only small amounts of lithium (0.03 mol per  $\text{TiO}_2$ ) the nanosized  $\text{TiO}_2$  (50 nm) could reach the composition of  $\text{Li}_{0.23}\text{TiO}_2$  in the first discharge down to 1 V and 0.11 mol lithium could be extracted during charge. Decreasing the crystallite size to 10 nm by using nanorods (10 nm diameter, 200 nm length) increased the amount of inserted lithium up to 0.85 mol in the first discharge and a reversible lithium insertion–extraction of 0.5 mol.

A study of lithium insertion into high surface mesoporous rutile with residual amounts of anatase was done by Liu *et al.*<sup>212</sup> The investigated material can reversibly accommodate 0.55 mol lithium ( $185 \text{ mAh g}^{-1}$ ) at C/5 and shows a capacity loss of only 10% after 100 cycles.

Qiao *et al.* published two performance studies<sup>213,214</sup> on hierarchical porous rutile  $\text{TiO}_2$  nanorod microspheres and flowerlike rutile  $\text{TiO}_2$  nanorods. The microspheres inserted up to 0.73 mol lithium ( $\text{Li}_{0.73}\text{TiO}_2$ ,  $246 \text{ mAh g}^{-1}$ ) during the first charge at a C/10 and retained  $192 \text{ mAh g}^{-1}$  after 30 cycles. In comparison to the microspheres the nanorods can insert less lithium and evidence a charge capacity of  $227 \text{ mAh g}^{-1}$  in the first cycle (C/10) and  $183 \text{ mAh g}^{-1}$  after 30 cycles.

Performance analysis of sol–gel synthesized  $\text{TiO}_2$  rutile nanowhiskers using a glycerol-modified titanium precursor and an anionic surfactant were done by Kubiak *et al.*<sup>119</sup> The material is characterized by a high BET surface area of  $181 \text{ m}^2 \text{ g}^{-1}$  and shows a reversible capacity of  $190 \text{ mAh g}^{-1}$  (C/5,  $0.067 \text{ A g}^{-1}$ )



combined with an excellent high rate capability of  $100 \text{ mAh g}^{-1}$  at  $30^\circ\text{C}$  ( $\sim 10 \text{ A g}^{-1}$ ).

An interesting material was prepared by Wang *et al.*<sup>189</sup> They combined  $\text{TiO}_2$  rutile with functionalised graphene sheets in a self-assembly approach improving especially the high rate capacity ( $87 \text{ mAh g}^{-1}$  at  $5 \text{ A g}^{-1}$ ) in comparison to rutile electrodes with Super P ( $35 \text{ mAh g}^{-1}$ ) as a conductive agent. The electrodes with 0.5 wt% of functionalised graphene sheets exhibit slightly better capacities at low rate and a strong improvement at high rates compared to the electrodes with 10% Super P. Therefore, the overall energy density and power density can be significantly increased by replacing Super P with functionalised graphene sheets.

Cycling rutile nanowhiskers in the larger potential window of 0.1–3 V in comparison to the standard 1–3 V one leads to an increase of the reversible capacity up to  $315 \text{ mAh g}^{-1}$  at C/5 ( $67 \text{ mA g}^{-1}$ ), which is close to the theoretical value of  $335 \text{ mAh g}^{-1}$  ( $\text{Li}_1\text{TiO}_2$ ).<sup>215</sup> Additionally, the high rate capacity is significantly increased to  $196 \text{ mAh g}^{-1}$  at 5 C ( $1.68 \text{ A g}^{-1}$ ). Although the discharge down to 0.1 V leads to electrolyte decomposition (EC/DMC) causing a SEI formation at potentials of  $\sim 0.8 \text{ V}$ <sup>32,215</sup> and a lower relative cycling and rate stability, the absolute capacity and energy gain overcompensate the disadvantages. Thermal analysis of the lithiated and delithiated rutile nanowhiskers revealed the safe character of rutile electrodes in combination with the electrolyte.<sup>32</sup> The samples exhibited no oxygen evolution and a low exothermic behaviour up to  $350^\circ\text{C}$ , while the compared graphite samples showed strong exothermic reactions known from several other studies (Fig. 11).<sup>216–219</sup>

Investigations of the low temperature behaviour of this nanowhisker showed excellent values and  $138$  and  $77 \text{ mAh g}^{-1}$  could be reached at  $-20$  and  $-40^\circ\text{C}$ , respectively (0.1–3 V, C/5).<sup>220</sup> These capacity values of the unmodified rutile electrode outnumber graphite electrodes, which maintain only  $26$  ( $-30^\circ\text{C}$ )<sup>221</sup> and  $45 \text{ mAh g}^{-1}$  ( $-20^\circ\text{C}$ )<sup>222</sup> (Fig. 12).

The electrochemical properties of ultra-fine rutile nanoparticles synthesized *via* a wet chemical method in acidic media were investigated by Chen *et al.*<sup>223</sup> The small crystals of 2–5.8 nm can reach a reversible capacity of  $198 \text{ mAh g}^{-1}$  after 20 cycles at a charge–discharge current of  $0.17 \text{ A g}^{-1}$  and  $77 \text{ mAh g}^{-1}$  at  $5.1 \text{ A g}^{-1}$ . After an initial capacity loss the ultra-fine rutile nanoparticles have a coulombic efficiency close to 100%.

Rutile nanoneedles have been synthesized by Khomane *et al.* using a reverse microemulsion-mediated sol–gel method.<sup>224</sup> The mild synthesis results in high surface area mesoporous rutile with a reversible capacity of  $128 \text{ mAh g}^{-1}$  at C/10 after  $305 \text{ mAh g}^{-1}$  in the first cycle.

## 4. Structural properties of rutile nanorods for lithium-ion batteries

### 4.1 TEM investigations on delithiated very small rutile nanorods

Kubiak *et al.*<sup>119</sup> demonstrated that rutile nanoparticles, sol–gel synthesized with a glycol modified titania precursor and an anionic surfactant, can be cycled reversibly between 1.2–3 V. As the material showed high charging/discharging capabilities,

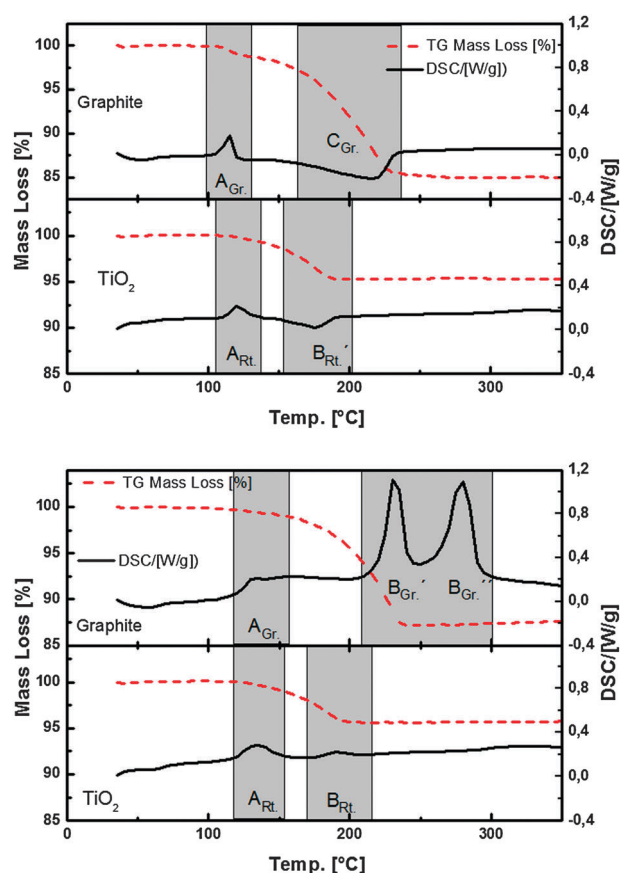


**Fig. 11** DSC/TG curves of the (a) lithiated graphite (top) and rutile (bottom) electrodes and the (b) delithiated graphite (top) and rutile (bottom). Positive peaks are exothermic and negative ones endothermic (reprinted from Pfanzelt *et al.*<sup>32</sup> with permission from Elsevier).

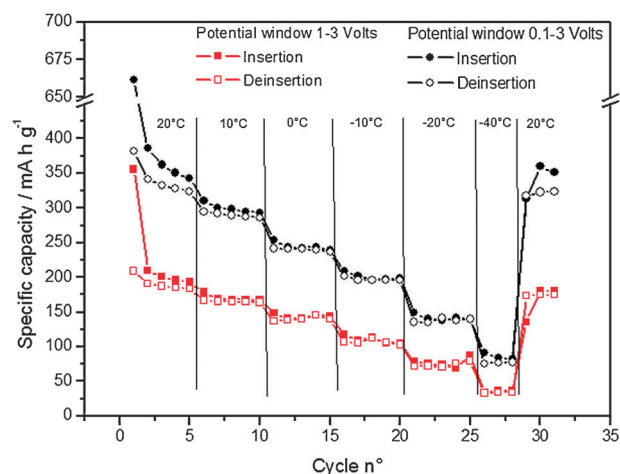


**Fig. 12** Specific capacities obtained at different temperatures (C/5 rate) in two (0.1–3 V and 1–3 V) investigated potential windows (reprinted from Marinaro *et al.*<sup>220</sup> with permission from Elsevier).

the structural properties of this material and the response to Li insertion–extraction will be discussed in more detail in the following sections.

Hörmann *et al.*<sup>225</sup> carried out *ex situ* TEM studies on as synthesized and cycled rutile nanorods, fabricated from a

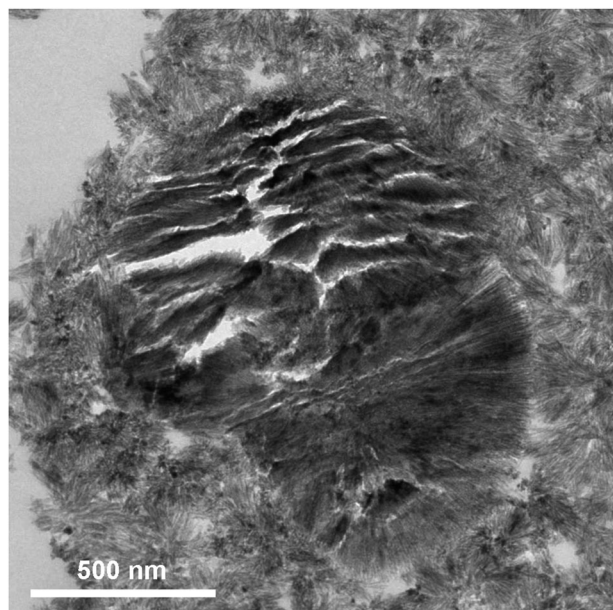


**Fig. 13** The bright-field TEM image shows the rutile nanorods agglomerated in small bunches and in spherical flowerlike structures.

glycolated precursor. After the electrochemical cycling experiments between 1–3 V, the powder was regained from the dismantled electrode. In order to correlate structural changes with the observed redox reactions and the number of cycles, the study contained as synthesized samples, and samples after the first cycle from 1 to 3 V, from 1.2 to 3 V, and after two and five cycles from 1 to 3 V.

In the following we show bright-field TEM and aberration-corrected high-resolution TEM images obtained from a TITAN 80–300 operated at 300 kV of as-synthesized and cycled samples. The bright-field TEM image in Fig. 13 shows the agglomerated rutile nanorods as obtained in the as-synthesized form and from the cycled samples. The nanorods agglomerate to small bunches and to flower-like spherical structures. The microstructure, *i.e.* the nanorod morphology, was preserved during electrochemical cycling.

The average nanorod diameter determined from the TEM images was 5–10 nm. In all samples three different types of nanorods were observed, namely nanorods with good crystallinity, nanorods with numerous lattice defects and bent nanorods. The nanomorphology was identical for the as-synthesized and all the cycled samples.

In the as-synthesized and in all of the cycled samples nanorods with good crystallinity were observed. These nanorods revealed a corrugated surface with hillocks of 1–2 nm baseline length as shown in Fig. 14 and 15 or terrace steps as shown in Fig. 16 and 17. Hillocks and terraces facilitate the diffusion of Li into the rod because they offer openings to the  $\langle 001 \rangle$  channels, the principle diffusion direction of Li. According to the studies on surface lattice expansion it can be expected that the initial pure  $\text{TiO}_2$  lattice spacings are larger than in bulk crystals. Larger lattice spacings increase the size of the diffusion channels and in this way they reduce the strain imposed on the lattice by Li insertion. The hillocks increase the surface area and are expected to enhance Li diffusion and

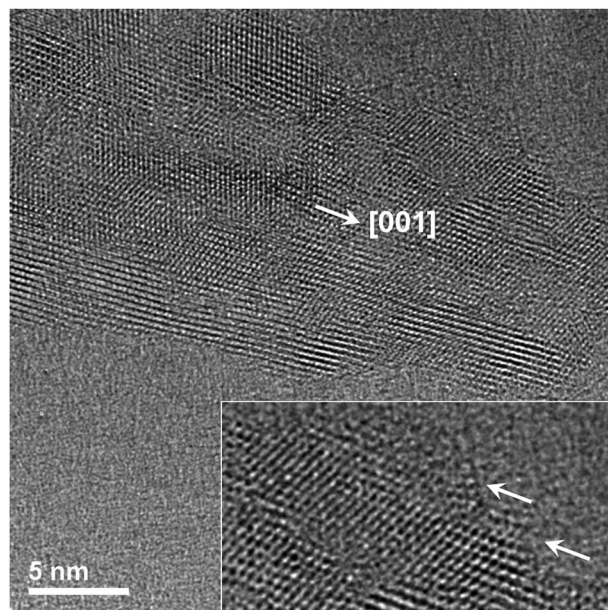


**Fig. 14** The aberration-corrected high-resolution TEM image shows an as-synthesized rutile nanorod with surface corrugations. The arrows in the enlargement point to the facets which offer openings to the  $c$  channels.

Li incorporation. The stress arising from Li insertion can easily be elastically relaxed *via* the surface as the hillocks can expand the crystal lattice laterally and outwards. According to these considerations, the hillocks and terraces are expected to facilitate the reversible Li incorporation.

In the as-synthesized and in all the cycled samples nanorods with a modular nanostructure were observed. These nanorods

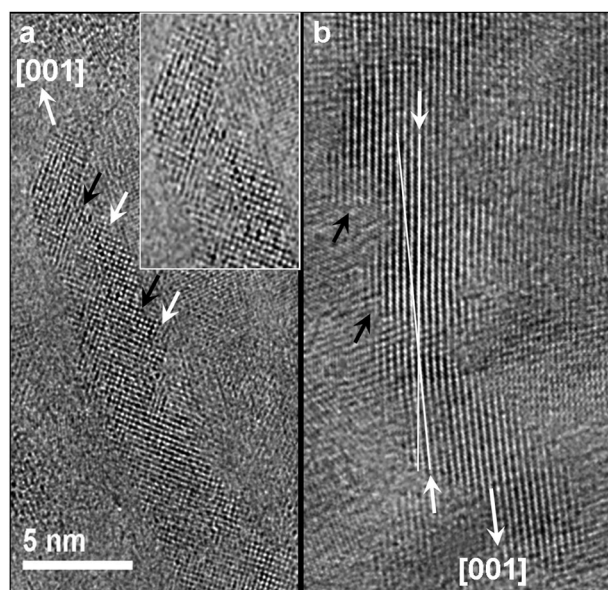


**Fig. 15** (a) The aberration-corrected high-resolution TEM image micrograph shows a rutile nanorod after the first cycle 1–3 V. The white arrows point to hillocks with a base line of *ca.* 2 nm. The black arrows point to troughs. The arrow in the enlarged inset points to the facets which offer openings to the  $c$  channels. (b) The HRTEM micrograph shows a rutile nanorod with severe surface corrugations and lattice bending. The black arrows point to the hillocks.



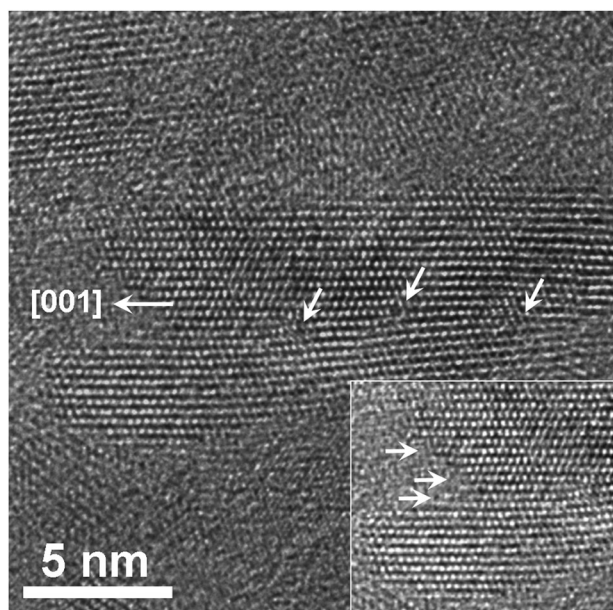


**Fig. 16** The aberration-corrected high-resolution TEM image shows two rutile nanorods after the first cycle 1.2–3 V. The arrows point to the small angle grain boundary which connects the two nanorods. The arrows in the inset point to the terrace steps which offer openings to the c channels.

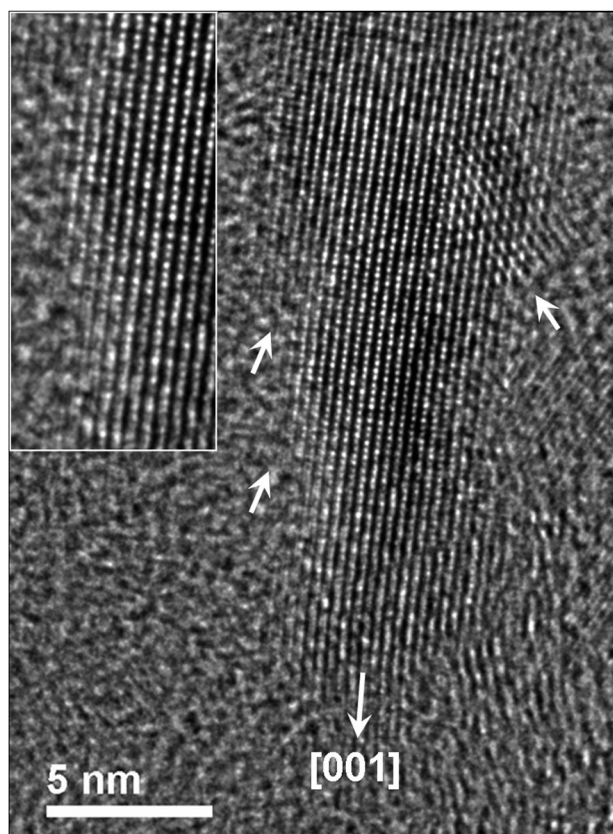


**Fig. 17** The aberration-corrected high-resolution TEM image shows a rutile nanorod after the five cycles 1–3 V. The arrows point to the terrace steps which offer openings to the c channels.

revealed lattice defects such as grain boundaries as shown in Fig. 18. The enlargement in Fig. 18 shows a nanorod built-up

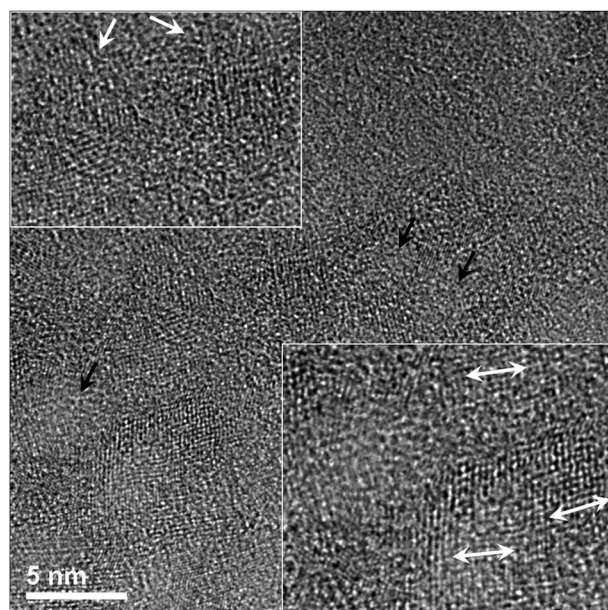


**Fig. 18** The aberration-corrected high-resolution TEM image shows an as-synthesized rutile nanorod of modular structure. The black arrows point to voids in the nanorod. The arrows in the lower enlargement show that the nanocrystallites are tilted by small angles. The arrows in the upper enlargement point to surface corrugations caused by the nanocrystalline building blocks.

of modularly arranged nanocrystallites enclosing pores. These crystallites increase significantly the total surface area of the nanorod and have the same ability for enhanced Li storage as discussed above for the hillocks. Crystallographic defects are known as locations for impurity segregation, *i.e.* sites which support the increased Li storage capability.

In the as-synthesized and in all of the cycled samples bent nanorods were observed. Prior to the TEM investigation the samples were embedded in a resin (EPON 812) of medium hardness which is used to prepare artifact free delicate biological samples. The bending is therefore considered as a property of the particle. Applying Hooke's law to the bent particles shown in Fig. 19 and 20 would result to a force of 17.9 N and 3.5 N, respectively which is needed to bend the particles. As already pointed out, a rigid body approach with bulk values of the elastic properties does not lead to physically reliable results. The observed bending clearly indicates the softening. A dislocation may have caused stress-induced bending of the particle shown in Fig. 21 in analogy to the Eshelby twist.<sup>226,227</sup> The torque of a whole nanowire or chiral branched nanowire caused by screw dislocation is called Eshelby twist. Although no direct evidence for a dislocation was found, the assumption is supported by (i) the contrast changes at the kink in Fig. 19 and (ii) the shape of the bent nanorod shown in Fig. 15b, which corresponds to the growth model for twisted nanorods proposed by Amelinckx.<sup>228</sup>

Fig. 21 shows the electron diffraction patterns of the as-synthesized and five times 1–3 V cycled powders. The rings in both diffraction patterns could be indexed as rutile, thus proving the reversible Li insertion–extraction in the nanorods. The TEM and Cs-corrected HRTEM investigations clearly



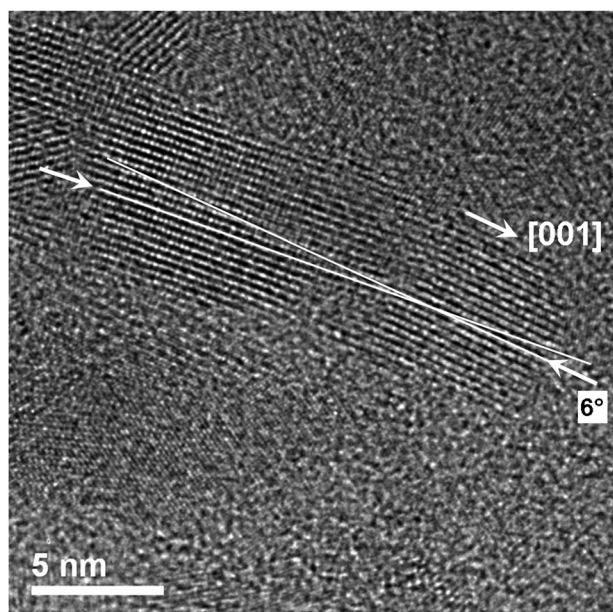


**Fig. 19** The aberration-corrected high-resolution TEM image shows a bent as-synthesized rutile nanorod which demonstrates the enhanced elasticity. The bending might be caused by the stress field of a dislocation.

showed that the pure rutile nanorods remain crystalline even after multiple charging–discharging cycles. These results demonstrate that the reaction towards  $\text{Li}_x\text{TiO}_2$  and the associated redox reactions were fully reversible.

#### 4.2 Phase transformations upon lithiation: pathways and boundary conditions

These experimental findings contradict the observations so far published in the literature. Studies on the Li insertion into rutile nanoparticles of a size larger than 10 nm discuss two different pathways for a phase transformation, each of them presenting an intermediate phase as a result of a solid solution type transition.

The first transition pathway was described by Borghols *et al.*<sup>229</sup> in an X-ray and neutron study. This mechanism is based on the first proposals by Macklin and Neat<sup>205</sup> and matches with earlier experimental work.<sup>144,145</sup> Theoretical work that predicted the transformation to a layered structure was started by Benco *et al.*<sup>230</sup> and extensively performed by Koudriachova *et al.*<sup>231</sup> According to this mechanism the tetragonal rutile transforms at  $x = 0.5$  into an intermediate monoclinic  $\text{Li}_{0.5}\text{TiO}_2$ . This transition is based on the ordered incorporation of Li into the rutile lattice and leaves the connectivity of the Ti–O network unaffected, *i.e.* no Ti–O bond breaking was necessary. As a result the unit cell volume is increased by 6.3%.

With a further increasing amount of Li ions to  $x = 0.85$ , this lattice becomes unstable, such that Ti–O bonds break up and the lattice rearranges into a layered monoclinic  $\text{LiTiO}_2$  structure with alternating  $\text{TiO}_2$  octahedra and Li monolayers. Borghols *et al.* expect this structure to be stable up to  $x = 1$ . The intermediate phase was observed for nanosized rutile only. Micron-sized particles directly transformed into the layered structure at a composition of  $x = 0.43$ .

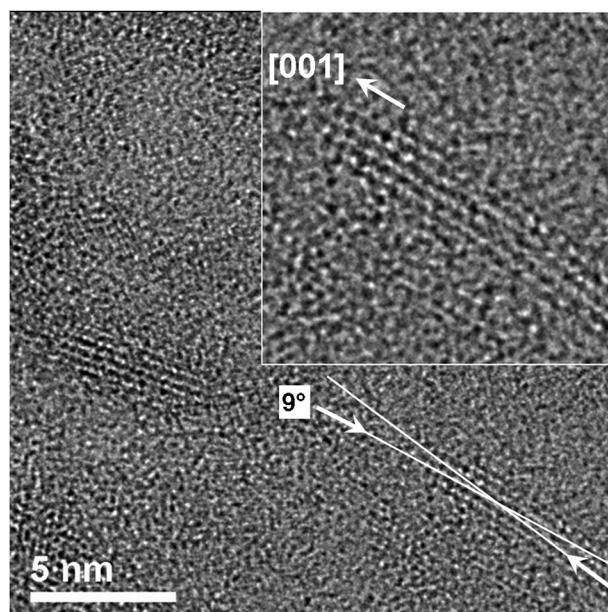


**Fig. 20** The aberration-corrected high-resolution TEM image shows a very thin bent rutile nanorod after five cycles 1–3 V which demonstrates the enhanced elasticity. The enlargement in the inset shows the bent lattice planes.

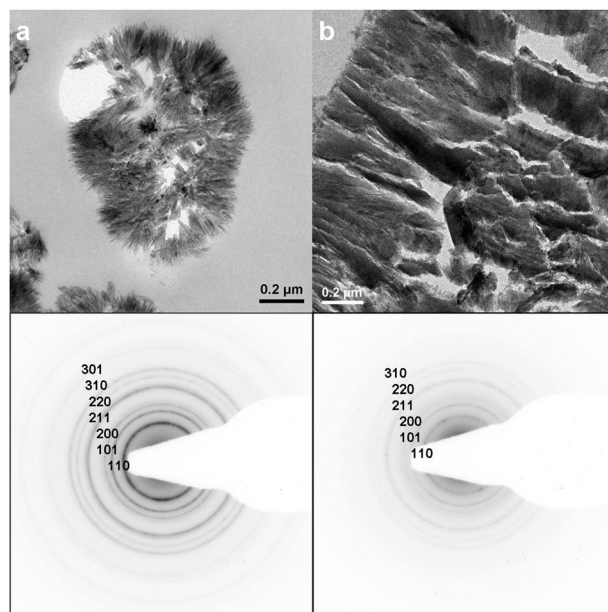


**Fig. 21** The bright-field TEM images show (a) the as-synthesized and (b) the five times 1–3 V cycled nanorods with the corresponding electron diffraction patterns. Both diffraction patterns could be indexed as rutile. The amorphous background in the ring pattern of the cycled sample is from the residual binder.

Reddy *et al.*<sup>145</sup> studied the phase transformation dependent on the particle size. By annealing 5 nm rutile nanorods they obtained particles with 6, 7.5, 11.4 and 14.7 nm diameter. They performed *ex situ* XRD measurements of the fully discharged electrode, which shows two peaks corresponding to a hexagonal  $\text{Li}_x\text{TiO}_2$ . This structure is retained upon charging, *i.e.* delithiation, indicating an irreversible phase transformation.

A crystallite size dependent effect at fast voltammetry experiments was observed by Milne *et al.* The effect vanished at reduced charging rates, indicating the charge rate, *i.e.* kinetic limitations as a second parameter for structural stability. In this study, lithium was inserted into different rutile samples with 4–50 nm in diameter. They observed increasing unit cell volumes at decreasing crystallite size as published by Luca *et al.*<sup>232</sup>

Milne *et al.* proposed that quantum size effects, *i.e.* quantum confinement, might influence the particle behaviour during charging–discharging.<sup>233</sup> The intercalation potential increases with decreasing crystallite size, which contradicts quantum size effect considerations and is possibly related to a facilitated lattice distortion. What is more, the particle size of Milne *et al.* is much larger than the Bohr radius of rutile.

Quantum confinement in titania nanoparticles was disputed, *e.g.* by Monticone *et al.*,<sup>234</sup> who pointed out that for a strong exciton confinement particle radius  $R$  must be smaller than the Bohr radius. Hörmann *et al.*<sup>235</sup> determined the Bohr radius of sol–gel synthesized anatase nanoparticles of 8.8 nm and 11.1 nm diameter to 2.35 nm. The particles showed pure bulk behaviour. Monticone, in the above-mentioned study, could not detect band gap energy shifts for particles with 1.5 nm diameter. The Bohr radius for rutile is considered to be significantly smaller than for anatase, even in the presence of electron donors.<sup>236</sup> Kormann *et al.*<sup>237</sup> calculated the Bohr radius of rutile for different literature values of the effective electron mass and obtained values between 0.75 and 1.9 nm. Hasiguti<sup>238</sup> determined the rutile Bohr radius to 0.76 nm from the effective electron mass and the dielectric constant. Bacsá *et al.*<sup>239</sup> calculated the Bohr radius of rutile from spectroscopic data to 0.26 nm. In view of these data, any quantum confinement effects can be ruled out to influence the phase transformations during Li insertion.

Kavan *et al.*<sup>206</sup> investigated the lithium storage capability of a commercial rutile powder (PK 5565, Bayer, average particle size 10–50 nm) at 120 °C. The rutile structure was retained up to the formation of a  $\text{Li}_x\text{TiO}_2$  with  $x = 0.25$ . At  $x = 0.5$  they observed an unknown intermediate structure that transformed to the hexagonal  $\text{Li}_{0.5}\text{TiO}_2$ . Macklin and Neat<sup>205</sup> observed the identical transition path in a commercial rutile powder. The hexagonal phase has shown reversibility in the composition range  $0.5 < x < 1$ .

The second transition pathway first described by Baudrin *et al.*<sup>203</sup> involved a solid solution type transformation of the tetragonal rutile to an intermediate phase leading to a unit cell volume increase of 9.7% in 10 nm thick  $\text{Li}_{0.6}\text{TiO}_2$  nanorods. At further lithiation the material is irreversibly transformed to cubic rock salt  $\text{LiTiO}_2$ . The irreversible phase transitions were in particular observed for particles larger than 10 or 20 nm diameter.

C. M. Wang *et al.*<sup>240</sup> used mechanical milling in order to lithiate nanosized rutile. This treatment transformed the nanorods into agglomerates of apparently equiaxed/isotropic crystallites. As a result they observed a cubic  $\text{LiTiO}_2$  in rock-salt structure. The structural transformation from the rutile to the rock-salt lattice requires the break-up of chemical bonds for the rearrangement of atoms. The mechanically induced transition from the rutile to the rock-salt structure was thus considered to be irreversible.

D. Wang *et al.*<sup>212</sup> lithiated nanosized rutile, containing 5% anatase in an electrochemical cell. The material was cycled

from 3 to 1 V. After 100 cycles they indexed the electron diffraction pattern as cubic  $\text{LiTiO}_2$ . TEM images showed that the nanorod morphology was retained after cycling. Hence, in this study the transition to the cubic rock-salt structure is independent of the particle size. The cyclic voltammogram shows a successive flattening of the peak which correlates with the first redox reaction. The peak indicating the second redox reaction remains stable during all cycles.

Vijayakumar *et al.*<sup>241</sup> performed a hydrothermal reaction at 180 °C in order to chemically lithiate a rutile sample. Upon lithium insertion of 0.12 mol  $\text{Li}_{0.12}\text{TiO}_2$ , the rutile structure is preserved without significant changes. At a composition of  $\text{Li}_{0.44}\text{TiO}_2$  a spinel type phase is present, while further lithiation up to  $\text{Li}_{0.88}\text{TiO}_2$  leads to the formation of a rocksalt type phase.

Koudriachova *et al.*<sup>202</sup> studied the behaviour of nanoscale rutile with a spaghetti-like shape in comparison to the bulk rutile using *ab initio* simulations. On the nanoscale the boundary of the single phase reaction, displayed at low Li-concentrations in the bulk, shifts to higher Li-concentrations enabling an alternative structural evolution upon intercalation. While lithium insertion into bulk rutile leads to the formation of monoclinically distorted rutile the nanoscale material transforms into a spinel phase.

The mechanistic studies of the lithium insertion into  $\text{TiO}_2$  rutile are inconsistent and the proposed phase transformations or deformations are controversially discussed in different theoretical and experimental publications. The main reason is the lack of proper analytical *in situ* or *ex situ* techniques which can detect the phases formed by electrochemical lithium insertion in a lithium ion cell. Recently developed TEM holders designed in order to study the Li insertion on an electrically contacted sample with a liquid electrolyte will be able to track the phase transformation and to compare the results from chemical and electrochemical lithiation.<sup>242–244</sup>

### 4.3 Size-dependent materials properties

The Li storage capability is generally considered to increase with decreasing particle diameter. Further materials properties, which govern the Li incorporation process, are first volume properties, such as Li diffusion through the rutile lattice, lattice spacings, and elasticity and second surface properties, such as surface diffusion and segregation, surface relaxation and surface corrugations.

**4.3.1 Size-dependent lattice constants.** Experimental evidence for lattice expansion of rutile nanocrystals is given in the study of Li *et al.*<sup>245</sup> By X-ray diffraction and X-ray photoemission they evaluated peak broadening and peak shift. The lattice volume linearly increased with decreasing particle diameter. For particles with 5.2 nm diameter the lattice volume increased by 6.3%. They attributed the lattice expansion to the negative interface pressure.<sup>246</sup>

Size-dependent lattice parameter changes are frequently observed in metallic and oxidic nanoparticles. As discussed below, lattice expansion in nanoparticles has been reported for oxides, while in metals the lattice volumes shrink due to compressive surface stress.

Huang *et al.*<sup>247</sup> investigated the influence of surface tension and particle shape on the size-dependent lattice contraction of metallic nanoparticles. Their calculations are based on elasticity

theory, which uses a continuum model and has proven to be a suitable approach to treat nanoparticles larger than 1 nm. In contrary, molecular dynamics essentially depends on the selection of the molecular potentials. In this study the bulk modulus was assumed to be constant throughout. The results of Huang indicate an increasing lattice contraction for metallic particles with decreasing diameter below a threshold diameter of 5 nm. They show that the effect of the surface tension on the lattice parameter can be neglected. The shape can in general account for up to 10% of the lattice contraction if the metallic nanoparticle deviates from the sphere.

A different view is taken from Huxter *et al.*<sup>248</sup> in the investigation of CdSe nanoparticles. They measured the acoustic phonon modes of CdSe nanoparticles and performed calculations based on elasticity theory. Huxter *et al.* not only included the surface stress into their calculation, but also investigated the bulk modulus as a function of the particle size. They suggest a thermodynamically governed interplay between the surface energy and compensating elastic material properties. In this study, CdSe nanoparticles larger than 4 nm showed bulk behaviour. Very small CdSe nanoparticles of 1.4 nm were found to be four times more compressible than bulk CdSe. The authors investigated how deeply the surface reconstruction propagates into the particle volume by counting the atoms which are affected by the two surface monolayers. The size dependency ceased when less than half of the particle atoms are within the two lattice spacings of the surface.

Experimental studies on oxygen deficient  $\text{CeO}_{2-x}$  particles have also shown increased lattice parameters. Tsunekawa *et al.*<sup>249</sup> performed X-ray photoelectron measurements on oxygen deficient  $\text{CeO}_{2-x}$  particles. They found an increase in oxygen deficiency, *i.e.* an increased molar fraction in reduced  $\text{Ce}^{3+}$  ions with decreasing lattice parameter. They attribute the observed lattice parameter increase to the reduced electrostatic forces of  $\text{Ce}^{3+}$  atoms at the surface.

**4.3.2 Li-diffusion and incorporation into small rutile particles.** Because diffusion lengths in small particles are shorter than in bulk crystals, lithiation of the whole particle is expected. Diffusion properties and incorporation mechanisms thus apply to the whole particle, whereas in bulk crystals, this is considered as near surface region phenomenon.<sup>166</sup>

It is generally accepted that Li predominantly diffuses along the *c* channels into the rutile lattice. The Li diffusion coefficients in rutile were experimentally determined by Johnson<sup>198</sup> to  $2.7 \times 10^{-3} \text{ cm}^2 \text{ s}^{-1}$  along *c* and  $10^{-12} \text{ cm}^2 \text{ s}^{-1}$  perpendicular to *c*. This strong anisotropy was later confirmed in the theoretical studies discussed below. The published models for the pathway of the Li ions through the rutile lattice are all based on diffusion in the *c* channels.

The diffusion coefficient is considered to depend on (i) the temperature, (ii) the current–voltage conditions and (iii) the Li concentration.

An experimental investigation of the concentration-dependent diffusion coefficient of nanosized  $\text{TiO}_2$  rutile by Bach *et al.*<sup>204</sup> via AC impedance spectroscopy evidences a lower impedance and a significantly better charge transfer and lithium transport kinetics in comparison to a micron-sized sample. The lithium diffusion

values  $D_{\text{Li}}$  decrease linearly with higher lithium content. The isotropic  $D_{\text{Li}}$  is between  $7 \times 10^{-8}$  and  $10^{-9} \text{ cm}^2 \text{ s}^{-1}$  for low lithium contents ( $\text{Li}_x\text{TiO}_2$ ,  $x \leq 0.4$ ) and  $5 \times 10^{-10} \text{ cm}^2 \text{ s}^{-1}$  at higher ones ( $0.4 < x < 0.8$ ). This result can be explained by the calculated energy barrier in the lithium diffusion process, which is 0.35 eV for nanosized material and thus significantly smaller than for micron-sized rutile with 0.85 eV.<sup>199</sup>

Koudriachova *et al.*<sup>250</sup> found from density-functional simulations the octahedral sites energetically preferred for Li incorporation. In addition they considered diffusion of Li in the (*a,b*) plane possible but energetically unfavourable as a result of their calculations. In a relaxed lattice the energy barrier between minima in the *c* direction is 0.04 eV and 0.8 eV in the (*a,b*) plane.

Gligor and Deleuw<sup>201</sup> investigated the trajectories of the Li ion by means of molecular dynamic simulations. They found that the Li ions proceed through jumps between octahedral sites. According to their results from probability density function calculations, the movements of a Li ion within the (*a,b*) plane are restricted within the occupied *c* channel. This means changing the channel by diffusion in the (*a,b*) plane is negligible from probabilistic considerations.

In electrochemical cycling, Kerisit *et al.*<sup>251</sup> propose a strong interaction of the Li ion with the parallel migrating electron. They predict the electrons to form electron polarons with the phonons of the rutile lattice. These polarons are expected to form correlated pairs with the Li ions where the polarons drag the Li ions through the rutile lattice.

The dielectric constant in rutile is highly anisotropic. According to the inelastic neutron scattering experiments of Traylor *et al.*<sup>252</sup> the static dielectric constant in the *c*-direction is 170 and thus approximately twice as large as along the *a*-direction where it is 86. Koudriachova *et al.*<sup>250</sup> combine the dielectric behaviour with the large deformation of the Li environment in the rutile lattice and conclude to a temperature dependent anisotropic screening of the electrical field of the Li ion. As a consequence they observe ordering of Li in the (*a,b*) plane for low Li concentrations.

Hence, the structural transformations occurring with increasing amount of diffusing Li are governed by an interplay of structural and electronic properties. The anisotropic diffusion properties of rutile and the preferred octahedral sites occupied by Li ions at room temperature cause the ordered incorporation of the Li in the rutile lattice.<sup>205</sup> This ordering reduces the tetrahedral symmetry and leads to the formation of the intermediate phases.

**4.3.3 Size-dependent elastic properties.** The lattice parameter increase affects the strength of the Ti–O bonds and thus the elastic properties of nanosized titania particles. Gerward and Olsen<sup>253</sup> determined the bulk modulus for rutile Standard Reference Material (from National Institute of Standards and Technology (NIST), USA) by synchrotron X-ray diffraction under high and ambient pressure. They calculated the bulk modulus of rutile volume crystals to 230 GPa at ambient pressure. Arlt *et al.*<sup>254</sup> determined the bulk modulus of anatase volume crystals by X-ray diffraction and *ab initio* calculations using a perturbed ion model to 179 GPa.

Mo and Ching<sup>255</sup> calculated the bulk modulus for bulk titania crystals by applying the self-consistent orthogonalized



LCAO method in the local-density approximation. They calculated the bulk modulus of rutile and anatase to 209.34 GPa and 272.11 GPa, respectively. According to their results, the bulk modulus of rutile for a bulk crystal is 30% lower than that of anatase. These values, however, are not in agreement with experimental data.

Chen *et al.*<sup>256</sup> investigated the size-dependent bulk modulus of free standing anatase nanoparticles by high-pressure synchrotron X-ray diffractometry. In accordance with the Hall–Petch effect for nanostructured polycrystalline materials, the bulk modulus of the particles increased from the bulk value 179 GPa to 239 and 245 GPa (from two independent measurements) for 15 nm particles. With decreasing particle size the bulk modulus decreased to 199 GPa for 6.5 nm particles and 185 GPa for 4.0 nm particles. For particles with 3.6 nm diameter they calculated the bulk modulus to 143 GPa, what is below the bulk value. This softening corresponds to an inverse Hall–Petch effect for free standing particles below a certain threshold diameter. In particular they consider open, less rigid surface layers with a smaller bulk and shear modulus than found in the interior of the particle to be responsible for the softening effect. The authors estimated the surface layer to *ca.* 0.2 nm and the bulk modulus of the surface to 139 GPa in order to calculate the influence on surface softening on the whole particle. They subtracted the surface from the particle and calculated the bulk modulus of a core particle without soft shell. From the published plot of the experimental and calculated curve, the maximum difference, *i.e.* the maximum softening influence of the surface can be extracted to be *ca.* 20 GPa, obtained for particles of *ca.* 3–6 nm.

Mayo *et al.*<sup>257</sup> conducted a nanoindenter study on compacted and sintered rutile nanoparticles. Sintering at 400, 700 and 900 °C was used in order to set the particle size to 14.3, 32.4, and 243.3 nm. The grain size of as-compacted particles was 12.2 nm. The estimated densities were 90–96% after sintering at 900 °C and 75% in the as-compacted sample. The variation between two measurements on the same sample varied up to 30%, which was attributed to sample inhomogeneities. However, the measured hardness of the as-compacted particles reaches a minimum value of *ca.* 10% of the single crystal value on the (001) plane for the as-compacted sample and *ca.* 40% for the sample sintered at 400 °C. The rutile nanoparticles were softer than the bulk crystal and thus easier to deform plastically. The authors obtained the same trend for the Young's modulus. The Young's modulus for the as-compacted sample is about 12 GPa, *i.e.* 2.4% of the single crystal value of 489 GPa. The samples were more compliant than the bulk crystal and thus easier to deform elastically.

**4.3.4 Surface relaxation.** Surface properties are generally size-independent properties. With decreasing particle size and increasing total surface area however, the role of the surface properties in the particle increases. Moreover, below a certain threshold particle diameter the surface properties interact with the full particle volume and govern the material properties of the entire particle.

In an *ab initio* study Hallil *et al.*<sup>258</sup> have calculated the relaxation of (110), (100) and (001) pure rutile surfaces, taking into account surface formation energies and charge transfer.

The charge transfer gives the deviation of the charge of a surface atom compared to the bulk value. In the case of the (110) surface, positive relaxation, *i.e.* towards the outside resulted for all atoms, except of one fivefold coordinated Ti. Charge transfer calculations showed similar charges for the fivefold coordinated Ti with a lost bond and a sixfold coordinated Ti. This finding is in agreement with earlier examples listed in the review article of Diebold,<sup>259</sup> in which it was also shown that at zero temperature only fivefold coordinated atoms are drawn inwards, while sixfold coordinated Ti are relaxing outwards.

Stashans *et al.*<sup>166</sup> conducted quantum-chemical Hartree–Fock calculations on Li incorporation into the rutile (110) surface. After the five-fold coordinated Ti obtained an electron from the diffusing Li in an octahedral site, it relaxes outwards, while the oxygen ions are moving towards the Li.

The impact of externally applied strain on rutile surface reconstructions was simulated in first-principle calculations by Shu *et al.*<sup>260</sup> They found that a relaxed rutile (110) surface with ideal stoichiometry is softer than the bulk volume.

**4.3.5 Elastic strain relaxation *via* surface corrugations.** The incorporation of Li into the crystal lattice causes large mechanical stresses to which the lattice responds by straining the unit cell. The system can relax the strain either elastically *via* the surface or plastically *via* dislocation formation.<sup>261</sup> Strain relaxation *via* the surface is in particular possible in the presence of surface corrugations, *i.e.* alternating nanometre-sized hillocks<sup>262</sup> and troughs.<sup>263</sup> Enhanced elastic strain relaxation *via* corrugated surfaces implicitly causes a strain gradient towards the less efficient strain relaxing volume.<sup>264</sup> At the surface near area of a hillock facet the crystal lattice can expand outwards in case the lattice is compressively strained, which can lead to significant segregation effects in solid solution systems.<sup>265</sup> Albrecht *et al.* have shown in a TEM and AFM study on the growth of heteroepitaxial layers that elastic strain relaxation (formation of hillocks, lattice deformations) and plastic strain relaxation (dislocation formation) are related to different stress regimes.<sup>266</sup> In the presence of hillocks, plastic strain relaxation occurs at higher strains than elastic strain relaxation.

The elastic strain relaxation of the rutile lattice as a response to Li incorporation was calculated by Koudriachova *et al.*<sup>250</sup> In a total energy calculation ionic positions, size and shape of the computational unit were relaxed until the total energy was minimized. According to these results the lattice parameters in the (*a*,*b*) planes were increased and slightly decreased along *c*. However, this calculation does not take into account effects of the crystallite size and shape.

**4.3.6 Enhanced diffusion and solubility in the surface near area.** Tersoff<sup>267</sup> presented model calculations that impurities show a strong elastic interaction with the surface of the host lattice. The lattice sites at the surface are no longer equivalent to the sites in the volume as a consequence of the broken bonds at the surface. He could show for solid solution systems that the solubility of C down to the fourth monolayer of a Si (001) surface can be 10<sup>4</sup> times higher than in the bulk. These enhanced concentrations of impurities do not segregate into the volume but are stored in the surface near area.



Tersoff attributes the increased solubility to two factors. Firstly, mechanical stress resulting from the incorporated impurity can be relieved *via* the surface. Secondly, the impurity energy on certain sites is significantly lowered by interaction between the impurities with the surface stress caused by the atomic surface reconstructions. Tersoff calculated an energy reduction by approximately  $-0.7$  eV for a C atom at the second and third subsurface layer of Si (001).

For rutile, Wagemaker *et al.*<sup>268</sup> investigated in a quasi-*in situ* XANES and XPS study the Li incorporation in the subsurface and surface layers. By probing the surface and subsurface layer of electrochemically lithiated rutile electrodes, they could localise Li in a less than 3 nm thick surface layer. The Li was potentiostatically inserted from  $-1.5$  V to  $-2.1$  V. In this regime full incorporation must be assumed to be less than in the potential between 1 V to 3 V, what was used in the present study. However, it is sufficient to proof that Li incorporation occurs predominately close to the surface. Koudriachova<sup>269</sup> however, expected homogeneous mixing in the volume of nanosized particles.

#### 4.4 Reversible Li insertion in rutile nanorods

The structural reversibility of the Li incorporation into 5–10 nm rutile nanorods is interpreted as a result of the interaction between the above-discussed properties of the rutile nanorods as (i) enhanced Li diffusion and enhanced Li incorporation in the surface near area, (ii) elastic strain relaxation *via* the corrugated surface, (iii) enlarged lattice parameters in the particle volume and outwards directed surface relaxation and (iv) the enhanced elasticity and thus compliance towards the stress imposed on the lattice by Li incorporation.

From general physical considerations, enhanced Li diffusion in the surface near area and enhanced Li incorporation into the surface layers can be expected. Outwards relaxation of the sixfold coordinated Ti atoms and of the lithiated fivefold coordinated Ti atoms support the Li storage in the (110) surface.

The surface corrugations offer additional openings to the c-channels, thus facilitating the Li indiffusion. Moreover, mechanical strain due to the Li incorporation can be relaxed elastically by lattice expansion at the facets of the hillocks.

When Li is incorporated into a rutile lattice with larger than bulk d-spacings, the resulting lattice distortions and thus the mechanical stress is lower than in the bulk. This effect is increased by the enhanced compliance of very small particles due to size dependent bulk modulus for very small particles.

### 5. $\text{TiO}_2$ as catalyst support

$\text{TiO}_2$  and related oxide materials are applied or of potential interest for numerous applications in heterogeneous catalysis, ranging from photocatalysis<sup>270</sup> *via* synthesis of fine chemicals to various hydrogenation and selective oxidation reactions, where the latter reactions involve either mixed oxide catalysts or  $\text{TiO}_2$  supported metal catalysts. As a reducible oxide, it interacts strongly with metal nanoparticles ('strong metal-support interactions'), leading to the SMSI effect.<sup>271</sup>

Due to space limitations, we will demonstrate the advantages, but also possible drawbacks of mesoporous  $\text{TiO}_2$  and related materials in catalysis using a catalyst system and a class of

reaction as example, where sufficient data are available for a systematic discussion of the specific effects brought about by the use of these mesoporous materials. In the present paper, we will focus on mesoporous  $\text{TiO}_2$  supported Au catalysts and their performance in two model reactions, the oxidation of CO and the preferential oxidation of CO in a  $\text{H}_2$ -rich atmosphere, as example. These catalysts, consisting of Au nanoparticles of a few nanometres in diameter, deposited on disperse metal oxides have been found to be highly active in a number of oxidation and reduction reactions, with CO oxidation being the most prominent one.<sup>6,272</sup>

Elemental Au was generally considered to be catalytically inactive, until in 1972 Bond reported that supported gold nanoparticles (NPs) are active in the hydrogenation of olefins.<sup>273</sup> But only more than a decade later, Hutchings and Joffe showed that Au NPs dispersed on carbon or silica are very efficient catalysts for acetylene hydrochlorination to vinyl chloride.<sup>274</sup> And again two years later, Au catalysts ( $\text{Au}-\alpha\text{-Fe}_2\text{O}_3$ ,  $\text{Au}-\text{NiO}$ ,  $\text{Au}-\text{Co}_3\text{O}_4$ ) prepared by co-precipitation showed an impressive CO oxidation activity already at low temperatures.<sup>275</sup> In the meantime, finely dispersed Au NPs supported on metal oxides have been demonstrated to be very active in various important oxidation and reduction reactions such as CO oxidation,<sup>275</sup> preferential CO oxidation in  $\text{H}_2$ -rich mixtures,<sup>276</sup> water gas shift reaction,<sup>277,278</sup> epoxidation of propene,<sup>279</sup> or NO reduction.<sup>280</sup>

Despite the fact that in many cases the activity and selectivity of dispersed Au NP catalysts exceeds those of the commonly used supported platinum metal catalysts based, *e.g.*, on Pt, Rh, and Pd NPs, the technical applications of supported Au catalysts are very limited so far, respirators for the protection from CO poisoning being one example ( $\text{Au}-\text{Fe}_2\text{O}_3$  or  $\text{Au}-\text{TiO}_2$ ).<sup>281</sup> Another attractive application could be the removal of CO from  $\text{H}_2$ -rich feed streams for low temperature fuel cells *via* the preferential oxidation of CO (PROX reaction).<sup>282</sup> The significant amounts of CO (1–10%), which are present in these gas mixtures if  $\text{H}_2$  is produced from fossil fuels, *e.g.*, by steam reforming and/or partial oxidation, have to be reduced to  $<10$  ppm to avoid poisoning of the fuel cell anode catalyst.<sup>283–287</sup> Au catalysts would be attractive for the final clean up (below 1% CO), *via* the PROX reaction, if for technical reasons this shall be performed at 80 to 100 °C, which may be attractive since it is close to the operating temperature of polymer electrolyte fuel cells (PEFCs).

So far, catalytic applications are mainly limited by the pronounced deactivation of oxide supported Au catalysts, including  $\text{Au}-\text{TiO}_2$  catalysts, with time on stream.<sup>288–290</sup> Accordingly, lowering the tendency for deactivation is a prime objective in today's Au catalysis research. This is also a major, if not dominant motivation for exploring the potential of high surface area oxide supports in Au catalysis.

In the following, we will elucidate the potential of high surface area  $\text{Au}-\text{TiO}_2$  catalysts and related oxide supported Au catalysts, focusing on the role of the supporting oxide for the catalytic performance in the CO oxidation reaction and in the PROX reaction. Before starting with the discussion of the catalytic behavior of these catalysts, we will summarize basic aspects of the Au catalyzed CO oxidation and PROX reaction, followed by a brief discussion of the different characteristic

procedures for catalyst preparation, specifically for Au loading of the oxides and subsequent catalyst activation. We will then discuss in detail the performance of these catalysts in the CO oxidation reaction, followed by a similar discussion of the PROX reaction. In the final section, we will summarize and discuss findings on the deactivation behavior of the catalysts in the two reactions.

### 5.1 Basic aspects of Au catalyzed CO oxidation

There is general agreement that the activity of Au catalysts depends sensitively on a number of factors, including in particular the size and shape of the Au NPs, but also the nature of the support (*e.g.*, its reducibility, specific surface area, density of defects and crystal phase, morphology), the chemical state of the support surface (*e.g.*, the presence of surface hydroxyl groups), and the interaction between Au NPs and supporting oxide. This is illustrated schematically in Fig. 22.

For instance, the activity decreases rapidly as the Au NPs grow beyond 5 nm.<sup>291</sup> These factors are of course also intimately interrelated; the interaction between oxide support and Au nanoparticle will, *e.g.*, strongly affect the Au particle size and shape. Accordingly, also other factors such as the method and conditions for the preparation of the supported Au NP catalysts or of the activation pre-treatment of the Au catalysts will be important, as they affect both, the Au particle size and shape as well as the chemical state of the support surface. Furthermore, it has been suggested that point defects and step edges on the oxide support are important for the stabilization of the Au NPs and therefore play an important role in determining the catalytic activity of the Au catalysts. Finally, the supporting oxide does not only act as a carrier for the Au NPs (*indirect* role), but may also play a *direct* role in the CO oxidation reaction, which was first suggested by Haruta already in 1987.<sup>6</sup> In 2001, Schubert *et al.* defined two categories of supports: (i) active supports which are more or less easily reducible (able to release oxygen upon formation of oxygen vacancies) such as TiO<sub>2</sub>, Fe<sub>2</sub>O<sub>3</sub>, or CeO<sub>2</sub> and (ii) 'inert', non-reducible supports such as Al<sub>2</sub>O<sub>3</sub> or SiO<sub>2</sub>.<sup>292</sup>

Focusing on the CO oxidation reaction, a number of different mechanistic models have been proposed to explain their high activity already at low temperatures. A possible

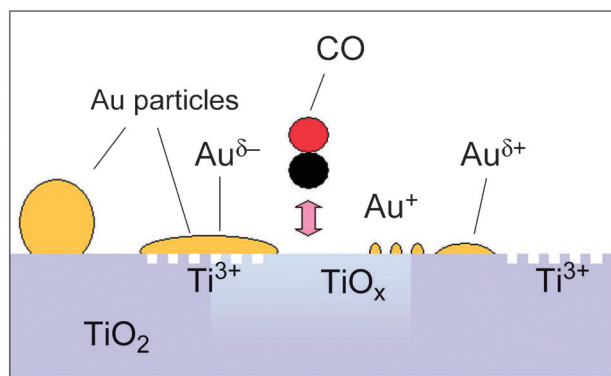


**Fig. 22** Schematic illustration of the different TiO<sub>2</sub> support phases and Au species potentially present on a Au-TiO<sub>2</sub> catalyst surface during CO oxidation reaction (reprinted with permission from Christmann *et al.*<sup>396</sup>).

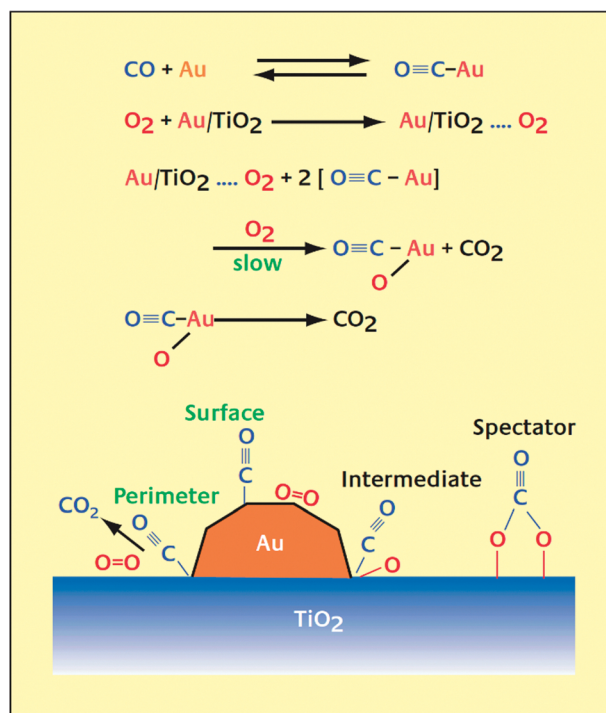


**Fig. 23** Schematic illustration of the CO oxidation mechanism, the reactant and product as well as the reaction intermediates and side products/spectator species on a Au-TiO<sub>2</sub> catalyst surface during CO oxidation reaction (reprinted with permission from Haruta<sup>385</sup>).

mechanism is illustrated in Fig. 23. The main points under discussion are (i) the active site(s) and, closely related, the nature of the active Au species (see Fig. 22), (ii) the mechanism for O<sub>2</sub> activation, and (iii) the role of the support.

Over the years, the discussion on these points was controversial. Less controversial is the adsorption site of the second reactant, CO<sub>ad</sub>. In numerous IR spectroscopic studies the authors agreed that under reaction conditions carbon monoxide is mainly or even exclusively adsorbed on Au NPs.<sup>293–295</sup> Since this is important also for the understanding of the major question discussed in this section, the potential of high surface area TiO<sub>2</sub> and related materials in Au catalysis, we will briefly summarize the main ideas and concepts:

- Most studies exploring this aspect, including the early study by Haruta *et al.*,<sup>6</sup> claim that metallic Au NPs of 2–5 nm diameter represent the active Au species, while others suggested that charged or ionic Au species,<sup>296–299</sup> either cationic<sup>297–299</sup> or negatively charged<sup>296</sup> ones, may act as highly active centers. Most likely, this depends also on the nature of the support, and for Au-TiO<sub>2</sub> there seems to be general agreement on metallic Au NPs as active species.

- The pronounced Au particle size effects were rationalized by quantum size effects,<sup>300</sup> or, alternatively, by the increasing presence (on a relative scale) of highly active undercoordinated Au atoms on small Au NPs.<sup>301,302</sup> As a third possibility, the increasing length of the perimeter of the interface between support and Au NPs with decreasing Au particle size was proposed to explain these size effects.<sup>303</sup> While the first possibility was discarded later, the latter two are still discussed and may in fact both contribute.

• The mechanism for O<sub>2</sub> activation found less attention in earlier studies. Some authors suggested that the support can supply and activate oxygen species,<sup>6,292,304</sup> others believed that oxygen dissociates at undercoordinated sites of the Au NPs,<sup>302</sup> while the majority suggested that it is adsorbed as O<sub>2</sub><sup>−</sup> species on gold atoms along the perimeter sites. Recent theoretical studies agreed that oxygen activation proceeds *via* adsorption of an O<sub>2</sub><sup>−</sup> species either at the interface perimeter or at undercoordinated Au sites and subsequently reacts with CO<sub>ad</sub>, to leave an atomic oxygen species on the surface which can react with another CO<sub>ad</sub>.<sup>305–309</sup> Recent *temporal analysis of products* (TAP) reactor studies, however, provided convincing experimental evidence that on Au–TiO<sub>2</sub> and most likely also on other reducible oxide supported catalysts oxygen activation proceeds *via* reaction of CO with surface lattice oxygen at the perimeter of the Au–TiO<sub>2</sub> interface and subsequent refilling of the resulting vacancies by reaction with O<sub>2</sub>, in a Au-assisted Mars-van Krevelen mechanism.<sup>310</sup>

• Accordingly, ionic Au species,<sup>297,298</sup> undercoordinated Au atoms (edges and corners at the Au NPs),<sup>301,302,311</sup> bilayer Au particles,<sup>312</sup> or the perimeter sites at the interface between oxide support and Au NPs were proposed as active sites.<sup>6,303,310,313–315</sup> For Au–TiO<sub>2</sub> the latter opinion is more or less generally accepted nowadays.

• Using preformed Au NPs of similar size, which allows us to exclude particle size effects, it could be clearly demonstrated that the nature of the support plays a decisive role for the CO oxidation activity of different oxide supported Au catalysts.<sup>316,317</sup>

• Another unresolved point is the role of water in the reaction. It is known that small amounts of water vapor in the reactant gas can greatly influence the reaction.<sup>318</sup> This was tentatively explained by an improved activation of oxygen by (small amounts) of adsorbed water/hydroxyl species.<sup>295</sup> Furthermore, water was proposed to enhance decomposition of surface carbonate species.<sup>288,319</sup> On the other hand, Gao *et al.* concluded later that water promotes the formation of carbonate species.<sup>320</sup>

The physical origin for the pronounced deactivation of oxide supported Au catalysts in oxidation reaction was also discussed controversially. Most commonly, this is attributed to growth of the active nanoparticles. In another mechanism, the catalysts surface and the active sites for reaction are increasingly covered ('poisoned') by stable adsorbates formed as side products during the reaction. Since agglomeration of Au NPs can be essentially excluded for reaction under the typical low temperature conditions (80–100 °C),<sup>288,321,322</sup> the latter explanations seem to be more realistic and have been favored in numerous studies.<sup>288,289,322,323</sup> For CO oxidation, possible side products are surface formates, surface (bi-)carbonates and surface carboxylates, for the PROX reaction also adsorbed water has to be considered. In that case the tendency for deactivation of a given catalyst could be reduced by increasing the surface area, by lowering the rate for stable adsorbate formation, or by enhancing the rate for continuous adsorbate removal, *e.g.*, by thermally induced decomposition. Assuming that the reaction takes place either on the Au NP or at the perimeter of the interface, a higher surface area would improve the stability by enhancing the uptake capacity for surface species on the support surface, leaving more available sites on the active

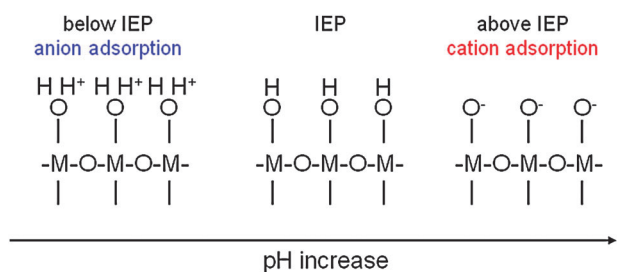
surface areas. Considering Au NP growth, strengthening the interaction between support and Au NP or increasing the surface area would be possible routes for improving the long-term stability of the catalyst.<sup>324,325</sup> In this case, the larger surface area would increase the separation between the Au NPs, and thus lower the potential for agglomeration. Furthermore, Au NPs located in the pores of mesoporous support materials might be further stabilized by multiple contacts between support and Au NPs. In conclusion, high surface area, mesoporous oxide supports have a clear potential to improve the long-term stability for both deactivation mechanisms. Another way to possibly increase the stability on-stream involves a modification of the surface chemistry of the oxide supports to influence the rate of formation/decomposition/desorption of deactivating surface species. Considering surface carbonates or formates, this could be achieved by increasing the acidity of the support surface. This can be reached, *e.g.*, by doping the support with another element,<sup>5</sup> or by more complex approaches for surface modification, *e.g.*, by deposition of a thin TiO<sub>2</sub> cover film of one or more layers thickness on a SiO<sub>2</sub> support material.<sup>326,327</sup>

## 5.2 Au catalyst preparation

Several preparation techniques have been developed and applied for the preparation of oxide supported Au catalysts,<sup>328–333</sup> and Au catalyst preparation is well documented also in a recent review by Corma and Garcia.<sup>334</sup> Focusing on Au–TiO<sub>2</sub> catalysts, however, deposition–precipitation (DP) procedures still remain the most simple and most used method; the quality of the resulting catalysts, however, in particular the size of the Au NPs, depends sensitively on details of the Au loading procedure and on the conditions used.<sup>275,335,336</sup> In contrast, impregnation with HAuCl<sub>4</sub><sup>275,337</sup> or co-precipitation lead to low activity Au catalysts. Only upon addition of magnesium citrate into the precipitation solution it was possible to obtain smaller Au NPs. The role of the citrate anions in the co-precipitation process, however, is not clear.<sup>328</sup>

In the DP procedures, the gold NPs are mostly formed from single Au atom gold precursors (*i.e.*, HAuCl<sub>4</sub>·3H<sub>2</sub>O) in an aqueous solution and in the presence of a suspension of the support. Raising the pH causes precipitation of Au(OH)<sub>3</sub>. The surface properties of the support play the key role and strongly affect the formation and final dispersion of Au NPs.<sup>338,339</sup> To stabilize small Au NPs, the support must provide a suitable surface which allows for sufficiently strong interactions between Au and the support, or a high surface area, which keeps the small Au NPs sufficiently far apart that agglomeration is hindered, especially during the calcination step. The optimal experimental conditions reported in the literature for the preparation of highly active Au catalysts by the DP method depend on (i) the type of the Au precursor, (ii) the pH range and the adjusting agent used, (iii) the isoelectronic point (IEP) of the support, and (iv) the pre-treatment (activation) of the as-prepared catalyst, prior to the catalytic reaction. Another condition, which needs to be fulfilled in order to obtain active, small Au NPs, is the absence of impurities, in particular chlorine, sodium/potassium and sulphur. For example, already trace amounts of residual chlorine





**Scheme 1** Relation between supporting  $\text{MO}_x$ , pH and isoelectric point (IEP).

(<0.015 wt%) have a negative impact on the overall CO oxidation activity. They affect (i) the mobility of Au on the support, by the formation of Au–Cl–Au bridges, which leads to agglomeration and growth of the Au NPs upon heat treatment, and (ii) poison active sites.<sup>297,323</sup> Employing Haruta's original DP method, which uses  $\text{HAuCl}_4 \cdot 3\text{H}_2\text{O}$  as a gold precursor and  $\text{Na}_2\text{CO}_3$  or  $\text{NaOH}$  to maintain the pH, requires extensive washing to reduce impurity levels below tolerance limits. In addition to the Au precursor, also the pH plays an important role, as the support has the role of a nucleation centre (positively charged) for the negatively charged Au complex (dependent on pH,  $\text{Au}(\text{OH})_x\text{Cl}_{4-x}^-$  is attached to the positively charged protonated OH groups of the support, if the pH is below the IEP of the support). Hydrolysis of  $\text{AuCl}_4^-$  releases also  $\text{Cl}^-$  which is also adsorbed on the support surface. Therefore, the degree of chloride poisoning depends on the IEP (Scheme 1) of the support.<sup>340</sup>

Chang *et al.* modified the DP method by the addition of magnesium citrate into the preparation solution in order to overcome the problem of chloride poisoning, by replacing it by the citrate anions, which produced thus highly active catalysts.<sup>341</sup> Another possible modification of the DP procedure involves the use of urea as a pH adjusting agent, which was developed by Zanella *et al.*<sup>342</sup> The authors explained the benefits of urea as adjusting agent by a number of effects, including (i) surface complex formation, (ii) a decrease of the positive charge after the IEP of  $\text{TiO}_2$  is reached, leading to neutral surface hydroxyl groups which provide more sites for the formation of Au complexes, and (iii) the fact that all gold present in the solution precipitates on the  $\text{TiO}_2$  surface probably *via* the formation of gold colloids.

Denkwitz *et al.* prepared Au supported catalyst based on various mesoporous supports (mesoporous  $\text{TiO}_2$  with rutile and anatase morphology),<sup>343</sup> using a slightly modified DP method.<sup>344</sup> They found that the type of  $\text{TiO}_2$  polymorph strongly affects the amount of Au deposited on the support and the mean diameter of the resulting Au NPs. The mean Au NPs size was found to decrease in the order rutile > mixture of rutile and anatase > anatase.<sup>343</sup> The authors tentatively related the larger Au particle size on rutile supported catalysts to a better stabilization of the Au NPs on the anatase support. Schwartz *et al.* also reported distinct differences in the amount of Au loaded upon DP of Au on three  $\text{TiO}_2$  polymorphs.<sup>345</sup> Using the same DP procedure, they obtained 13.7, 12.6, and 3.3 wt% Au on mesoporous rutile, anatase, and brookite, respectively. (In all cases a Au loading of 13 wt% would have been obtained if all Au would have adsorbed). Yan *et al.* also

prepared Au catalysts by a DP procedure on mesoporous anatase, rutile and brookite, getting 13, 14, and 3.3 wt% of Au on anatase, rutile and brookite, respectively (theoretical value: 13 wt% of Au).<sup>346</sup> After oxidative pre-treatment (8%  $\text{O}_2$  in He, 573 K, 10 min), Au/rutile showed the highest deactivation, while the stability of Au/brookite seemed to be least affected by thermal treatment. Au/rutile was found to have the lowest CO oxidation activity, which was explained by large Au NPs, although proper TEM analysis is missing.<sup>346</sup>

The physical origin of the differences in the Au deposition behavior on the different polymorphs is not yet clear, most likely it is related to differences in the surface chemistry, *e.g.*, in the degree of surface hydroxylation, and in the (bulk) defect density.<sup>347,348</sup> It is important to note that these differences in the Au deposition behavior do not affect the stability of the Au NPs under reaction conditions.<sup>343,349</sup>

Going to more complex support materials with modified properties for the CO oxidation reaction, these often involve different types of surface sites and/or crystalline phases with different acid–base properties. It is likely than in many cases the Au NPs will be formed preferentially on one site/phase and grow subsequently, depending on the synthesis conditions used and the different acid–base properties of such surface sites/phases. Geserick *et al.* prepared highly active mesoporous mixed oxide  $\text{Au-Si}_x\text{Ti}_{1-x}\text{O}_2$  catalysts with different of Si–Ti ratios and morphologies (rutile, anatase).<sup>5</sup> Similarly to the observation for mesoporous rutile and anatase  $\text{TiO}_2$  supports, the mean Au particle diameter was in the range of 2.0–2.7 nm for all anatase mixed oxide supported Au catalysts, while for the rutile polymorph mixed oxide supported catalyst the mean Au particle size was larger, around 3.2 nm for similar deposition conditions. (For pure rutile  $\text{TiO}_2$  supported Au catalysts it was  $6.1 \pm 1.5$  nm.) Similarly, the highest Au loading was obtained on the rutile mixed oxide sample. Another important factor was the Si–Ti ratio. For the sample with the highest Si concentration, the lowest amount of Au was deposited. This can be rationalized by the mechanism of the DP method. Since the IEP of  $\text{SiO}_2$  is  $\sim 2$  and we used a pH 5–6 for Au loading, with increasing amount of  $\text{SiO}_2$  in the mixed oxide support, the Au concentration will decrease due to the fact that  $\text{Au}(\text{OH})_x\text{Cl}_{4-x}^-$  cannot be attached to the negatively charged surface of the support, if the pH is above the IEP of the support.<sup>5</sup> A similar DP procedure was used recently to prepare a Au catalyst supported on a SBA-15 support surface modified by 1–4  $\text{TiO}_2$  monolayers.<sup>350</sup> In that case, the Au loading increased with increasing number of  $\text{TiO}_2$  cover layers, from about 2.2 to 3.2 wt%, with the mean size of the Au NPs between 3.5 and 4.9 nm.

To improve the hindered deposition of Au on silica surfaces, which was attributed to a weak interaction between the Au precursor ( $\text{AuHCl}_4 \cdot 3\text{H}_2\text{O}$ ) and the silica surface (low IEP of  $\sim 2$ ), a modified DP process using a cationic precursor  $[\text{Au}(\text{en})_2]^{3+}$  was developed.<sup>351,352</sup> Zhu *et al.* reported on a highly active mesoporous Au/SBA-15 catalysts with Au NPs of 4.9 nm (pre-treatment: calcination in 8%  $\text{O}_2$ –He at 400 °C).<sup>351</sup> This is in a good agreement with recent findings of Sundararajan *et al.*, who determined a Au NPs size of 6.1 nm on pure SBA-15 material (DP method,  $[\text{Au}(\text{en})_2]^{3+}$  as an Au precursor, pH 9) after annealing in a stream of 10%  $\text{O}_2$ – $\text{N}_2$



at 400 °C (30 min).<sup>353</sup> Another possibility for controlled Au deposition involves the use of chemical vapor deposition of MeAu(acac), which yielded a highly active Au–SiO<sub>2</sub> catalyst Au (NP Ø 6.6 nm), more active than the standard Au/P25 catalyst under similar reaction conditions.<sup>291</sup>

Recently, Tai *et al.* prepared highly stable mesoporous Au catalysts supported on titania coated silica by deposition of preformed, thiol-capped Au NPs.<sup>332</sup> The CO oxidation activity was affected by the presence of sulphur and increased by a factor of 3–5 after oxidative removal of sulphates at 400 °C or 600 °C, resulting in TOF values of ~0.015 for reaction at –63 °C. Long *et al.* prepared Au–TiO<sub>2</sub> catalysts by deposition of thiol monolayer-protected Au clusters (MPCs).<sup>354</sup> The thiol MPCs were prepared using dendrimer templates, the thiol stabilizer was removed reductively, by heating in a H<sub>2</sub>–N<sub>2</sub> (1 : 1) mixture at 290 °C for 16 h. Based on TEM analysis, the mean diameter of the Au HPs increased from 2.8 to 3.4 nm during the reductive treatment. Similarly, Gaur *et al.* prepared microporous Au–TiO<sub>2</sub> catalysts by impregnation with thiol capped Au<sub>38</sub>(SC<sub>12</sub>H<sub>25</sub>)<sub>24</sub> particles.<sup>333</sup> Upon subsequent reductive pre-treatment in 5% H<sub>2</sub>–He (60 min, 400 °C), the Au NPs grew from 1.7 to 3.9 nm. Both groups, Long *et al.* and Gaur *et al.* found that without a pre-treatment the catalysts are essentially inactive. After the reductive pre-treatment, the catalysts showed a moderate activity, which is, however, lower than that of conventionally prepared catalysts. The low activity of the non-pre-treated catalyst was attributed to the surface blocking of the Au NPs due to the adsorbed thiol species.

Akolekar and Bhargava prepared Au catalysts consisting of Au NPs confined in microporous and mesoporous materials by direct synthesis (Au loading 0.166–2.2 mol%); after a subsequent treatment at 1275 K in He, the size of the Au NPs was 8–11 nm for MCM-41 and 6 nm for ZSM-5, respectively.<sup>331</sup>

Another deposition method, denoted as the Au colloidal deposition method, was introduced by Comotti *et al.*<sup>317,355</sup> In this case, the Au NPs are prepared first by addition of a stabilizer, *e.g.*, polyvinyl alcohol (PVA) or glucose to an aqueous solution of HAuCl<sub>4</sub> at room temperature. Afterwards, an aqueous solution of NaBH<sub>4</sub> is added to initiate gold reduction (formation of metallic Au NPs). Subsequently, the support material is added under stirring to this Au colloidal solution, until all Au particles are deposited on the support. The size of the Au NPs on various supports is around 3 nm (controlled by the stabilizing agent), the Au loading was 1 wt%.<sup>316,317</sup> The size of the Au NPs is largely preserved upon deposition on the support and subsequent pre-treatment (10% O<sub>2</sub> in N<sub>2</sub>, 250 °C). The Au loading is determined by the deposition time and the amount of support material added. Also this method, however, is limited by the “ability” of the support to adsorb all Au NPs, which is particularly critical, *e.g.*, for SiO<sub>2</sub>. The colloidal deposition method allows preparing Au catalysts with different support materials, but (almost) identical Au particle size and Au loading, which is attractive for comparative studies.<sup>316,317</sup>

In summary, there is a large variety of different methods and procedures for preparing highly active Au catalysts based on different support materials, and only a limited selection of them could be discussed in this review. The Au colloidal deposition method seems to be a good candidate for the preparation of catalysts with well-defined Au particle sizes,

independent of the support material and Au loading, which is particularly attractive for comparative studies. On the other hand, the DP method seems to be the best compromise in order to prepare highly active Au catalysts, although it does not always lead to comparable results.

### 5.3 CO oxidation reaction

In the following, we will review the catalytic performance of different high surface area TiO<sub>2</sub> supported and related Au catalyst in the CO oxidation reaction. The main information is briefly summarized in a table at the end of each section. Since in many cases direct kinetic information in terms of (Au mass normalized) reaction rates or turn-over frequencies is missing, we use as much as possible the comparison with the activity of standard, nonporous P25 (Degussa) type TiO<sub>2</sub> (BET surface area 56 m<sup>2</sup> g<sup>–1</sup>) supported Au–TiO<sub>2</sub> catalysts (Au/P25) as reference for the activity of the respective catalysts.

**5.3.1 Mesoporous Au–TiO<sub>2</sub> catalysts.** In the section we focus on the catalytic performance of high surface area TiO<sub>2</sub> supported Au catalysts, with special emphasis on the influence of crystal morphology (for details see Table 2).

A significantly higher catalytic activity of a mesoporous Au–TiO<sub>2</sub> catalyst compared to a Au/P25 catalyst was reported by Wang *et al.*<sup>325</sup> Mesoporous crystalline TiO<sub>2</sub> rutile (5% anatase, BET surface area 245–300 m<sup>2</sup> g<sup>–1</sup>) was prepared by oxidative hydrolysis and condensation in the presence of anionic surfactants. Au was loaded *via* a DP method. A mesoporous Au–TiO<sub>2</sub> catalyst (MCT-Ti) showed a high activity with 50% conversion at –44 °C (Au loading 7 wt%) and at 13 °C for CO oxidation on freshly prepared samples and after pre-treatment at 500 °C in 8% O<sub>2</sub>–He, respectively. For comparison, for reaction at a Au/P25 catalyst (5.6 wt% Au loading) under similar reaction conditions, the respective values are –39 and 126 °C. The authors explained the difference in activities by a higher stabilization of the Au NPs in the mesoporous matrix compared to nonporous P25. Based on TEM images, the Au NPs tended to agglomerate on P25, yielding particles/agglomerates of 5–30 nm in size, while they remained intact and separated in the mesoporous MCT-Ti support. It should be mentioned that the agglomeration may be a consequence of the high pre-treatment temperature, which seems to affect the Au/P25 catalyst much more than the mesoporous Au–TiO<sub>2</sub> catalyst. Comparable or somewhat higher activities for mesoporous Au–TiO<sub>2</sub> than for Au/P25 were also observed in our laboratory.<sup>343,349</sup> In this case, Au catalysts based on mesoporous anatase and rutile nanoparticles were synthesized *via* a water-based sol–gel process with titanium glycolates.<sup>356</sup>

Yan *et al.* studied the influence of the crystallographic structure on the activity and stability of mesoporous Au–TiO<sub>2</sub> catalysts.<sup>346</sup> Anatase and rutile were prepared by sonication, brookite by hydrothermal synthesis. All three samples showed inter-particle mesoporosity with specific surface areas of 225, 77 and 106 m<sup>2</sup> g<sup>–1</sup> for anatase, rutile and brookite, respectively. Au catalysts were prepared by the DP method. Comparing the activity without any pre-treatment, all three catalysts exhibited a rather high activity with 50% of the CO converted at  $T_{50}$  = –38, –31, –19 °C for anatase, rutile and

**Table 2** Mesoporous TiO<sub>2</sub> supported Au catalysts

TiO <sub>2</sub> preparation			Au preparation/characteristics			Catalytic reaction conditions			Catalytic activity/stability						
			Au (wt%)	Au NP Ø (nm)	Au NP Ø after reaction (nm)	Atmosphere/ T °C	PT	Deactivation (%)	T <sub>50</sub> (fresh) (°C)	T <sub>50</sub> (PT1) (°C)	T <sub>50</sub> (PT2) (°C)	T <sub>50</sub> (PT3) (°C)	RR	Ref.	
Part 1															
Catalyst	Synthesis	SSA (m <sup>2</sup> /g)	Method	Au	Au NP Ø (nm)	Au NP Ø after reaction (nm)	All below: 1% CO/air/RR at –30 °C (after PT2)	All below: 400 °C (PT1) 500 °C (PT2), 8% O <sub>2</sub> /He, 2.5 h	10%/25 h at 24 °C (PT1)	–44	–49	13	n.m.	1630	All below: [325]
	Oxidative hydrolysis/condensation/anionic surfactants	245–300	DP	7	n.m.	n.m.									
Au/MCT-Ti-10 R(5%)·A	Commercial	50	DP	5.6	n.m.	n.m.			–39	n.m.	126	n.m.	0.06		
Au/P25															
Au/A	Sonication	225	DP	13	Raft like 0.5–2.0 + few 20–50	5–20 (faceted)	All below: 1% CO/air/RR at –38 °C	All below: 12% H <sub>2</sub> /Ar 150 °C	n.m.	–38	4(–38)	0.75(–10)	7	2.8	All below: [326]
Au/R	Sonication	77	DP	14	n.m.	5		(PT1), 8% O <sub>2</sub> /Ar	n.m.	–31	1.8(–35)	0.0016(54)	48	0.0003	
Au/B	HT	106	DP	3.3	0.5–2	2–3 + 1–10 + larger		300 °C (PT2); 30 min	n.m.	–19	16(–38)	15(–35)	–10	30	
Au/P25	Commercial	47	DP	5.7	n.m.	n.m.			n.m.	–48	7(–25)	0.07(64)	21	2.8	
Au/P25	Commercial	47	CD	1	3.0 ± 1.3	3.0 ± 1.1	All below:	All below:	All: Primarily growth of Au NPs + other reasons	–12	–18	10	38	n.m.	All below: [357]
Au/AK350-A	Commercial	327	CD	1	2.9 ± 2.0	3.1 ± 1.3	1% CO/air, –100–300 °C	Calcined in N <sub>2</sub> at 350 °C (PT1), 450 (PT2), 550 °C (PT3)		40	40	70	100		
Au/SP06/16-R	Commercial	10	CD	1	3.0 ± 1.1	3.1 ± 1.1									
Au/TiO <sub>2</sub>	Sol-gel, template: P123	160	DP	9	3.5 (5% H <sub>2</sub> /He, 150 °C)	n.m.	1% CO/air	n.m.	n.m.	–10	–10	40	n.m.	n.m.	[324]
Au/P25 (A/R)	Commercial	58	DP	3.1	2.9 ± 0.8	n.m.	All below:	All below:	72	n.m.	n.m.	n.m.	n.m.	34.3/9.4	All below: [349]
Au/A/B56	All: Sol-gel, template: BRU56, SDS	106	DP	3.0	4.1 ± 0.8	n.m.	1% CO, 1% O <sub>2</sub> , N <sub>2</sub> , 80 °C	400 °C, 10% O <sub>2</sub> /N <sub>2</sub> , 30 min, 80 °C	67	n.m.	n.m.	n.m.	n.m.	84.1/27.9	
Au/A/SDS		175	DP	2.6	3.7 ± 0.9	n.m.			70	n.m.	n.m.	n.m.	n.m.	37.2/12.4	
Au/A-R/sds		240	DP	4.2	6.1 ± 1.3	n.m.			67	n.m.	n.m.	n.m.	n.m.	33.9/6.0	
Au/R		160	DP	4.8	6.1 ± 1.5	n.m.			74	n.m.	n.m.	n.m.	n.m.	34.8/9.2	
Au/A	Commercial	10	DP	0.08	n.m.	n.m.	All below:	All below:	All below:	n.m.	50	n.m.	n.m.	1.3	All below: [358, 359]
Au/A	Commercial	37	DP	0.47	n.m.	n.m.	0.5% CO/air, –80–100 °C, specific activity at –30 °C	Run in rx gas mixture until stable	at 20 °C	n.m.	–15	n.m.	n.m.	2.5	
Au/A	Commercial	45	DP	0.5	n.m.	n.m.				n.m.	–17	n.m.	n.m.	1.6	
Au/A	Commercial	90	DP	0.67	n.m.	n.m.				n.m.	–10	n.m.	n.m.	0.5	
Au/A	Commercial	240	DP	1.0	n.m.	n.m.				n.m.	0	n.m.	n.m.	0.3	
Au/A	Commercial	305	DP	1.0	n.m.	n.m.				n.m.	15	n.m.	n.m.	0.1	
Au/R	Commercial	100	DP	0.8	n.m.	n.m.				n.m.	–12	n.m.	n.m.	1.0	

Table 2 (continued)

TiO <sub>2</sub> preparation			Au preparation/characteristics		Catalytic reaction conditions			Catalytic activity/stability			Ref.				
Catalyst	Synthesis	SSA (m <sup>2</sup> /g)	Method	Au (wt%)	Au NP Ø (nm)	Au NP Ø after reaction (nm)	Atmosphere/ T °C	PT	Deactivation (%)	T <sub>50</sub> (fresh) (°C)		T <sub>50</sub> (PT1) (°C)	T <sub>50</sub> (PT2) (°C)	T <sub>50</sub> (PT3) (°C)	RR
Part 2															
Au/A-whisker-T300	HT	143	DP	1	8.5–13.5 (300 °C, air, 2 h)	n.m.	All below: 1% CO, 1.98% O <sub>2</sub> , He, 20–160 °C	All below: n.m.	All below: at 50 °C	50	n.m.	n.m.	n.m.	n.m.	All below: [360]
Au/A-whisker-T600	HT	59	DP	1	6.5–11.5 (300 °C, air, 2 h)	n.m.			30	30	n.m.	n.m.	n.m.	n.m.	n.m.
Au/P25	Commercial	55	DP	1	n.m.	n.m.			40	40	n.m.	n.m.	n.m.	n.m.	n.m.
Au/B-A (45%–55%)	TiCl <sub>3</sub> + urea	197	DP-urea, micelle SAu <sub>6</sub> , micelle SAu <sub>15</sub>	2.1, 2.3, 2.2 n.m.	n.m., 4.7 ± 0.7, 10.2 ± 9.4, n.m.	5 ± 1.5, 10.2 ± 9.4, n.m.	All below: 0.5% CO, 9.5% O <sub>2</sub> , 52% He, 38% Ar	All below: 400 °C, air, 1 h	n.m.	53, –, –, 52, –, 53, –, –	5, –, –, 28, –, 28, –, –	10, 79, 87	n.m.	n.m.	All below: [361]
Au/B	TiCl <sub>4</sub> + HCl	114	DP-urea, micelle SAu <sub>6</sub> , micelle SAu <sub>15</sub>	1.9, 2.1, 2.2	n.m., 6.4 ± 1.4, 15.2 ± 5.5	2.9 ± 0.9, 5.9 ± 2.0, 17 ± 6.4			n.m.	52, –, 53, –, –	28, –, 28, –, –	82, 73, 132	n.m.	n.m.	n.m.
Au/P25 (85%A-15%R)	Commercial	55	DP-urea, micelle SAu <sub>6</sub> , micelle SAu <sub>15</sub>	1.8, 2.2, 2.2	n.m., 6.4 ± 1.4, 15.1 ± 5.5	3.1 ± 0.8, 9.5 ± 6.3, 15.0 ± 5.8			n.m.	53, –, –	28, –, –	–1, 51, 22	n.m.	n.m.	n.m.
Au/R	HT	n.m.	DP	4.5	2–3	n.m.	1% O <sub>2</sub> , 1% CO, N <sub>2</sub> , 25–300 °C	5% H <sub>2</sub> /He at 300 °C (PT1), 400 °C (PT2), 500 °C (PT3), 2 h	Due to the carbonate species reactivation (activity as initial)	n.m.	n.m.	5	10	n.m.	All below: [362]
Au-Ir/R	HT	n.m.	DP	2 Ir, 4 Au	Ir ~ 1, Au 2–3	n.m.				n.m.	n.m.	5	below T <sub>room</sub>	n.m.	

A, anatase; R, rutile; B, brookite; HT, hydrothermal; SSA, specific surface area; IE, ionic exchange; DP, deposition–precipitation method; CD, colloidal deposition method; n.m., not mentioned; PT, pre-treatment. RR- reaction rate (mol<sub>co</sub> g<sub>Au</sub><sup>–1</sup> s<sup>–1</sup> × 10<sup>4</sup>) either initial or initial/final after 1000 min on stream.

A, anatase; R, rutile; B, brookite; HT, hydrothermal; SSA, specific surface area; IE, ionic exchange; DP, deposition–precipitation method; CD, colloidal deposition method; n.m., not mentioned; PT, pre-treatment. RR- reaction rate (mol<sub>CO</sub> g<sub>Au</sub><sup>–1</sup> × 10<sup>4</sup>) either initial or initial/final after 1000 min on stream.



brookite (Au loadings 13, 14 and 3.3 wt%), respectively, compared to Au/P25 (5.7 wt%) with  $T_{50} = \sim -48$  °C under similar reaction conditions. After several pre-treatment steps (reductive and oxidative pre-treatment at 150 °C, followed by another oxidative step at 300 °C), the temperature dependent conversions ('light-off curves') shifted significantly to higher temperatures for all catalysts except the brookite supported catalyst ( $T_{50} = 7$  °C (anatase), 48 °C (rutile),  $-10$  °C (brookite), and 21 °C (P25)). The authors ascribed the loss in activity to changes in the TiO<sub>2</sub> morphology and in the size and shape of the Au NPs, to a growth of the initial Au rafts of small sizes (<2 nm) into 3D particles with large sizes (>10 nm) during oxidative treatment at 300 °C. The Au NPs agglomerated most strongly on the rutile phase, while the brookite based catalysts seemed to be least affected by the pre-treatment procedure. (Au NP growth on P25 was not quantified.) Rather similar observations were reported by Comotti *et al.*, who found that the activities of fresh Au catalysts, prepared by colloidal deposition on P25, rutile and anatase TiO<sub>2</sub>, were little different ( $T_{50} = 5, 5, -12$  °C), respectively.<sup>357</sup> The situation changed drastically, however, after calcination at different temperatures. For instance, after calcination at 550 °C, the  $T_{50}$  temperature for P25, anatase and rutile supported catalysts increased to 38, 100 and 100 °C, respectively. This led the authors to the conclusion that the catalytic activity depends little on the TiO<sub>2</sub> modification. The strong deactivation after calcination at 550 °C was attributed to the changes of the support and agglomeration of the Au NPs.<sup>357</sup> Overbury *et al.* also obtained a rather high activity for mesoporous Au–TiO<sub>2</sub> catalysts (SSA = 250 m<sup>2</sup> g<sup>-1</sup>, DP–Au Ø 3.5 nm, 9–14 wt% Au) after pre-treatment at 150 °C in H<sub>2</sub>–He, with  $T_{50} = -10$  °C as compared to  $T_{50} = -37$  °C for Au/P25.<sup>324</sup>

We recently studied the influence of the TiO<sub>2</sub> structure (rutile, anatase, and a mixture of anatase and rutile) and of the specific surface area in mesoporous Au–TiO<sub>2</sub> catalysts on the CO oxidation activity of these catalysts. Oxide supports were synthesized *via* a water-based sol–gel process.<sup>356</sup> Au loading was performed *via* a DP procedure, finally the fresh catalysts were activated by oxidative pre-treatment (350 °C for 30 min in 10% O<sub>2</sub>–N<sub>2</sub>). We found that a mesoporous (106 m<sup>2</sup> g<sup>-1</sup>) anatase support led to a significantly higher CO oxidation activity at 80 °C, both in terms of the Au mass normalized rates and in TOF numbers, than the use of a non-porous P25 support (56 m<sup>2</sup> g<sup>-1</sup>). However, when going to supports with higher specific surface areas (176 m<sup>2</sup> g<sup>-1</sup> anatase, 240 m<sup>2</sup> g<sup>-1</sup> anatase/rutile) or to a rutile support (160 m<sup>2</sup> g<sup>-1</sup>), the activity was comparable with that of Au/P25 catalysts. All catalysts deactivated strongly with time on stream (~60–70% over 1000 min). Since TEM measurements did not reveal any changes in Au NP size or in the structural texture of the support, growth/agglomeration of Au NPs can be excluded as origin for the deactivation.

Investigating a number of Au catalysts supported on high surface-area anatase with various surface areas (commercial source, 10, 37, 45, 90, 240, 305 m<sup>2</sup> g<sup>-1</sup>), Moreau *et al.* found a distinct correlation between the Au mass specific CO oxidation rate and the specific surface area (conversion measurements between  $-90$  and 20 °C, long-term measurements at  $-80$  °C).<sup>358,359</sup> All catalysts were prepared by the DP method at pH 9.

Reaction measurements were performed with no extra pre-treatment, running the reaction at 20 °C until it was stable, and the temperature was then lowered to  $-80$  °C. Long term activity tests were conducted at  $-80$  °C. The lowest rate was observed with the lowest specific surface area (SSA) of 10 m<sup>2</sup> g<sup>-1</sup>. The maximum rate was observed for the support with the next lowest specific surface area (37 m<sup>2</sup> g<sup>-1</sup>), and then it declined again as the surface area of the catalysts increased from 37 to 305 m<sup>2</sup> g<sup>-1</sup>. The authors had no obvious explanation for this progressive decrease in activity with increasing SSA. A high surface area Au/rutile catalyst (100 m<sup>2</sup> g<sup>-1</sup>) showed also a high activity, slightly higher than that of the anatase supported catalyst with about the same SSA. In long term measurements, the authors observed that for catalysts with high SSA the activity increased dramatically, from ~5 to 90% conversion during the first few hours, which did not happen with low SSA supports. They believed that this is due to ongoing decomposition of the Au precursor (HAuCl<sub>4</sub>), which takes longer time on high SSA supports. Au/P25 as well as the anatase supported Au catalyst with 10 m<sup>2</sup> g<sup>-1</sup> exhibited a slow decrease in activity (from 80 to 50% conversion over 100 h). The authors believed that the different tendencies for deactivation are mainly caused by two factors: (i) a much slower growth of the Au NPs on the high surface area supports due to their larger separation and/or by (ii) a more facile migration of reaction inhibiting carbonate species from the perimeter of the Au NPs to the support, plus a higher uptake capacity of the support surface. It should be noted, however, that a proper TEM analysis of the Au particle sizes is missing.

Zhu *et al.* investigated the activity of Au catalysts supported on anatase whiskers in conversion measurements.<sup>360</sup> The anatase whiskers were prepared from potassium ditanate whiskers, which were acid-washed to obtain protonic titanate, and then calcined at 300 and 600 °C for 2 hours to get two different TiO<sub>2</sub> whisker samples. The Au catalysts were prepared by a urea based DP method (for both catalysts 1 wt% Au), yielding rather large Au particle sizes of 8.5–13.5 nm and 6.5–11.5 nm for an anatase nanowhisker-600 catalyst (calcined at 600 °C, 55 m<sup>2</sup> g<sup>-1</sup>) and a Au/anatase nanowhisker-300 catalyst (calcined at 300 °C, 141 m<sup>2</sup> g<sup>-1</sup>), respectively. The Au particle size of the Au/P25 reference catalyst was not given. In contrast to the above trends, they found a slightly decreasing activity with increasing surface area. The activity followed the order Au/anatase nanowhisker catalyst (55 m<sup>2</sup> g<sup>-1</sup>), Au/P25 (1 wt%, 56 m<sup>2</sup> g<sup>-1</sup>), and a Au/anatase nanowhisker catalyst (141 m<sup>2</sup> g<sup>-1</sup>) with  $T_{50}$  values of 50, 40 and 30 °C, respectively (reaction temperature 20–160 °C; 1% CO, 1.98% O<sub>2</sub>, rest He). The authors associated the slightly higher activity of the highly crystalline TiO<sub>2</sub> nanowhisker-600 supported catalyst with the morphology of particles, with a higher ratio of low-coordinated surface sites suitable for strong attachment of Au NPs. The differences, however, are very small.

Beck *et al.* also investigated the influence of the support structure on the CO oxidation activity using different TiO<sub>2</sub> modifications and compared them with Au/P25.<sup>361</sup> They prepared two TiO<sub>2</sub> samples, pure brookite and a brookite–anatase mixture, by a precipitation method. The Au catalysts were prepared by two different methods, (i) a sol method (SAu<sub>15</sub>, SAu<sub>6</sub> and SAu<sub>5</sub>),

where Au sols were prepared and deposited on the TiO<sub>2</sub> supports upon addition of stabilizer poly(diallyldimethylammonium)chloride (PDDA), and (ii) a DP method using urea. The samples prepared by the sol method exhibited rather large Au NPs, using the sol SAu<sub>15</sub> the Au mean particle size for all three supports was around 15 nm in the as-prepared form and between 15 and 17 nm after calcination. Catalysts using SAu<sub>6</sub> and SAu<sub>5</sub> sol showed mean Au sizes between 4 and 6 nm for as prepared catalysts and between 6 and 10 nm after calcination. The smallest Au particle size was reached using the DP-urea method, with mean Au particle sizes between 3 and 5 nm after calcination (not mentioned before calcination). For the Au catalysts prepared by the DP-urea method and prior to any subsequent pre-treatment, the activity followed the order: Au/P25 (denoted as Au/A-R) ~ Au/B-A > Au/B. After activation at 400 °C in 10% O<sub>2</sub> in Ar, the activities changed and now followed the order: Au/B-A > Au/P25 >> Au/B. The authors tentatively explained the lower activity of the brookite supported catalyst by a higher intrinsic activity of the perimeter sites of the Au–TiO<sub>2</sub> interface, where anatase has a significantly higher activity compared to rutile and brookite. The drop in activities after oxidative pre-treatment was attributed to an increasing size of the Au NPs.

Bokhimi *et al.* investigated the activity of rutile supported Au–TiO<sub>2</sub> catalysts (specific surface area unknown) in conversion measurements and compared it with those of Ir–TiO<sub>2</sub> and of Au–Ir–TiO<sub>2</sub> (rutile) supported Au catalysts.<sup>362</sup> Rutile TiO<sub>2</sub> was prepared by hydrothermal synthesis at 80 °C, deposition of Au, Ir and IrAu was performed by DP methods (metal loading 4 wt% Au for Au–TiO<sub>2</sub>, 4 wt% Ir for Ir–TiO<sub>2</sub>, 4 wt% Ir and 4 wt% Au for Au–Ir–TiO<sub>2</sub>), particle sizes: Au ~ 2–3 nm, Ir–Au ~ 1 nm, Ir: ~ 1 nm). After activation in H<sub>2</sub>, they observed high CO oxidation activities already below room temperature for the Au–Ir–TiO<sub>2</sub> and Au–TiO<sub>2</sub> catalysts, while for the Ir–TiO<sub>2</sub> catalyst reaction started only at 50 °C. The activity followed the order Au–Ir–TiO<sub>2</sub> > Au–TiO<sub>2</sub> > Ir–TiO<sub>2</sub>. For the Au–TiO<sub>2</sub> catalyst, also the influence of the activation temperature was investigated, the *T*<sub>50</sub> temperature was found to increase slightly from 5 °C via 10 °C to 15 °C after reductive pre-treatment at 300, 400 and 500 °C, respectively. The higher activity for Au–Ir samples was tentatively explained by a not further specified synergetic effect of Ir and Au in the small, mixed metal NPs (1 nm and respectively). Long-term aging (7 months) was found to deactivate the Ir–Au–TiO<sub>2</sub> catalyst. The original activity could, however, be almost quantitatively regained upon reductive treatment at 300 °C. Based on these findings and on additional evidence from IR measurements, the deactivation was related to the accumulation of carbonates during ageing.

It is evident from the above data that quantitative answers to the main questions in this section, on the influence of the specific surface area and the structure/modification as well as the morphology of the TiO<sub>2</sub> substrate on the CO oxidation activity of the Au–TiO<sub>2</sub> catalysts are hardly possible. This is mainly due to experimental reasons. In most cases, the variation in one of these properties was accompanied also by changes in other critical parameters such as Au loading or Au particle sizes. Second, it is almost impossible to compare the results of the different activity measurements, since (i) there is

no general protocol for the catalytic measurements (reaction conditions including composition of the reaction gas mixture, kinetic measurements *vs.* conversion measurements, *etc.*) and since (ii) essential parameters such as amount of examined catalysts (in conversion experiments), Au loading/particle size, *etc.* are not given or not known. Furthermore, different procedures for the activation procedure may further affect the activities by varying the surface chemistry of the supports. At best, it is possible to map out trends, which are summarized in the following:

- The use of high surface area supports seems to lead to small but clear improvements in the activity and deactivation behavior, compared to the standard non-porous Au/P25 catalyst for similar reaction conditions and similar Au loading/particle size.
- There is an optimum value for the specific surface area, for higher surface areas the activity decreases again.
- The influence of the crystalline phase (anatase, rutile, brookite or their mixtures) on the reaction and activity is not straightforward.

A better understanding, however, would require more systematic measurements performed under better experimental control. The use of preformed Au NPs as done in colloidal deposition procedures may be helpful.

**5.3.2 Binary mixed oxide Au catalysts.** In this section, we will discuss the catalytic performance of Au catalysts supported on various mesoporous binary Si–Ti mixed oxides (see Table 3). This also includes well established mesoporous silica structures such as MCM-41, MCM-48 or SBA-15, which were modified with metals oxides, mainly TiO<sub>2</sub>, using different experimental approaches.

*MCM-48.* Bandyopadhyay *et al.* studied the catalytic properties of Au catalysts supported on Ti modified MCM-48 (Ti-MCM-48).<sup>363</sup> The support material was prepared by a post-synthesis wet impregnation method of MCM-48 (dry MCM-48 material was reacted with tetrabutylorthotitanate, the impregnation was performed 3 times, yielding about 15% Ti), which deposits TiO<sub>2</sub> on the inner surface of the MCM-48 material. Au loading was performed by a DP method (3 wt% Au). The Au NPs are deposited inside the porous channel system, the size is between 1.9 and 2.7 nm (pore size ~ 2.8–2.9 nm). Conversion measurements performed on the fresh catalysts (no extra pre-treatment) showed that these catalysts were highly active for CO oxidation, showing a *T*<sub>50</sub> of –20 °C even after the 3rd cycle of temperature screening. In order to test its thermal stability, the catalyst was heated to 200 °C, retaining the same CO oxidation activity. Overall, the TiO<sub>2</sub> surface coverage leads to a significant improvement of the CO oxidation activity of the Au/MCM-48 catalysts.

Closely related catalysts were investigated by Narkhede *et al.*<sup>327</sup> The catalysts were prepared by post-synthetic wet impregnation using titanylacetylacetonate, which lead to Au–TiO<sub>2</sub> clusters in the channel system of the MCM-48 framework. The pore system was, however, significantly perturbed after Au introduction *via* a conventional DP method. In conversion measurements, these catalysts were found to be rather active, with reproducible light-off temperatures (onset of the light-off curve) between –23 and –33 °C in the first

**Table 3** Binary mixed oxide Au catalysts

Support preparation			Au preparation/characteristics			Catalytic reaction conditions		Catalytic activity/stability								
Catalyst	Synthesis	SSA (m <sup>2</sup> /g)	Method	Au (wt%)	Au NP Ø (nm)	Au NP Ø after re-action (nm)	Atmosphere/ T °C	PT	Deactivation (%)	T <sub>50</sub> (fresh) (°C)	T <sub>50</sub> (PT1) (°C)	T <sub>50</sub> (PT2) (°C)	T <sub>50</sub> (PT3) (°C)	T <sub>50</sub> (°C)	RR	Ref.
Part 1																
Au/Ti-MCM-48	Post-synthesis wet impreg. 3-times, ~15 wt% TiO <sub>2</sub>	n.m.	DP	3	1.1–1.2	Stable to sintering up to 200 °C	1% CO, 20% O <sub>2</sub> , N <sub>2</sub>	Heated to 200 °C	n.m.	1st ramp –20	2nd ramp –30	3rd ramp –20	n.m.	n.m.	n.m.	[363]
Au/Ti-MCM-48	Post synthesis wet impregnation	965 (after Au loading 820)	DP	3 to 4	Inside porous system and on the surface	n.m.	1% CO/air	Inert gas, 400 °C	n.m.	T <sub>50</sub> Range –33 to –23	2nd ramp 4	3rd ramp 7	After PT –48	n.m.	n.m.	[327]
Au/ATM-1 (11.1 wt% Ti)	Post synthesis wet impregnation	n.m.	DP	4.1	Average Au particle size (nm)@250 °C <1 nm (EXAFS)	n.m.	1% CO, 20% O <sub>2</sub> , He	250 (PT1), 400 (PT2), 500 °C (PT3), He	All below: Carbonates	–23	n.m.	n.m.	n.m.	n.m.	n.m.	[364]
Au/SBA-15	All below: HT, 932	DP	DP	1.0	15 ± 5	n.m.	All below:	All below:	n.m.	n.m.	0	n.m.	n.m.	n.m.	n.m.	All below:
Au/SBA-15-8.1T	post synthesis wet	555	DP	3.6	4.0 ± 1.5	n.m.	1% CO, 1% O <sub>2</sub> , air	200 °C, 4 h	n.m.	n.m.	30	n.m.	n.m.	n.m.	n.m.	[366]
Au/SBA-15-12.8T	wet	537	DP	1.7	4.3 ± 1.5	n.m.	O <sub>2</sub> , N <sub>2</sub>		n.m.	n.m.	129	n.m.	n.m.	n.m.	n.m.	
Au/SBA-15-25.1T	impregnation	476	DP	3.0	7.2 ± 3.2	n.m.			n.m.	n.m.	65	n.m.	n.m.	n.m.	n.m.	
Au/SBA-15-41.3T		316	DP	2.4	n.m.	n.m.			n.m.	n.m.	202	n.m.	n.m.	n.m.	n.m.	
Au/TiO <sub>2</sub>		17	DP	1.1	3.0 ± 1.2	n.m.			n.m.	n.m.	Below 0	n.m.	n.m.	n.m.	n.m.	
Au/SBA-15-Ti-DP	All below: Surface hydroxyl hydrolysis	5 wt% Ti, 556 m <sup>2</sup> g <sup>–1</sup>	DP	0.62	5.1 ± 2.9	4.8 ± 1.8	All below: 0.54% CO, 9.1% O <sub>2</sub> , He	400 °C, 20% O <sub>2</sub> /He, 1 h	n.m.	105	105	n.m.	n.m.	n.m.	n.m.	All below: [367]
Au/SBA-15-Ti-PDDA		n.m.	CD_PDDA	1.47	5.7 ± 2.1	6.7 ± 3.6			n.m.	235	235	n.m.	n.m.	n.m.	n.m.	
Au/SBA-15-Ti-PVA		n.m.	CD_PVA	2.47	2.7	2.9			n.m.	160	160	n.m.	n.m.	n.m.	n.m.	
Part 2																
Au/Ti-SBA-15	Surface sol–gel	n.m.	DP	n.m.	0.8–1.0	0.9–1 (150 °C, H <sub>2</sub> )	All below: 1% CO/air	All below: 300 °C, 8% O <sub>2</sub> /He, 30 min	No deactivation over 16 h	–33	–25	n.m.	n.m.	n.m.	n.m.	All below: [368]
Au/P25	Commercial	n.m.	DP	n.m.	n.m.	n.m.	All below:	All below: O <sub>2</sub> /He, 30 min	n.m.	–40	25	n.m.	n.m.	n.m.	n.m.	
Au/SBA-15-1Ti	All below: post synthesis wet	~800	DP	2.7	3.5 ± 0.6	n.m.	1% CO, 1% O <sub>2</sub> , N <sub>2</sub> , 80 °C	400 °C, 10% O <sub>2</sub> /N <sub>2</sub> , 30 min	All below: at 80 °C after 1000 min rx: 70%	n.m.	n.m.	n.m.	n.m.	n.m.	1.4/ 0.3	All below: [353]
Au/SBA-15-2Ti	impregnation	~700	DP	2.2	4.9 ± 1.6	n.m.				n.m.	n.m.	n.m.	n.m.	n.m.	2.2/ 0.5	
Au/SBA-15-3Ti		~500	DP	4.2	n.m.	n.m.				n.m.	n.m.	n.m.	n.m.	n.m.	3.9/ 0.6	

A, anatase; R, rutile; B, brookite; HT, hydrothermal; SSA, specific surface area; IE, ionic exchange; DP, deposition–precipitation method; CD, colloidal deposition method; n.m., not mentioned; PT, pre-treatment; RR, reaction rate (mol<sub>CO</sub> g<sub>Au</sub><sup>–1</sup> s<sup>–1</sup> × 10<sup>4</sup>) either initial or initial/final after 1000 min on stream.

A, anatase; R, rutile; B, brookite; HT, hydrothermal; SSA, specific surface area; IE, ionic exchange; DP, deposition–precipitation method; CD, colloidal deposition method; n.m., not mentioned; PT, pre-treatment; RR, reaction rate (molCO g<sub>Au</sub><sup>–1</sup> s<sup>–1</sup> × 10<sup>3</sup>) either initial or initial/final after 1000 min on stream.



screening cycle. In a later report from the same group,<sup>364</sup> they determined extremely small Au particle sizes of <1 nm diameter from EXAFS measurements. For the 'as-prepared' catalyst, they determined light-off temperatures between -23 and 7 °C upon activation in the feed stream. Significant poisoning of the catalysts could be removed by an inert gas treatment at 400 °C, which lowered the light-off temperature to -48 °C. Under similar reaction conditions, a 1.5 wt% Au-TiO<sub>2</sub> catalyst available from the World Gold Council<sup>365</sup> yielded a light-off temperature of 12 °C in the first run (no pre-treatment).

**SBA-15.** Peza-Ledesma investigated the CO oxidation activity of Au catalysts based on mesoporous silica (SBA-15) material, which after synthesis was modified with different amounts of titania (0, 8.1, 12.8, 25.1, 41.3, 65.1 wt%), using titanium isopropoxide in 2-propanol.<sup>366</sup> For a reference catalyst, TiO<sub>2</sub> was synthesized by a sol-gel method using titanium isopropoxide in 2-propanol. Deposition of Au NPs was performed by a DP method using HAuCl<sub>4</sub>·3H<sub>2</sub>O at pH 11 and NaOH as an adjusting agent. Prior to the reaction, the catalysts were calcined in air (200 °C, 240 min). The mean size of the Au NPs, determined by TEM analysis after drying the catalysts in air at 110 °C for 18 h, increased in the order Au-TiO<sub>2</sub> (3.0 ± 1.2 nm) < Au/SBA-15/8.1% TiO<sub>2</sub> (4.0 ± 1.5 nm) < Au/SBA-15/12.8% TiO<sub>2</sub> (4.3 ± 1.5 nm) < Au/SBA-15/25.1% TiO<sub>2</sub> (7.2 ± 3.2 nm) < Au/SBA-15/41.3% TiO<sub>2</sub> (15 ± 5 nm). CO conversion measurements revealed that the Ti doped Au-Ti-SBA-15 catalyst with the lowest Ti content (8.1 wt% Ti) showed the highest activity ( $T_{50}$  = 30 °C). One should note, however, that the activity is rather low compared with that of the standard Au/P25 catalyst, which is at least partly related to the bigger size of the Au NPs. No measurable activity was found for a pure SiO<sub>2</sub> supported Au/SBA-15 catalyst. The difference in activity between Au/SBA-15 and TiO<sub>2</sub> modified Au-Ti-SBA-15 catalysts was qualitatively attributed to the higher dispersion of the Au NPs on the latter catalysts compared to the Au-SiO<sub>2</sub> one.

Beck *et al.* compared the CO oxidation performance for Au-Ti-SBA-15 catalysts prepared by three different methods: (i) by DP, (ii) by deposition of Au colloids stabilized with PVA, and (iii) by deposition of Au colloids stabilized with PDDA.<sup>367</sup> The Ti-SBA-15 samples (5 wt% Ti) were prepared post-synthetically by surface hydroxyl hydrolysis using Ti-isopropoxide in anhydrous ethanol suspension of SBA-15. The Au concentration was 0.62, 1.47 and 2.47 wt% for Au-Ti-SBA-15-DP > Au-Ti-SBA-15-PVA > Au-Ti-SBA-15-PDDA. In the freshly prepared catalysts, the size of the Au NPs decreased in the order Au-Ti-SBA-15-PDDA (5.7 ± 2.1 nm) > Au-Ti-SBA-15-DP (5.1 ± 2.9 nm) > Au-Ti-SBA-15-PVA (2.7 nm). The same order was observed after the reaction (6.7 ± 3.6 nm, 4.8 ± 1.8 nm, 2.9 ± 1.0 nm). The CO oxidation activity was determined in CO conversion measurements, using different amounts of the respective catalysts with the same amount of Au. Prior to the reaction, all catalysts were calcined *in situ* at 400 °C (20% O<sub>2</sub>-He, 60 min). Comparing the light-off temperatures, the authors determined the following order of activity: Au-Ti-SBA-15-DP > Au-Ti-SBA-15-PVA > Au-Ti-SBA-15-PDDA. None of the tested catalysts, however, reached the activity of the standard Au/P25 catalyst.

In contrast, Yan *et al.* reported highly active Au catalysts supported based on SBA-15 which was uniformly covered by a

monolayer of TiO<sub>2</sub> in a surface sol-gel process.<sup>368</sup> Au loading was performed *via* a DP process (Au amount not mentioned). The Au NPs were deposited inside the channel system (0.8–1.0 nm). The as-synthesized catalyst showed a high activity in conversion measurements, yielding a  $T_{50}$  value of -33 °C, which is comparable with the activity of Au/P25 ( $T_{50}$  = -40 °C). Upon calcination in 8% O<sub>2</sub>-He (300 °C, 30 min), the activity of the Au/P25 catalyst decreased markedly, as shown by the shift of the light-off curve by ~50 °C to higher temperature, while the activity of the monolayer TiO<sub>2</sub> modified Au/SBA-15 catalyst did not change significantly. This deactivation was primarily attributed to the aggregation of gold nanoparticles on the Au/P25 catalyst, while on the TiO<sub>2</sub> modified Au/SBA-15 catalyst the very small Au NPs seem to be stabilized against growth.

Recently, we investigated the potential of Au catalysts supported on SBA-15, which was surface modified by uniform TiO<sub>2</sub> films of 1–3 monolayers thickness.<sup>353</sup> These modified supports were prepared in a surface sol-gel approach, by post-synthetic treatment of silica SBA-15 with a solution of Ti(O<sup>i</sup>Pr)<sub>4</sub>.<sup>350</sup> Subsequently, the catalysts were prepared by a DP method and subsequent activation by oxidative pre-treatment (10% O<sub>2</sub>-N<sub>2</sub>, 400 °C, 30 min). Kinetic measurements showed a clear trend in the CO oxidation behavior. While the pure Au/SBA-15 (1 wt% Au, mean Au NP diameter 6.1 nm) shows nearly no activity in the CO oxidation reaction (1% CO, 1% O<sub>2</sub>, rest N<sub>2</sub>), the activity increases with increasing number of TiO<sub>2</sub> layers (Au loading 2.7, 2.2 and 4.2 for 1, 2 and 3 TiO<sub>2</sub> layers, respectively, and mean Au particle sizes of 3.5 nm and 4.9 nm for 1 and 2 TiO<sub>2</sub> monolayers), reaching the activity of a standard Au/P25 catalyst at a TiO<sub>2</sub> film thickness of 3 monolayers of TiO<sub>2</sub>. The deactivation was comparable to that of the standard Au/P25 catalyst, with about 70% deactivation after 1000 min on stream.

**Other mixed oxides (see Table 4).** Zhu *et al.* investigated the CO oxidation behavior of Au/P25 catalysts surface modified by SiO<sub>2</sub> decoration.<sup>369</sup> The calcined Au/P25 catalysts with 3.3 wt% Au loading were decorated with SiO<sub>2</sub> by chemical grafting, using three different Si precursors. For comparison, they prepared an Au-SiO<sub>2</sub>-TiO<sub>2</sub> catalyst, where the mixed oxide SiO<sub>2</sub>-TiO<sub>2</sub> material was produced first by addition of tetramethylorthosilicate to the TiO<sub>2</sub> re-dispersed in ethanol, followed by Au loading on the mixed oxide support by a DP procedure. The catalytic activity was characterized by conversion measurements (light-off curves), both for the fresh catalysts and after calcination at 500 or 700 °C in 8% O<sub>2</sub> in He for 1–5 h. For the non-modified Au/P25 catalyst, the  $T_{50}$  temperature was -37 °C after calcination at 300 °C, and it steadily shifted to higher temperature upon calcination at 500 °C for 1, 2 and 3 h ( $T_{50}$  = 30, 84 and 127 °C, respectively) and at 700 °C ( $T_{50}$  = 196 °C), in agreement with the increasing size of Au NPs, as determined by XRD. For the SiO<sub>2</sub> modified catalysts, a  $T_{50}$  value between 140–240 °C was obtained on the fresh, non-calcined catalyst. Upon calcination at 500 °C for 1 h, this decreased strongly to 15–30 °C. This activation was attributed to the removal of residual organic fragments. Upon longer calcination at 500 °C or calcination at 700 °C, the  $T_{50}$  temperature increased again to 60–110 °C. Comparing the activities after calcination at 500 °C for 1 h, the SiO<sub>2</sub> decorated

**Table 4** Other mixed oxide Au catalysts

Support preparation			Au preparation/characteristics		Catalytic reaction conditions		Catalytic activity/stability				Ref.			
Catalyst	Synthesis	SSA (m <sup>2</sup> /g)	Au (wt%)	Au NP Ø (nm)	Au NP Ø after reaction (nm)	Atmosphere/ T °C	PT	Deactivation (%)	T <sub>50</sub> (fresh) (°C)	T <sub>50</sub> (PT1) (°C)		T <sub>50</sub> (PT2) (°C)	RR	
Au/TiO <sub>2</sub> (P25)	Commercial	—	3.3	PT1 6.2	PT2 16.5	All below: 1% CO/air	All below: 500 (PT1), 700 (PT2) °C, 8% O <sub>2</sub> /He/ 1–5 h	Carbonates	n.m.	30	196	n.m.	All below: [369]	
SiO <sub>2</sub> (TMOS)/Au/TiO <sub>2</sub> SiO <sub>2</sub> (APTMS)/Au/TiO <sub>2</sub> SiO <sub>2</sub> (BOS)/Au/TiO <sub>2</sub> Au/SiO <sub>2</sub> (TMOS)/TiO <sub>2</sub>	All below: Pre-formed Au/TiO <sub>2</sub> decorated by SiO <sub>2</sub> <i>via</i> solution based approach	0.1 0.06 0.004 0.11	2.2 2.5 2.5 0.1	5.3 5.4 5.3 n.m.	6.5 7.1 12 n.m.			22	239 228 141 160	27 26 15 n.m.	64 85 110 > 520	n.m. n.m. n.m. n.m.		
	Commercial	—	1	PT1, 2, 3, 4, 4.7, 4.7, 9.4, 17.0	n.m.	All below: 1% CO/dry air	All below: 5% O <sub>2</sub> /He/ 1 h	n.m.	–41	n.m.	n.m.	n.m.	All below: [370]	
	All below: Au/P25 calcined at 250 °C, ALD of SiO <sub>2</sub>	0.06 0.11	1 1	4.7, 4.8, 6.1, 8.5 After 700 °C 5.8 nm	n.m.			n.m. n.m.	112 220	100 260	n.m. n.m.	n.m. n.m.	n.m. n.m.	
	All below: Surface sol-gel	n.m. n.m. n.m. n.m. n.m. n.m.	7.9 10.3 11.7 5.1 2.7 6.8 10.3	24.5 8 21.3 2.7 n.m. 3.8 7.7	n.m.	All below: 1% CO/dry air	All below: 8% O <sub>2</sub> /He (PT1), 50% H <sub>2</sub> /Ar (PT2)	n.m. n.m. n.m. n.m. n.m.	Unstable 7.8 –22 –44 –45 –31	n.m. 12 –11 –32 –95 < –98	n.m. 43 –18 –54 –55 –32	n.m. n.m. n.m. n.m. n.m.	All below: [326]	
Au/titania coated silica	HT	n.m.	3	2 (up to 550 °C)	3.2 (600 °C), 4.7 (700 °C)	1% CO, 21% O <sub>2</sub> , 78% N <sub>2</sub> , rel. TOF at 63 °C	500 °C (PT1) and 700 °C (PT2), air, 4 h	~30	n.m.	1–1.5	5.0	n.m.	[332]	
Au/Si <sub>x</sub> Ti <sub>1–x</sub> O <sub>2</sub> (4 : 1)-A Au/Si <sub>x</sub> Ti <sub>1–x</sub> O <sub>2</sub> (1 : 10)-A Au/Si <sub>x</sub> Ti <sub>1–x</sub> O <sub>2</sub> (1 : 19)-A Au/Si <sub>x</sub> Ti <sub>1–x</sub> O <sub>2</sub> (1 : 34)-A Au/Si <sub>x</sub> Ti <sub>1–x</sub> O <sub>2</sub> (1 : 19)-pH = 10-A Au/Si <sub>x</sub> Ti <sub>1–x</sub> O <sub>2</sub> (1:34)-pH = 0-R Au/TiO <sub>2,m</sub> A Au/TiO <sub>2,m</sub> R	All below: Sol-gel, template: BRIJ56	3.9/1 1/8.6 1/13.1 1/22 1/15	0.2 2 1.3 1.6 1.6	2.6 ± 0.9 2.7 ± 1.0 2.1 ± 0.7 2.4 ± 1.0 2.0 ± 0.4	— 2.2 ± 0.6 2.2 ± 0.6 — 2.2 ± 0.3	All below: 1% CO, 1% O <sub>2</sub> , N <sub>2</sub> , 80 °C	All below: 89 400 °C, N <sub>2</sub> , 10% O <sub>2</sub> /N <sub>2</sub> , 30 min 66	89 78 67 66 68	n.m. n.m. n.m. n.m. n.m.	n.m. n.m. n.m. n.m. n.m.	n.m. n.m. n.m. n.m. n.m.	6.0/0.7 54.7/12.1 116.0/37.6 103.0/29.3 133.2/43.6	All below: [5]	
		1/17	70	3.2 ± 0.5	—			68	n.m.	n.m.	n.m.	n.m.	37.4/12.7	
		— —	175 160	26 4.8	3.0 ± 0.7 6.1 ± 1.5	— —			67 74	n.m. n.m.	n.m. n.m.	n.m. n.m.	37.2/12.4 34.8/9.2	
	A, anatase; R, rutile; B, brookite; HT, hydrothermal; SSA, specific surface area; IE, ionic exchange; DP, deposition–precipitation method; CD, colloidal deposition method; n.m., not mentioned; PT, pre-treatment; RR, reaction rate (molCo g <sub>Au</sub> <sup>–1</sup> s <sup>–1</sup> × 10 <sup>4</sup> ) either initial or initial/final after 1000 min on stream.													

A, anatase; R, rutile; B, brookite; HT, hydrothermal; SSA, specific surface area; IE, ionic exchange; DP, deposition-precipitation method; CD, colloidal deposition method; n.m., not mentioned; PT, pre-treatment; RR, reaction rate (mol<sub>CO</sub> g<sub>Au</sub><sup>–1</sup> s<sup>–1</sup> × 10<sup>4</sup>) either initial or initial/final after 1000 min on stream.

mixed oxide supported Au-SiO<sub>2</sub>-TiO<sub>2</sub> catalyst showed an activity comparable to that of a non-modified Au/P25 catalyst; after calcination at 700 °C they were even somewhat more active, which can be rationalized by a higher thermal stability of the Au NPs on the mixed oxide supported catalysts (6.5–12 nm compared to 16 nm on Au/P25). Nevertheless, all activities of the SiO<sub>2</sub> decorated Au/P25 catalysts are lower than that of the 300 °C calcined Au/P25 catalyst. For the Au-SiO<sub>2</sub>-TiO<sub>2</sub> catalyst (Si: Ti = 0.11 : 1), only very low Au loadings were reached, in the range of 0.1 wt%, compared to between 2.2 and 3.3 wt% Au for the other catalysts. Accordingly, the poor CO oxidation activity ( $T_{50}$  = 160 and > 520 °C after calcination at 300 and 700 °C) is mainly due to the negligible Au loading. Overall, the SiO<sub>2</sub> surface modification of the Au/P25 catalyst does not lead to an improvement of the CO oxidation performance, at least not under 'normal' reaction conditions.

Ma *et al.* investigated SiO<sub>2</sub>-Au-TiO<sub>2</sub> catalysts prepared by atomic layer deposition of SiO<sub>2</sub> on calcined Au-TiO<sub>2</sub> catalysts (*via* tetramethylorthosilicate (TMOS) evaporation).<sup>370</sup> Three samples were characterized by CO oxidation: Au/P25, SiO<sub>2</sub>-Au-TiO<sub>2</sub> (Si-Ti = 0.06) and SiO<sub>2</sub>-Au-TiO<sub>2</sub> (Si-Ti = 0.11). For the as-synthesized catalysts, the authors obtained  $T_{50}$  values of -41, 112 and 220 °C, respectively. After calcination at 300, 500 and 700 °C, the activities for SiO<sub>2</sub>-Au-TiO<sub>2</sub> with Si-Ti = 0.06 were similar, with  $T_{50}$  values between 90 and 140 °C. The similar activity even after high temperature treatment indicates a rather good thermal stability of the Au NPs. TEM measurements revealed Au NP sizes of ~4.7, 4.8, 6.1 and 8.5 nm for the SiO<sub>2</sub>-Au-TiO<sub>2</sub> (Si-Ti = 0.06) after synthesis and after calcination at 300, 500 and 700 °C, respectively. The sample with the higher SiO<sub>2</sub> content showed an average Au NP size of 5.8 nm after pre-treatment at 700 °C, pointing to a higher stability of the AuNPs on the latter support, while the unmodified Au-TiO<sub>2</sub> catalyst showed average Au NP sizes of 4.7, 9.4, 17.0 nm after calcination at 300, 500 and 700 °C, respectively. The distinctly lower general CO oxidation activity of the SiO<sub>2</sub> modified Au-TiO<sub>2</sub> catalysts was convincingly explained by blocking of the active Au-TiO<sub>2</sub> interface perimeter sites by inactive SiO<sub>2</sub>.

Yan *et al.* modified fumed silica by a sol-gel process, by growth of TiO<sub>2</sub> or Al<sub>2</sub>O<sub>3</sub> monolayers or double layers or a combination of both oxides (Al<sub>2</sub>O<sub>3</sub>-TiO<sub>2</sub>, TiO<sub>2</sub>-Al<sub>2</sub>O<sub>3</sub>) on the silica material.<sup>326</sup> Au NPs were loaded *via* a DP method, followed by oxidative (8% O<sub>2</sub>-He) or reductive (50% H<sub>2</sub>-Ar) pre-treatment. The Au loadings and the mean particle sizes, as determined by XRD (from the Au(111) peak), were as follows: Au-Al<sub>2</sub>O<sub>3</sub>-SiO<sub>2</sub> (7.9 wt%, 24.5 nm), Au-Al<sub>2</sub>O<sub>3</sub>-Al<sub>2</sub>O<sub>3</sub>-SiO<sub>2</sub> (10.3 wt%, 8 nm), Au-TiO<sub>2</sub>-Al<sub>2</sub>O<sub>3</sub>-SiO<sub>2</sub> (11.7 wt%, 21.3 nm), Au-TiO<sub>2</sub>-SiO<sub>2</sub> (5.1 wt%, 2.7 nm), Au-TiO<sub>2</sub>-TiO<sub>2</sub>-SiO<sub>2</sub> (6.8 wt%, 3.8 nm), Au-Al<sub>2</sub>O<sub>3</sub>-TiO<sub>2</sub>-SiO<sub>2</sub> (10.3 wt%, 7.7 nm). The catalytic activity, determined in conversion measurements from light-off curves, was different for oxidative or reductive pre-treatment. The activity of the fresh catalysts and of catalysts calcined at 150 °C in O<sub>2</sub> followed the same order ( $T_{50}$  value for the fresh/calcined catalyst): Au-TiO<sub>2</sub>-TiO<sub>2</sub>-SiO<sub>2</sub> (-45, -55 °C)  $\approx$  Au-TiO<sub>2</sub>-SiO<sub>2</sub> (-44, -54 °C) > Au-Al<sub>2</sub>O<sub>3</sub>-TiO<sub>2</sub>-SiO<sub>2</sub> (-31, -32 °C) > Au-TiO<sub>2</sub>-Al<sub>2</sub>O<sub>3</sub>-SiO<sub>2</sub> (-22, -18 °C) > Au-Al<sub>2</sub>O<sub>3</sub>-Al<sub>2</sub>O<sub>3</sub>-SiO<sub>2</sub> (7.8, 43 °C). After reductive pre-treatment,

the activity decreased in the order: Au-Al<sub>2</sub>O<sub>3</sub>-TiO<sub>2</sub>-SiO<sub>2</sub> (> -98 °C) > Au-TiO<sub>2</sub>-TiO<sub>2</sub>-SiO<sub>2</sub> (-95 °C) > Au-TiO<sub>2</sub>-SiO<sub>2</sub> (-32 °C) > Au-TiO<sub>2</sub>-Al<sub>2</sub>O<sub>3</sub>-SiO<sub>2</sub> (-11 °C) > Au-Al<sub>2</sub>O<sub>3</sub>-Al<sub>2</sub>O<sub>3</sub>-SiO<sub>2</sub> (12 °C). The activity strongly depends on the structure of the support and on the pre-treatment. The highest activity was reached after the reductive pre-treatment for the Au-Al<sub>2</sub>O<sub>3</sub>-TiO<sub>2</sub>-SiO<sub>2</sub> composite material. The surface modification (functionalization) of silica material is an important tool for tailoring the properties of catalytically active materials, and the authors showed that structuring the support with monolayer precision can lead to highly active CO oxidation catalysts.

Tai *et al.* investigated Au catalysts prepared by loading thiol-capped Au NPs on alumina coated silica.<sup>332</sup> The Au NPs were stable against sintering up to 500 °C (2 nm) and started to agglomerate only after calcination at 600 °C (3.2 nm) and 700 °C (4.7 nm). The catalytic activity increased after calcination above 500 °C, most probably due to the presence of sulfur species (from the thiol capping agent), but the resulting TOF values of ~0.015 for reaction at -63 °C are not overly high.

Recently, we systematically studied the catalytic behavior of Si-Ti mixed oxide supported Au catalysts, aiming particularly at lowering the tendency for deactivation by tuning the surface activity.<sup>5</sup> The oxides were prepared using a sol-gel based synthesis with glycolated precursors (similarly to that used for mesoporous TiO<sub>2</sub> synthesis<sup>356</sup>), Au loading was performed by DP. After subsequent calcination (400 °C, 30 min, 10% O<sub>2</sub> in N<sub>2</sub>), Au NP sizes were between 2.6 and 3.2 nm. Au loading was 1.3–3.2 wt%, with a very low loading for the material with the highest Si content (Si:Ti = 4, mean Au particle size 2.6 nm). The CO oxidation activities (1% CO, 1% O<sub>2</sub>, rest N<sub>2</sub>, 80 °C), determined as Au mass specific rates in kinetic measurements under differential reaction conditions, were found to strongly depend on the Si-Ti ratio and on the TiO<sub>2</sub> morphology. Some of the mixed oxide supported Au catalysts exhibited activities significantly higher than that of the non-porous Au/P25 catalysts and slightly higher than those of mesoporous anatase supported Au-TiO<sub>2</sub> catalysts (see ref. 343, 349 and above). The initial-final Au mass normalized rates increased in the order: Au-Si<sub>x</sub>Ti<sub>1-x</sub>O<sub>2</sub>(4:1) < Au-Si<sub>x</sub>Ti<sub>1-x</sub>O<sub>2</sub>(1:34)-pH = 0 (rutile)  $\sim$  Au-TiO<sub>2,m</sub>(rutile polymorph)  $\sim$  Au-TiO<sub>2,m</sub>(anatase polymorph) < Au-Si<sub>x</sub>Ti<sub>1-x</sub>O<sub>2</sub>(1:10) < Au-Si<sub>x</sub>Ti<sub>1-x</sub>O<sub>2</sub>(1:34) < Au-Si<sub>x</sub>Ti<sub>1-x</sub>O<sub>2</sub>(1:19) < Au-Si<sub>x</sub>Ti<sub>1-x</sub>O<sub>2</sub>(1:19)-pH = 10.

Similarly to our observation for mesoporous TiO<sub>2</sub> catalysts, the anatase supported catalysts (Au-Si<sub>x</sub>Ti<sub>1-x</sub>O<sub>2</sub>(1:19), Au-Si<sub>x</sub>Ti<sub>1-x</sub>O<sub>2</sub>(1:19)-pH = 10) exhibit rather similar reaction characteristics, while the rutile supported (Au-Si<sub>x</sub>Ti<sub>1-x</sub>O<sub>2</sub>(1:34)-pH = 0) catalyst is much less active. We mainly attribute the difference to the smaller specific surface area (70 m<sup>2</sup> g<sup>-1</sup>) and larger size of the Au NPs (~3.2 nm) in the latter sample compared to a specific surface area of ~150 m<sup>2</sup> g<sup>-1</sup> and Au NP size of ~2.1 nm for the anatase supported catalysts. For all three mixed oxide catalysts, the activity decreased in the same exponential way during time on stream, reaching a nearly steady-state value of about 30% of the initial activity after about 500 min on stream. Overall, despite of some improvements in the activity of supported Au catalysts, this study revealed little progress in the main problem, in the long-term stability.



The mixed oxide phases seem to be better in stabilizing Au NPs at higher temperatures, allowing higher reaction temperatures compared to Au/P25. At 'normal' reaction temperatures, however, where deactivation is not related to Au NP growth/agglomeration, the concept of reducing the tendency for deactivation by modifying the surface acidity was not overly successful so far.

The above conclusion is characteristic also for the complete body of studies discussed in this section. Apparently, so far modifications in the surface chemistry of TiO<sub>2</sub> that are sufficient to significantly modify the deactivation behavior also lowered the activity to an extent that the catalyst is not attractive any more.

**5.3.3 Other "novel" supports (Table 5).** The previous sections have demonstrated that at least for the class of catalysts considered, Au catalysts supported by mesoporous TiO<sub>2</sub> and related materials, and for the reactions discussed, that high activity and tendency for deactivation seem to be correlated. In that case, one might think of other high surface area materials rather than modifying the support material. This may pave the way to improving the surface chemistry responsible for the catalyst deactivation while keeping the advantages introduced by the use of the mesoporous oxide substrates. Potential candidates would be classes of microporous and mesoporous materials, which found increasing use in commercial catalysts or as adsorbents due to their unique properties, *e.g.*, high specific surface area, regular well-defined pore systems, thermal stability, tunable acidity, *etc.* These materials are also ideal host material for metal NPs or for tuning their properties by inclusion of other elements. Despite their potential, there is up to now only little known on their use as support in Au catalysis. It should be noted that also this approach should be considered as an example for other reactions and mesoporous oxide supported catalysts.

Prime candidates are zeolites, which could equally well as mesoporous materials stabilize small Au NPs, providing it is possible to locate them in the pores of the zeolite matrix. Pestryakov *et al.* tested the potential of zeolites for the stabilization of Au and other metal NPs and for the formation of highly active metal NPs in the CO oxidation reaction (1% CO, 1% O<sub>2</sub>, no pre-treatment, pretreatment at 500 °C with He or O<sub>2</sub>).<sup>371</sup> Au catalysts were prepared by ionic exchange of H-mordenite (Si–Ti ratio = 15) with aqueous solution of [Au(NH<sub>3</sub>)<sub>4</sub>](NO<sub>3</sub>)<sub>3</sub>. The catalytic activity of a fresh Au/mordenite catalyst was negligible up to temperatures around 270 °C. After treating the Au/mordenite catalyst for 1 h in O<sub>2</sub> at 520 °C, the *T*<sub>50</sub> value reached 334–344 °C (up- and down-scan measurement). A similar activity was reached after pre-treatment at 520 °C in He (*T*<sub>50</sub> = 340 °C). Since the as-prepared catalyst obtained a high fraction of Au<sup>3+</sup> species, the authors believe that the increasing activity for CO oxidation pre-treatment is related to an increased fraction of metallic Au species. Though details on Au loading and Au particle sizes are missing, the activity seems to be extremely low on an absolute scale.

Jafari *et al.* used a DP method for loading Au NPs on Na/Y and H/Y zeolite supports (Au loadings of 3.89 wt% and 5.77 wt% for Au/Na–Y and Au/H–Y, respectively).<sup>372</sup>

Employing CO conversion measurements, they achieved 100% and 5% CO conversion at 20 °C on fresh untreated Au/Na–Y and Au/H–Y catalysts, respectively. After a thermal treatment at 400 °C (24 h), the conversion of CO at 20 °C changed to 65% and 15% for the Au/Na–Y and Au/H–Y catalysts, respectively. The authors explained the higher CO oxidation activity of the Au/H–Y catalyst by formation of more Au NPs confined inside the channel system. The increase with temperature may be related to the removal of chlorides, which remained on the external surface of the support during the DP process, upon the thermal treatment.

Recently, Huang *et al.* reported rather active Au catalysts for CO oxidation supported on hydroxylapatite (Ca<sub>10</sub>(PO<sub>4</sub>)<sub>6</sub>(OH)<sub>2</sub>), which was Au loaded by a DP(urea) procedure.<sup>373</sup> All samples contained 2.9 wt% Au, the size of the Au NPs was controlled by the calcination atmosphere, with mean Au NP sizes of 2.2, 2.9 and 3.7 nm for samples calcined in He, O<sub>2</sub> or H<sub>2</sub> at 300 °C for 30 min, respectively. Two types of catalytic measurements were performed, CO conversion measurements and kinetic measurements under differential reaction conditions. In CO conversion measurements (1% CO, 20% O<sub>2</sub>, He), the highest initial activity (*T*<sub>50</sub> = –10 °C) was obtained for the sample calcined in He. On the other hand, this also showed the highest deactivation on stream (90% after 90 min at 25 °C). Calcination in O<sub>2</sub> led to a lower activity (*T*<sub>50</sub>(initial) = 14 °C), but to the highest stability (30% deactivation) of the catalyst sample. The deactivation was attributed to the accumulation of surface carbonate species, the difference in the degree of deactivation was related to the different surface basicities of the support surfaces after calcination in various atmospheres, with the catalysts calcined in the O<sub>2</sub> atmosphere showing the lowest basicity.

Another type of material evaluated towards its potential as support for highly active Au are spinels (MgFe<sub>2</sub>O<sub>4</sub>). Jia *et al.* explored the catalytic behavior of Au–MgFe<sub>2</sub>O<sub>4</sub> catalysts, which were prepared by deposition of small Au NPs on spinel by colloidal deposition, using PVA as a stabilizing agent.<sup>374</sup> The catalyst (0.8 wt% Au, mean Au NPs size 1–5 nm) was activated in the reaction gas mixture (1% CO, 20% O<sub>2</sub>, N<sub>2</sub>) by ramping the temperature from –40 to 300 °C. CO conversion measurements (light-off curves) indicated a high initial activity (*T*<sub>50</sub> = –40 °C). The catalyst, however, rapidly deactivated, *e.g.*, by 76% after 100 min at –40 °C. The light-off measurement was repeated with a deactivated Au catalyst, after a full ramp from –40 to 300 °C, yielding a *T*<sub>50</sub> value of –18 °C. The effect of pre-treatment (O<sub>2</sub> (300 °C, 30 min), N<sub>2</sub> (300 °C, 30 min) and H<sub>2</sub> (200 °C, 30 min)) was investigated in additional measurements, always starting with a fresh catalysts, which was first activated in the reaction gas by ramping the temperature from –40–300 °C. The different pre-treatments resulted in the following order of activity (*T*<sub>50</sub>): Au–MgFe<sub>2</sub>O<sub>4</sub> oxidative pre-treatment (O<sub>2</sub> (–25 °C)) > Au–MgFe<sub>2</sub>O<sub>4</sub> reductive pre-treatment (H<sub>2</sub> (–9 °C)) > Au–MgFe<sub>2</sub>O<sub>4</sub> inert gas pre-treatment (N<sub>2</sub>) (8 °C). Keeping the temperature at –40 °C, the best long-term stability was reached over the catalysts pre-treated in oxygen. Deactivation was not caused by agglomeration of Au NPs which have the same size prior and after the catalytic test (2.2 and 2.6 nm, respectively). The highest activity/stability of the catalyst pre-treated in O<sub>2</sub> was explained by its capability to activate CO and supply active oxygen as based on CO titration experiments.

**Table 5** Other “novel” supports

Support preparation			Au preparation/characteristics		Catalytic reaction conditions		Catalytic activity/stability						
Synthesis	SSA (m <sup>2</sup> /g)	Method	Au (wt%)	Au NP Ø (nm)	Au NP Ø after reaction (nm)	Atmosphere/ T °C	PT	Deactivation (%)	T <sub>50</sub> (fresh) (°C)	T <sub>50</sub> (PT1) (°C)	T <sub>50</sub> (PT2) (°C)	RR	Ref.
Au/Mordenite	Commercial	n.m.	IE	n.m.	n.m.	1% CO, 1% O <sub>2</sub>	PT1: 500–520 °C, He; n.m. PT2: 520 °C, O <sub>2</sub>	n.m.	Negligible	67–100	0.75(–10)	n.m.	[371]
Au–NaY	Commercial	n.m.	DP	5.8	n.m.	All below: 0.5% CO, dried air/20 °C	All below: PT1: 400 °C, 24 h	All below: at 20 °C no deactivation	n.m.	Below 20	n.m.	n.m.	All below: [372]
Au–HY	Commercial	n.m.	DP	5.8	n.m.				90	80	n.m.	n.m.	
Hydroxylapatite (HAP)	Precipitation	79	DP	2.9	n.m.	All below: 1% CO, 20% O <sub>2</sub> , He/25 °C	All below:	n.m.	288	n.m.	n.m.	—	All below: [373]
Au/HAP–H <sub>2</sub>	Precipitation	81	DP	2.9	3.7		300 °C, 5% H <sub>2</sub> /Ar, 1 h	60	30	n.m.	n.m.	0.14	
Au/HAP–O <sub>2</sub>	Precipitation	83	DP	2.9	2.9		300 °C, 5% O/Ar, 1 h	30	14	n.m.	n.m.	0.25	
Au/HAP–He	Precipitation	84	DP	2.9	2.2		300 °C, He, 1 h	90	–10	n.m.	n.m.	0.08	
Au/ HAP–He–regenerated	Precipitation	n.m.	DP	2.9	2.3	n.m.		70	n.m.	n.m.	n.m.	0.15	
Spinel Au/MgFe <sub>2</sub> O <sub>4</sub>	Sol–gel	110	CD	0.8	1.5–5	1.5–5	All below: 1% CO/air	All below: after ramping from –40–300 °C; 300 after 100 min	270 –40	n.m. n.m.	n.m.	n.m.	All below: [374]
Au/MgFe <sub>2</sub> O <sub>4</sub>	Sol–gel	110	CD	0.8	1.5–5	1.5–5			–25 –9	n.m. n.m.	n.m.	n.m.	
Au/MgFe <sub>2</sub> O <sub>4</sub> –O <sub>2</sub>	Sol–gel	110	CD	0.8	1.5–5	1.5–5	O <sub>2</sub> 200 °C, H <sub>2</sub> 300 °C, N <sub>2</sub>	10 50 20	8	n.m.	n.m.	n.m.	
Au/Fe–P–O	Commercial	28	DP	5.5	1–3	2–20	All below: 1% CO/air	All below: 200 °C, 8% O <sub>2</sub> /He (PT1), 500 °C, 8% O <sub>2</sub> /He (PT2)	n.m.	–31	244	n.m.	All below: [375]
Au/Eu–P–O	Commercial	61	DP	8.5	2–6	6–15		At T <sub>room</sub> : 25 increased activity (70%)	n.m.	–28	68	n.m.	
Au/Ca–P–O	Commercial	21	DP	1.3	2–5	2–5		60	n.m.	–18	16	n.m.	
Au/P25	Commercial	50	DP	2.3	2–8	5–30		n.m.	n.m.	–36	140	n.m.	
Au/Pr–P–O	Commercial	57	DP	0.9	3–8	3–15		0	n.m.	n.m.	–49	n.m.	
Au@TiO <sub>2</sub>	See ref.	n.m.	—	n.m.	Core 10–15 nm	n.m.	10% CO/air 300 °C, 4 h	n.m.	n.m.	–220	n.m.	n.m.	[376]

A, anatase; R, rutile; B, brookite; HT, hydrothermal; SSA, specific surface area; IE, ionic exchange; DP, deposition–precipitation method; CD, colloidal deposition method; n.m., not mentioned; PT, pre-treatment; RR, reaction rate (mol·CO g<sub>Au</sub><sup>–1</sup> s<sup>–1</sup> × 10<sup>4</sup>) either initial or initial/final after 1000 min on stream.

A, anatase; R, rutile; B, brookite; HT, hydrothermal; SSA, specific surface area; IE, ionic exchange; DP, deposition–precipitation method; CD, colloidal deposition method; n.m., not mentioned; PT, pre-treatment; RR, reaction rate (mol<sub>CO</sub> g<sub>Au</sub><sup>–1</sup> s<sup>–1</sup> × 10<sup>4</sup>) either initial or initial/final after 1000 min on stream.

Ma *et al.* tried to develop a new catalyst system using commercial metal phosphates as support for Au NPs.<sup>375</sup> Au loading was performed by a DP method (0.9–8.5 wt% Au). After oxidative pre-treatment at 200 °C (8% O<sub>2</sub>–He), the activity as determined in CO conversion (light-off) measurements was highest for Au/P25 ( $T_{50}$  = –36 °C, 2.3 wt% Au, Au  $\varnothing$  2–8 nm) > Au–Fe–P–O ( $T_{50}$  = –31 °C, 5.5 wt% Au, Au  $\varnothing$  2–8 nm) > Au–Eu–P–O ( $T_{50}$  = –28 °C, 8.5 wt% Au, Au  $\varnothing$  2–8 nm) > Au–Ca–P–O ( $T_{50}$  = –18 °C, 1.3 wt% Au, Au  $\varnothing$  2–8 nm) > Au–Pr–P–O ( $T_{50}$  = 11 °C, 0.9 wt% Au, Au  $\varnothing$  3–8 nm). After oxidative pre-treatment at 500 °C, the order in activity changed significantly. The highest activity was obtained over Au–Pr–P–O ( $T_{50}$  = –49 °C, Au  $\varnothing$  3–15 nm), followed by Au–Ca–P–O ( $T_{50}$  = 16 °C, Au  $\varnothing$  2–5 nm) > Au–Eu–P–O ( $T_{50}$  = 68 °C, Au  $\varnothing$  6–15 nm) > Au/P25 ( $T_{50}$  = 140 °C, Au  $\varnothing$  2–5–30 nm) > Au–Fe–P–O ( $T_{50}$  = 244 °C, Au  $\varnothing$  2–20 nm). The main message is that compared to P25 these phosphate materials are better in stabilizing the Au NPs against particle growth at high temperatures, while under ‘normal’ reaction conditions the resulting catalysts are significantly lower in activity than standard Au/P25 catalysts.

Chen *et al.* investigated the CO oxidation performance of core-shell Au@TiO<sub>2</sub> particles.<sup>376</sup> These were prepared by depositing TiO<sub>2</sub> onto the surface of Au nanoparticles, by addition of tetrabutyl titanate solution diluted in absolute ethanol (with the volume ratio 1 : 100) to Au core nanoparticles (prepared by HAuCl<sub>4</sub> solution, sodium citrate solution and polyvinylpyrrolidone). Based on TEM analysis, the core-shell structure of Au@TiO<sub>2</sub> nanoparticles is comprised of a core with a size of 10–15 nm (Au) and a shell of a thickness of 1–3 nm (TiO<sub>2</sub>). The catalytic testing of the calcined catalyst (300 °C, 4 h) showed a  $T_{50}$  = 220 °C. The catalytic activity of the large Au particles was explained by three effects: (i) the formation of cracks in the core-shell particles during the heating process, which would enable contact of CO molecules with Au core, (ii) cracking induced irregularities in the Au surface which may offer more active sites and hence facilitate the catalytic process, and (iii) a high number of metal-support contacts.

The examples discussed above clearly demonstrate the potential of ‘non-traditional’ supports for the preparation of highly active Au catalysts. They also underline, however, that at present none of these materials has reached or even outperformed traditional oxide supports such as TiO<sub>2</sub> or Fe<sub>2</sub>O<sub>3</sub>, *etc.* as support material for highly active Au catalysts in the CO oxidation reaction. Considering the enormous amount of possible materials, there is a clear need for a knowledge based materials selection. The way for improvement, however, is open and promising. Furthermore, similar to the data in the preceding sections also these examples demonstrate the urgent need for generally accepted reaction conditions and for Au catalysts with comparable Au loading and NP sizes. Without more controlled experimental conditions, there is little hope for an overall understanding of the reaction mechanism and in particular of the role of the support. Finally, considering the main weakness of supported Au catalysts, their pronounced tendency for deactivation, we would like to stress the need for longer term measurements.

#### 5.4 Preferential CO oxidation

PROX reaction studies performed on mesoporous TiO<sub>2</sub> and/or TiO<sub>2</sub>–SiO<sub>2</sub> mixed oxide supported Au catalysts are rare

(for an overview see Table 6). For a better understanding of the ongoing discussion in this area, we also included a few studies on more traditional oxide supports in this section, which we found relevant.

In recent years we studied the effect of the structure and mesoporosity (pore size, BET surface area) of TiO<sub>2</sub> supports on the activity and selectivity of Au–TiO<sub>2</sub> catalysts in the selective CO oxidation reaction (the behavior of these catalysts in the CO oxidation reaction was already described in Section 6.1).<sup>343,349</sup> Similarly, we also investigated the effect of the presence of Si in the mesoporous mixed oxide Au–Si<sub>x</sub>Ti<sub>1–x</sub>O<sub>2</sub> catalysts on the selectivity and activity in H<sub>2</sub>-rich atmospheres.<sup>377</sup> The results were compared to findings in our previous studies on Au/P25.<sup>288,378</sup>

Comparing the activities in the selective CO oxidation, we did not find a significant increase during the 1000 min on stream compared to the standard, nonporous Au/P25 catalyst, which could be induced by the different physical properties (mesoporosity) of the TiO<sub>2</sub> support or the changed surface acidity in the mixed oxide phase. The activities were more or less comparable to that of a Au/P25 catalyst, except the higher activity of the mixed oxide supported catalyst with a Si–Ti ratio of 1 : 13. Also the selectivity seems to be little affected by the higher surface area of the mesoporous catalysts or the acidity of the mixed oxide support, being between ~45% (Au/P25) and 50–55% (Au/TiO<sub>2</sub> and Au/mixed oxides). Regarding the deactivation, the best stability was found for the mesoporous pure TiO<sub>2</sub> supported catalyst (support prepared with SDS as template, 106 m<sup>2</sup> g<sup>–1</sup>), where after 1000 min on stream the activity was still 97% of the initial value. For all other catalysts, the deactivation over 1000 min was around 20%. It should be noted that the deactivation under PROX reaction conditions is generally much lower than for CO oxidation in the absence of H<sub>2</sub>, which was explained by more facile decomposition of surface carbonates under these conditions, *e.g.*, *via* reaction to less stable bicarbonates.<sup>288</sup>

Ruszel *et al.* used Au–Ti–SBA-15 material with different Ti contents, prepared by impregnation of SBA-15 material with titanium isopropoxide in isopropanol, which was subsequently Au loaded *via* a DP procedure.<sup>379</sup> The distribution of Au NP sizes based on TEM analysis revealed that with increasing Ti content, the amount of the smallest Au NPs (1–2 nm) decreased, together with a simultaneous increase in the amount of bigger particles (5–8 nm). The authors found that for not too high Ti contents (up to 1.32 wt%) at 50 °C and a rather low H<sub>2</sub> content (CO : O<sub>2</sub> : H<sub>2</sub> = 2.3% : 2.3% : 10%), both the conversion and the selectivity were very high, with almost 100% selectivity and conversion, while for the highest Ti content (2.5 wt%) the activity decreased strongly. The performance of the best Au–Ti–SBA-15 catalysts in the PROX reaction was better than that of the Au–TiO<sub>2</sub> reference catalyst, distributed by the World Gold Council,<sup>365</sup> where at slightly different reaction conditions the selectivity at 50 °C amounted to 85% at a CO conversion of 55%.

Chang *et al.* tried to combine the advantages of Au supported on TiO<sub>2</sub>, and of MnO<sub>2</sub> supported Au NPs.<sup>380</sup> Au–TiO<sub>2</sub> is generally known to be a very active catalyst for CO oxidation,<sup>328</sup> but also active for oxidation of hydrogen,<sup>272,381</sup> which results in a low selectivity for CO oxidation in a H<sub>2</sub>-rich gas stream.



**Table 6** Preferential CO oxidation

Catalyst	Support preparation		Au preparation/characteristics			Catalytic reaction conditions		Catalytic activity/stability		
	Synthesis	SSA (m <sup>2</sup> /g)	Method	Au (wt%)	Au NP Ø (nm)	Atmosphere/ T °C	PT	Deactivation (%)	Conversion (%)	RR Ref.
<i>Part 1</i>										
Au/P25	Commercial	56	DP	2.6	3.7	All below: 1% CO, 1% O <sub>2</sub> , 75% H <sub>2</sub> , N <sub>2</sub> /80 °C	All below: 400 °C, 10% O <sub>2</sub> /N <sub>2</sub> , 30 min	19	n.m.	3.96/ All below: 3.2 [288]
Au/TiO <sub>2</sub> (A)	Sol-gel, template: B56	106	DP	2.6	3.1			25	n.m.	3.9/ 2.9
Au/TiO <sub>2</sub> (A)	Sol-gel, template: SDS	160	DP	2.6	3.0			3	n.m.	2.8/ 2.7
Au/Si <sub>x</sub> Ti <sub>1-x</sub> O <sub>2</sub> (1:8) (A)	Sol-gel, template: B56	192	DP	2.7	2.8			23	n.m.	4.6/ 3.6
Au/Si <sub>x</sub> Ti <sub>1-x</sub> O <sub>2</sub> (1:13) (A)	Sol-gel, template: B56	158	DP	2.9	3.5			20	n.m.	7.8/ 6.3
Au/Ti(0.13)-SBA-15	Impregnation	500 ± 75	DP	1	38% 1-2; 62% 3-4	All below: 2.3 CO, 10% O <sub>2</sub> , 10% H <sub>2</sub> , 74.7% He/50 °C	All below: 350 °C, air, 4 h	n.m.	98	n.m. All below: [379]
Au/Ti(0.26)-SBA-15	Impregnation	500 ± 75	DP	1	36% 1-2; 64% 3-4			n.m.	99	n.m.
Au/Ti(0.53)-SBA-15	Impregnation	500 ± 75	DP	1	19% 1-2; 81% 3-4			n.m.	100	n.m.
Au/Ti(1.32)-SBA-15	Impregnation	500 ± 75	DP	1	10% 1-2; 60% 3-4, 30% > 5			n.m.	100	n.m.
Au/Ti(2.6)-SBA-15	Impregnation	500 ± 75	DP	1	40% 3-4, 40% 3-4, 20% > 5			n.m.	12	n.m.
<i>Part 2</i>										
Au/TiO <sub>2</sub>	Impregnation	53	DP	0.55	2.45	All below: 1.33% CO, 1.33% O <sub>2</sub> , 65.33% H <sub>2</sub> , He/80 °C	All below: 180 °C, air, 4 h	n.m.	80	n.m. All below: [380]
Au/Mn <sub>2</sub> Ti <sub>98</sub>	Impregnation	51	DP	0.57	3.01			n.m.	27	56.1 n.m.
Au/Mn <sub>2</sub> Ti <sub>98</sub>	Impregnation	50	DP	0.58	2.37			n.m.	98.4	51.3 n.m.
Au/Mn <sub>2</sub> Ti <sub>98</sub>	Impregnation	51	DP	0.58	2.45			n.m.	96.5	48.5 n.m.
Au/Mn <sub>4</sub> Ti <sub>96</sub>	Impregnation	50	DP	0.64	2.35			n.m.	52	62 n.m.
Au/Mn <sub>13</sub> Ti <sub>87</sub>	Impregnation	46	DP	0.69	2.63			n.m.	80	62 n.m.
<i>Part 2</i>										
Au/HMS	One pot synthesis	685	DP	2.24	6.3	All below: 0.5% CO, 1% O <sub>2</sub> , 50% H <sub>2</sub> , 48.5% N <sub>2</sub> /T <sub>50</sub> /selectivity at 375 °C	All below: TGA analysis for coke formation: all catalysts stable	All below: TGA 316	35	1.4 All below: [383]
Au/HMS-Ti	Neutral S <sup>0</sup> templating	758	DP	3.02	5.2			analysis for coke formation: all catalysts stable	116	2.4
Au/HMS-Ce	Neutral S <sup>0</sup> templating	596	DP	3.44	7.4				103	2.5
Au/HMS-Fe	Neutral S <sup>0</sup> templating	807	DP	2.84	4.6				81	9.3
<i>Part 2</i>										
Au/2.5TiSi_M1	2 different methods for details see publication	n.m.	Hydrosol Au (6.5 nm Au NPs, 2.4 tannin/citrate)	n.m.	7.9 ± 2.0	All below: 1% CO, 1% O <sub>2</sub> , 67% H <sub>2</sub> , He/T <sub>25</sub> /selectivity at 80 °C	All below: 400-450 °C	n.m.	97	n.m. All below: [384]
Au/5TiSi_M1		n.m.		2.4	8.5 ± 2.8			n.m.	89	52 n.m.
Au/4TiSi_M2		n.m.		1.9	6.6 ± 2.0			n.m.	56	Below 40
Au/4TiSi_M4		n.m.		1.8	6.9 ± 1.5			n.m.	83	40 n.m.
Au/Ti		n.m.		2.3	13.0 ± 5.6			n.m.	89	4 n.m.
Au/1FeO <sub>x</sub> -99TiO <sub>2</sub>	Impregnation	n.m.	DP	0.8	n.m.	All below: 1.33% CO, 1.33% O <sub>2</sub> , 65.33%	All below: 180 °C, air, 4 h	n.m.	90	n.m. All below: [387]
Au/5FeO <sub>x</sub> -95TiO <sub>2</sub>	Impregnation	n.m.	DP	0.75	n.m.			n.m.	95	40-50 n.m.
Au/10FeO <sub>x</sub> -90TiO <sub>2</sub>	Impregnation	n.m.	DP	0.71	n.m.			n.m.	95	40-50 n.m.

Table 6 (continued)

Catalyst	Support preparation		Au preparation/characteristics		Catalytic reaction conditions		Catalytic activity/stability		
	Synthesis	SSA (m <sup>2</sup> /g)	Method	Au (wt%), Au NP Ø (nm)	Atmosphere/ T/°C	PT	Deactivation (%)	Conversion (%)	RR Ref.
Au/20FeO <sub>x</sub> -80TiO <sub>2</sub>	Impregnation	n.m.	DP	0.76 n.m.	H <sub>2</sub>		n.m.	88	n.m.
Au/FeO <sub>x</sub>	Impregnation	n.m.	DP	0.73 n.m.	He/80 °C		n.m.	88	n.m.
Au/TiO <sub>2</sub>	Impregnation	n.m.	DP	0.74 n.m.			n.m.	88	n.m.
Au/TiO <sub>2</sub>	Commercial	127	DP	1.4 2.5 ± 1.0	All below: 1% CO, 1% O <sub>2</sub> , 70% H <sub>2</sub> , He/80 °C	All below: 150 °C, 5% H <sub>2</sub> /Ar, 30 min	n.m.	30	n.m. All below: [388]
Au/Co <sub>3</sub> O <sub>4</sub> -CeO <sub>2</sub>	Co-precipitation (1:1)	48	DP	1.4 2.9 ± 1.0			n.m.	78	n.m.
Au/CeO <sub>2</sub>	Commercial	52	DP	1.4 2.9 ± 1.2			n.m.	72	n.m.
Au/Co <sub>3</sub> O <sub>4</sub>	Commercial	39	DP	1.3 n.m.			n.m.	35	n.m.
Au/γ-Al <sub>2</sub> O <sub>3</sub>	Commercial	160	DP	1.1 3.5 ± 2.1			n.m.	40	n.m.

A, anatase; R, rutile; B, brookite; HT, hydrothermal; SSA, specific surface area; IE, ionic exchange; DP, deposition-precipitation method; CD, colloidal deposition method; n.m., not mentioned; PT, pre-treatment; RR, reaction rate (mol<sub>CO</sub> g<sub>Au</sub><sup>-1</sup> s<sup>-1</sup> × 10<sup>4</sup>) either initial or initial/final after 1000 min on stream.

On the other hand, MnO<sub>2</sub> supported Au catalyst were found to exhibit a high selectivity for CO oxidation in H<sub>2</sub>-rich gas streams, but at a rather poor activity.<sup>7,382</sup> Therefore they prepared MnO<sub>2</sub>-TiO<sub>2</sub> materials with various compositions by incipient wetness impregnation, followed by Au deposition *via* a DP method (specific surface area ~ 50 m<sup>2</sup> g<sup>-1</sup>, mean Au NP size 2.2–4 nm, gold loading 0.55–0.69 wt%). They studied the effect of the pH during Au loading and of the Mn:Ti ratio of the catalyst support, finding the most efficient catalyst to be the Au-Mn<sub>2</sub>Ti<sub>98</sub> catalysts prepared at pH 6 and 9, respectively, with CO conversions above 96% and selectivities above 48% (1.33% CO, 1.33% O<sub>2</sub>, 65.33% H<sub>2</sub>, balance He). Apparently, the addition of MnO<sub>2</sub> on a Au-TiO<sub>2</sub> catalyst indeed improved the selectivity for CO oxidation, without sacrificing too much on the CO conversion under these conditions. This was tentatively explained by an 'optimum combination of metallic and electron-deficient gold on the catalyst surface', a deeper understanding, however, is still missing.

Recently, Zepeda *et al.* explored the performance of Au catalysts supported on hexagonal mesoporous silica (HMS) modified with Fe<sup>2+</sup>, Ce<sup>4+</sup> and Ti<sup>4+</sup> in the PROX reaction.<sup>383</sup> Au loading was performed *via* a DP procedure (2.0–3.4 wt% Au loading, mean Au NP size 4.6–7.4 nm). The catalytic performance was determined in conversion measurements in a H<sub>2</sub>-rich feed stream (50% H<sub>2</sub>, 1% O<sub>2</sub>, 0.5% CO, N<sub>2</sub>, temperature 20–400 °C) after *in situ* pre-treatment with H<sub>2</sub> at 300 °C for 2 h. The activity (*T*<sub>50</sub> °C) and selectivity for CO oxidation determined at 375 °C followed the trend: Au-HMS-Fe (81 °C, 63%) > Au-HMS-Ti (116 °C, 54%) ≈ Au-HMS-Ce (103 °C, 48%) > Au-HMS (316 °C, 35%). The activities are clearly well below those of other catalysts, while the selectivities seem to be in the normal range. Here it has to be considered, however, that they were determined at an extremely high temperature, well above the operation temperature of 'normal' Au catalysts, which normally leads to a loss of selectivity.<sup>282,378</sup> Finally, the long term stability in the CO oxidation reaction was tested at 160 °C for 800 min, yielding values of between 5% and 30% for the deactivation. Considering that this was determined in the absence of H<sub>2</sub>, and on the other hand the high temperature, the values are somewhat lower than reported recently for a Au/P25 catalyst at 180 °C (28% deactivation over 1000 min).<sup>378</sup>

Beck *et al.* investigated the catalytic behavior of Au catalysts consisting of Au NPs and titania or of Au oxides deposited on either amorphous silica or mesoporous SBA-15 in the PROX reaction.<sup>384</sup> Au colloids (around 2 wt%) and titania in various amounts (2.5–20 wt%) were deposited on the silica substrates by three different methods (denoted by M1–M3) to obtain the Au-*x*TiSi catalysts, where *x* denotes the TiO<sub>2</sub> content in wt%. (For details of the deposition process, see ref. 384.) Since the sizes of the Au NPs lie in the same range of about 6.6–7.9 nm and above 5 nm, the influence of the Au NPs size on the activity will be small.<sup>385,386</sup> For comparison, a Au/P25 catalyst was included as well (2.3 wt% Au, 5.3 mean particle size). The PROX activity was evaluated in conversion measurements after calcination of the catalysts at 400–450 °C. It followed the order: Au/P25 (50 °C) > Au-4TiSi\_M2 (56 °C) > Au-4TiSi\_M3 (83 °C) ~ Au-Ti = Au-5TiSi\_M1 (89 °C) > Au-2.5TiSi (97 °C), while the selectivity in the range of 50 and 80 °C

decreased in order: Au–2.5TiSi (above 60%) > Au–5TiSi\_M1 (~52%) > Au–4TiSi\_M3 (~40%) > Au/P25 (~40%) > Au–4TiSi\_M2 (below 40%). Samples having a higher amount of titania than 5 wt% were not active for the PROX. Obviously, the activity of Au/P25 sample is not comparable with the usual activity of nonporous Au/P25, which may be due to the relatively large Au NP size in that catalyst.<sup>384</sup> This hinders also a quantitative comparison for the other catalysts, at least for the CO oxidation activity. The selectivities, on the other hand, look rather similar to those generally reported for Au/P25 for comparable reaction conditions. As for the mechanistic understanding of these finding, the authors underlined the importance of the length of active perimeter of the Au–TiO<sub>2</sub> interface and of the interface between Au and the inert oxide (SiO<sub>2</sub>). The latter was proposed to be important for the H<sub>2</sub> oxidation reaction.

A comparable series of measurements was performed by Yang *et al.*, who studied the effect of Fe<sub>2</sub>O<sub>3</sub> modification of the TiO<sub>2</sub> support on the PROX reaction characteristics of the resulting Au–FeO<sub>x</sub>–TiO<sub>2</sub> catalysts.<sup>387</sup> For these measurements, they prepared a series of Au catalysts (Au loading around 0.8 wt%) based on FeO<sub>x</sub>–TiO<sub>2</sub> supports, which were prepared *via* incipient wetness impregnation. Gold deposition was performed *via* DP. In addition, a Au/P25 catalyst was evaluated as well. Based on conversion measurements in a PROX reaction mixture (1% CO, 1% O<sub>2</sub>, 49% H<sub>2</sub>, 49% He), the highest activity was reached for the Au catalyst supported on FeO<sub>x</sub>–TiO<sub>2</sub> with a ratio 1:99, at least at lower temperatures ( $\leq 50$  °C). The selectivity was found to decrease with increasing *T* for all catalysts, the highest selectivity of ~90% was reached over the Au–FeO<sub>x</sub>–TiO<sub>2</sub> catalyst with a ratio of 10:90 at 20 °C, though the differences between the different catalysts are small. For reaction at 80 °C, the selectivities were comparable for all samples. The authors proposed that the addition of amorphous Fe<sub>2</sub>O<sub>3</sub> enhances the CO conversion and suppresses the oxidation of H<sub>2</sub> *via* an enhanced electronic interaction and better stabilization of the Au NPs. Except for the low temperature ( $\leq 50$  °C) CO conversion, the effects, however, are rather small, in particular with respect to the selectivity.

Liotta *et al.* compared the performance of several Au catalysts with different reducible support materials (TiO<sub>2</sub>, Co<sub>3</sub>O<sub>4</sub>–CeO<sub>2</sub>, CeO<sub>2</sub>, Co<sub>3</sub>O<sub>4</sub>) and for comparison Au supported on non-reducible Al<sub>2</sub>O<sub>3</sub> in the selective CO oxidation.<sup>388</sup> The catalysts were prepared by a DP procedure and a reductive pre-treatment in 5% H<sub>2</sub> in Ar (150 °C, 30 min) prior to the reaction (mean Au particle sizes 2.5–3.5 nm, Au loading 1.1–1.4 wt%). Comparing the activity and selectivity at 80 °C, these decreased in the order: Au–Co<sub>3</sub>O<sub>4</sub>–CeO<sub>2</sub>  $\approx$  Au–CeO<sub>2</sub> > Au–Co<sub>3</sub>O<sub>4</sub>  $\approx$  Au/Al<sub>2</sub>O<sub>3</sub>  $\approx$  Au–TiO<sub>2</sub> and Au–Co<sub>3</sub>O<sub>4</sub>–CeO<sub>2</sub>  $\approx$  Au–CeO<sub>2</sub>  $\approx$  Au–Co<sub>3</sub>O<sub>4</sub> > Au/Al<sub>2</sub>O<sub>3</sub>  $\approx$  Au–TiO<sub>2</sub>, respectively. While Au–TiO<sub>2</sub> is the most active catalyst in CO oxidation, its high activity for the competing H<sub>2</sub> oxidation in the PROX affects the CO oxidation by an increasing lack of oxygen (1% CO, 70% H<sub>2</sub>, 1% O<sub>2</sub>, balance He). The authors attributed the high activity of the Au–TiO<sub>2</sub> catalyst for H<sub>2</sub> oxidation to a large population of highly dispersed and low coordinated Au atoms, which can activate O<sub>2</sub> to subsequently react with either CO or H<sub>2</sub> at lower temperature and predominantly with H<sub>2</sub> at higher temperatures. The high activity and selectivity of Co<sub>3</sub>O<sub>4</sub>–CeO<sub>2</sub>,

CeO<sub>2</sub>, Co<sub>3</sub>O<sub>4</sub> supported catalyst in the PROX reaction, on the other hand, they explained by a high formation of oxygen vacancies (high reducibility of the support), which they claim would activate the oxidation of CO. In the absence of hard experimental support for these concepts, however, the mechanistic understanding of these reactions is not yet solved.

In total, the findings for the PROX reaction very much resemble those reviewed in Section 3 for the CO oxidation reaction, although the data base is smaller than for CO oxidation. So far, the move to high surface area TiO<sub>2</sub> supports and related materials gave some promising results, but the overall improvement compared to standard non-porous Au/P25 catalysts is still small. It should be noted that the situation is different in the PROX reaction in that under PROX reaction conditions the main problem is not the long-term stability, but the selectivity, in particular at lower CO contents. Based on the above data, improvements in the selectivity seem to be more within reach than for the long-term stability in the CO oxidation in a H<sub>2</sub>-free atmosphere.

## 5.5 Deactivation

As mentioned before, deactivation is a major if not the dominant problem of supported Au catalysts, at least in many reactions. In general, catalyst deactivation can be caused by three main reasons, and this is true also for the deactivation of high surface area TiO<sub>2</sub> supported Au catalysts and related Au catalysts with time on stream. These are (i) growth of the active phase nanoparticles, *e.g.*, by Ostwald ripening or agglomeration, (ii) poisoning of the catalytically active sites by adsorption of catalyst poisons from the reaction gas mixture or by segregation from the catalyst bulk, and (iii) poisoning by accumulation of adsorbed side products or reaction intermediates. Examples typical for deactivation of supported Au catalysts would be (i) Au particle growth, (ii) catalyst poisoning by mobile residues from the support or catalyst preparation such as Cl or S, or (iii) accumulation of reaction side products such as surface carbonates or carboxylates on the catalyst surface, which may cause *e.g.*, blocking of active sites at the perimeter of the interface between support and Au NP. Furthermore, modifications of the surface chemistry by adsorption or desorption of surface groups may play a role as well. Typical example in Au catalysis would be the formation/depletion of surface hydroxyl groups and/or water formation or the reduction (O vacancy formation)/oxidation (replenishment of O vacancies) on the support surface.<sup>272</sup>

Deactivation of Au NPs by aggregation or a combination of aggregation and Ostwald ripening would lead to an increase of the Au NP size, and, in consequence, to a decrease of the active surface area (or of the length of the interface perimeter per g of catalyst), which in turn would lead to loss of activity. Both processes, however, require relatively high temperatures, estimated  $0.4 \times$  melting point ( $T_m(\text{Au}) = 1068$  °C), which would mean ~430 °C for Au. This is on the scale of typical pre-treatment procedures, *e.g.*, calcination at 400 °C, which indeed often lead to Au NP growth and result in mean particle sizes of 2.5–3 nm. Since most of described reactions did not exceed reaction temperatures of 300 °C, and mostly they were below 100 °C, Au particle growth can essentially be excluded



as a major contribution to the deactivation of Au catalysts. This was confirmed in numerous TEM measurements, which found no significant Au NP growth during the reaction, *e.g.*, for CO oxidation or PROX reaction on Au/P25 catalysts at 80 or 180 °C.<sup>378</sup>

Poisoning of Au catalysts by adsorption of reaction inhibiting species from the gas phase, by segregation of such species from the catalyst bulk or by decomposition of surface species was experienced, *e.g.*, in cases where S containing species were used during catalyst preparation. A typical example is the use of thiols as a capping agent for the preparation of Au NPs.<sup>333,354</sup> The authors reported that the catalysts had to be activated, by oxidation of thiols to SO<sub>x</sub>, to be active for CO oxidation. The effect of SO<sub>2</sub> on the activity of Au–TiO<sub>2</sub> was studied also by Ruth *et al.*, who found that the presence of SO<sub>2</sub> rapidly poisoned the Au–TiO<sub>2</sub> catalyst.<sup>389</sup> Comparable effects can be caused by the presence of Cl, which may be present as trace impurity from the catalyst preparation process, due to insufficient washing.

Predominant reason for the deactivation of Au catalysts, including high surface area TiO<sub>2</sub> supported Au catalysts, is to our belief the accumulation of stable, adsorbed reaction side products on the catalyst surface, which among others will block catalytically active surface sites. The unanimous identification of adsorbed species as site blocking catalyst poison, however, is complex. In the absence of direct evidence, which is mostly the case, it requires a quantitative correlation between increasing coverage of these species, possibly on specific sites, and decline in activity. Only if this can be proven during dynamic variation of the surface composition, the respective surface species are safely identified as surface poison. In other cases, they may act as spectator species, which are present on the surface, but have little effect on the activity.

*In situ* spectroscopy measurements, *e.g.*, *in situ* IR spectroscopy, can clearly characterize the state of the catalyst surface before and during the CO oxidation reaction. It has been demonstrated that surface carbonates and related species such as monodentate carbonates, bidentate carbonates, bicarbonates, formates, carboxyls, *etc.* can be formed during the CO oxidation reaction, and it has been suspected that these species poison the perimeter sites, where activation of O<sub>2</sub> takes place.<sup>288,289,390</sup> Although this appears very plausible, unanimous evidence therefore, however, is still rare or missing.

Ntho *et al.* monitored the region of carbonate vibrations during CO oxidation on mesoporous titania nanotube supported Au catalysts by *in situ* diffuse reflection IR Fourier transform spectroscopy (DRIFTS) measurements.<sup>391</sup> They observed the formation of a band at 1290 cm<sup>-1</sup>, which was considered to be typical for adsorbed bicarbonate species. Based on a qualitative correlation with the decreasing activity they proposed that the formation of this stable species is responsible for the pronounced catalyst deactivation (95% after 22 h on stream). The stability of this species was determined by temperature programmed desorption (TPD) measurements, which implied that decomposition of this species occurs at ~150 °C, resulting in a CO<sub>2</sub> desorption peak. They also tried to investigate the influence of water on the deactivation, by addition of ~1 µl water during the reaction. The presence of water inhibited the formation of this bicarbonate species, as evident from both DRIFTS and TPD. Most probably, the presence of water has two effects: it promotes

the CO oxidation reaction and reduces the deactivation, a phenomenon which is commonly observed for the PROX reaction.<sup>288</sup>

Wang *et al.* obtained a very low deactivation for CO reaction over mesoporous Au–MCT–Ti catalysts at 24 °C of only about 10% during 24 h on stream.<sup>325</sup> Considering the stability of supported Au NPs described above, this low deactivation must be due to a very low tendency for adsorbed carbon containing side products such as surface carbonates, *etc.* On the other hand, they found that the Au NPs on these extremely stable. Even after per-treatment at 500 °C, the size of the Au NPs is still very small, contrary to the observations over Au/P25, where the particles grew to 5–30 nm. This indicates a support specific stabilization of Au NPs.

In our reaction studies on mesoporous TiO<sub>2</sub> or mixed oxide supported Au catalysts,<sup>5,343,349</sup> we found the same characteristic features in *in situ* DRIFTS measurements as in similar measurements on nonporous Au/P25 catalysts, and also the evolution of the intensities with time on stream was comparable in nature.<sup>288</sup> This lead us to the conclusion that similar to the proposal for Au/P25,<sup>288</sup> the deactivation is likely to be caused by stable adsorbed reaction side products such as surface carbonates and/or carboxylates, which accumulate on the catalyst surface during the CO oxidation reaction. Differences existed, however, in the relative intensities of these species. Comparing non-porous and mesoporous Au catalysts, the accumulation of carbonate species on mesoporous Au–TiO<sub>2</sub> or mixed oxide supported catalysts are much lower in intensity, indicative of lower coverages. The data base, however, is not sufficient to unambiguously identify specific adspecies as dominant catalyst poison, *i.e.*, as being mainly responsible for the observed catalyst deactivation. Monodentate surface carbonates, which had been proposed by Schumacher *et al.* as the main cause for the deactivation of Au/P25 catalysts during CO oxidation under similar reaction conditions,<sup>288</sup> are possible candidates also for the present catalysts, but contributions from other adsorbed carbonate and carboxylate species cannot be excluded either.

Reversible deactivation was reported also by Zhu *et al.*, who found that after regenerating their used SiO<sub>2</sub> decorated Au–TiO<sub>2</sub> catalysts by calcination in O<sub>2</sub>–He at 400 °C for 1 h, the catalysts showed the same reactivity as the fresh catalysts.<sup>369</sup> This means that the deactivation was not irreversible, as would be expected for Au NP growth, and most likely caused by accumulation of stable adsorbed reaction side products or intermediate species.

Moreau *et al.* tested the long term stability of Au catalysts supported on mesoporous CeO<sub>2</sub> modified with La or Fe or on mesoporous CeZrO<sub>4</sub>.<sup>392</sup> While the Au–CeO<sub>2</sub> deactivated slowly, but steadily over 50 h, the Au–La–CeO<sub>2</sub> or Au–Fe–CeO<sub>2</sub> catalysts showed a constant activity. For Au–CeZrO<sub>4</sub>, the activity passed through an initial maximum, and then remained almost constant. DRIFTS measurements showed that on all catalysts surface carbonate species were formed, as indicated by bands in the range 1000–1600 cm<sup>-1</sup>. The intensity decreased in the order Au–CeO<sub>2</sub> > Au–La–CeO<sub>2</sub> ≈ Au–CeZrO<sub>4</sub> > Au–Fe–CeO<sub>2</sub>, which reflects approximately, but not exactly the deactivation behavior. Furthermore, it was found that using catalysts dried in He at room temperature, the amount of carbonate formation decreased with longer drying periods.

The authors concluded that stable activity is associated with retention of surface OH groups and lesser formation of carbonate/bicarbonate species during reaction. The improved stability upon modification of the support with Fe and La was tentatively attributed a greater acidity of the hydroxyl groups on these catalysts, which would reduce the tendency for surface carbonate formation.

The situation is different in H<sub>2</sub>-rich reaction atmospheres, as encountered, *e.g.*, in the PROX reaction. Under these conditions, the deactivation of the catalysts is significantly lower. First of all, based on numerous TEM analyses before and after reaction, we can exclude also under these reaction conditions growth of Au NPs as a major reason for deactivation.<sup>349,378</sup> Based on *in situ* DRIFT spectra recorded during PROX reaction on mesoporous TiO<sub>2</sub> and mesoporous mixed oxide supported Au catalysts, the situation is rather similar to that during reaction in a H<sub>2</sub>-free atmosphere, if focusing on the nature of the different adsorbed carbon containing species being formed during reaction. Differences exist, however, in the peak intensities in the carbonate region and in the very intense water peak at  $\sim 1620\text{ cm}^{-1}$ . As it was proposed by Schumacher *et al.*,<sup>288</sup> the presence of H<sub>2</sub> largely inhibits the formation of carbonate species that develop in much higher quantities in H<sub>2</sub>-free reaction mixtures, and were held responsible for catalyst deactivation.<sup>7,288,289,318,393</sup>

These ideas were confirmed later by *operando* DRIFTS measurements on a Au–TiO<sub>2</sub> catalyst (World Gold Council<sup>365</sup>) by Piccolo *et al.*<sup>394</sup> From elegant switch experiments, removing or adding individual components from the reaction gas mixture (CO, H<sub>2</sub>, O<sub>2</sub>), they concluded that in the presence of higher amounts of H<sub>2</sub>, the formation of surface carbonate species, which is dominant in the absence of H<sub>2</sub>, is inhibited, together with pronounced accumulation of adsorbed water and formation of hydroxyl groups.

Zepeda *et al.* tested the stability of Au catalysts supported on hexagonal mesoporous silica (HMS) modified by Fe<sup>3+</sup>, Ce<sup>4+</sup> or Ti<sup>4+</sup>.<sup>383</sup> The catalyst stability was evaluated in long-term (800 min) CO oxidation runs at 160 °C. The amount of surface carbonates and related species formed during the reaction was determined by measuring the amount of CO<sub>2</sub> formation and the weight loss upon decomposition of these species by temperature programmed oxidation (TPO) and thermogravimetric analysis (TGA). The activity measurements and the TPO/TGA measurements at the end of the reaction indicated that the modification of the Au/HMS catalyst reduced both the deactivation and the tendency for the formation of surface carbonates and related species. Also this result points to a dominant role of these surface species for catalyst deactivation.

### 5.6 Concluding remarks on the catalysis with TiO<sub>2</sub>

The preceding discussion has shown that high surface area TiO<sub>2</sub> and related materials are promising candidates as support material for highly active, and, even more important, long-term stable Au catalysts. Using Au/P25 as a reference catalyst, significantly improved stabilization of Au NPs against thermally induced particle growth, either by Ostwald ripening or by agglomeration of NPs, has been demonstrated

in a number of cases. Activities reaching or even slightly exceeding that of the reference catalyst have also been achieved. Also selectivities for CO oxidation in the PROX reaction, which are comparable or even in excess of that of the reference catalyst, have been reported. Most critical for applications is the long-term stability, which for oxide supported Au catalysts and for the present reactions, seems to be mainly limited by the adsorption of stable, adsorbed reaction side products rather than by Au NP growth, at least under normal reaction conditions. Catalyst deactivation, which is the weak point for technical applications of Au catalysis, is also limiting for the present class of high surface area catalysts discussed in this section. On the one hand, support materials which lead to high long-term stabilities should not lose the high activity of the reference catalyst. This latter demand has not yet met by any of the ‘new’ support materials discussed here. On the other hand, there is significant progress in specific catalyst properties, which leaves the further search for improved support materials for Au catalysts promising and open.

From a scientific point of view, aiming at a detailed understanding of the reaction, and the mechanisms being responsible for the high activity and for the deactivation, the main problem seems to be on the experimental side. In general, understanding and interpretation suffer from the fact that in almost all systematic studies several parameters are changed simultaneously. In addition to the support material, also Au loading and Au particle sizes are changed. This of course reflects the problems encountered in materials synthesis and catalyst preparation. Nevertheless, there are ways to separate these aspects, *e.g.*, by colloidal deposition. In this context also the reproducibility in materials synthesis and catalyst preparation has to be addressed, which also has potential for improvement. Finally, the reaction conditions in the catalytic measurements vary tremendously between different studies, and it is hardly possible to compare results on a quantitative scale. This also includes differences in the activation pre-treatment of the catalysts. Overall, a detailed mechanistic understanding of the reactions, as it would be desirable for a systematic search strategy on the materials side, requires significant improvements in these areas. This will be the main task of the coming years.

## 6. Conclusion and outlook

In this critical review, novel aspects and recent developments in the synthesis of crystalline titania nanostructures as well as their application have been reviewed. From the many possible applications, the focus in this article was given to titania in energy storage systems, such as lithium ion batteries, or as catalyst support in the Au-catalyzed CO oxidation reaction. For both processes, the Li diffusion into the titania network as well as the deposition and catalytic performance of the Au nanoparticles on the titanium oxide surface, the clear demand for crystalline nanoscale structures with well-accessible surfaces/interfaces is given. Therefore, there is still a large need for novel, simple and cheap preparative methods towards crystalline titania polymorphs with well-defined nanostructures, porosity, interface and surface areas.

Many approaches towards nanoscale materials are based on processes in solution, with the sol–gel or related procedures as

the most prominent ones to discuss. The formation of titania *via* these processes has been described in numerous publications over the last hundred years. However, titania is a metal oxide with a rather high temperature of crystallization, thus crystallinity of the material directly from the synthesis process is often poor and it is very difficult to deliberately control the formation of the different relevant polymorphs (rutile/anatase). In addition, postsynthetic heat treatment to increase crystallinity of the material may adversely affect the nanoscale properties, often resulting in sintering and particle growth and thus, in reduced surface and interface areas. Novel synthesis procedures – based on advanced techniques, such as hydrothermal processing, microwave heating, sonochemistry, mini/microemulsion processing, or novel precursor systems – gave access to crystalline titania nanostructures with higher surface areas, deliberately tailored morphology and the desired polymorph. In addition, some of these protocols are based on purely aqueous solutions, therefore not leaving environmental aspects out of sight. Despite all the research effort, it is for many of the synthesis procedures still very difficult to predict the final product properties based on the knowledge present today. Nevertheless, the wealth of reaction parameters, precursors and techniques that have been applied and that still can be investigated is almost endless and despite the many studies that have attempted to correlate chemical structure and formation process, it is still ambiguous and leaves much room for more research.

We have shown that titanium dioxide (anatase) is an attractive candidate as electrode (anode) material in lithium ion batteries, due to its fast lithium ion insertion–extraction reactions, the high insertion capacity in combination with high abundance and stability, non-toxicity and low cost. In addition, only recently it was found that nanoscale rutile as well shows a high potential as anode material. With respect to the electrochemical performance, a deliberate control of the morphological and compositional properties of titania (anatase, rutile, TiO<sub>2</sub> (B)) is indispensable. Decreasing the particle size to the nanoscale dimensions, incorporating mesopores and thus, increasing the surface area, shows a dramatic positive effect on the electrochemical behavior for anatase, but also rutile. Future generations of rechargeable lithium ion batteries with the demand for higher energy and higher power will more and more depend on the application of nanomaterials as electrodes, as well as electrolytes, thus increasing the amount of interfaces for an efficient lithium ion and electron transport significantly. The authors are convinced that the development of novel methods in synthesis and electrochemistry will be of major impact in this area in the future. The same is true for the characterization of the materials. Many studies have been performed on model systems, nevertheless, the data are to some extent contradictory and there is major need for more sophisticated *in situ* and *ex situ* characterization techniques.

Equally attractive are nanostructured, high surface area titanium dioxide and related materials for catalytic applications, in particular as support material in heterogeneous catalysis, photocatalysis and electrocatalysis. This was elucidated using the CO oxidation reaction catalyzed by Au NPs on TiO<sub>2</sub> as example. Also here, the existing data clearly demonstrate the

complexity of both the reaction and the research. Structure, physical and chemical properties of the supporting material will play a role in the formation of Au NPs, their morphology and especially the type of contact between the support and the Au nanoparticle. Since one of the possible explanations for activity is the number of low coordinated sites, also the shape of the resulting Au NPs may be important. Furthermore, these may directly influence also the catalytic reaction. The contact Au–support and the nature of the accessible perimeter sites along the interface are expected to be essential for the transfer of oxygen species. A main problem to be solved for technical applications is to lower the deactivation of the Au catalysts while maintaining their high activity. Also here, novel synthesis methods, allowing for controlled modification of specific catalyst properties, while maintaining their other properties, will be a key for the systematic improvement of these catalysts, based on a microscopic understanding of their function.

Titania nanostructures with high surface area are attractive materials and ideal candidates for manifold applications. The versatility and feasibility of these materials have been demonstrated in this review article and there is still more to come. Nevertheless, it is the opinion of the authors that much more research effort has to be devoted to systematic studies of synthesis–structure–properties relationships that are relevant for the specific applications.

## Acknowledgements

This work was supported by the Deutsche Forschungsgemeinschaft within the Priority Programme 1181 “Nanomaterials” (Be 1201/13, Hu 1427/1, KA 1295/5, LA 1013/7, WO 882/2). Financial support from BMBF in the framework of the LISA project (03SF0327A) is gratefully acknowledged.

## References

- 1 B. M. Reddy and A. Khan, *Catal. Rev. Sci. Eng.*, 2005, **47**, 257–296.
- 2 Z. Zhang, C.-C. Wang, R. Zakaria and J. Y. Ying, *J. Phys. Chem. B*, 1998, **102**, 10871–10878.
- 3 K. Fukushima and I. Yamada, *J. Appl. Phys.*, 1989, **65**, 619–623.
- 4 W. P. Hsu, R. Yu and E. Matijevic, *J. Colloid Interface Sci.*, 1993, **156**, 56–65.
- 5 J. Geserick, T. Froeschl, N. Huesing, G. Kucerova, M. Makosch, T. Diemant, S. Eckle and R. J. Behm, *Dalton Trans.*, 2011, **40**, 3269–3286.
- 6 M. Haruta, T. Kobayashi, H. Sano and N. Yamada, *Chem. Lett.*, 1987, 405–408.
- 7 M. M. Schubert, V. Plzak, J. Garche and R. J. Behm, *Catal. Lett.*, 2001, **76**, 143.
- 8 N. G. Park, J. van de Lagemaat and A. J. Frank, *J. Phys. Chem. B*, 2000, **104**, 8989–8994.
- 9 L. Kavan, M. Graetzel, J. Rathousky and A. Zukal, *J. Electrochem. Soc.*, 1996, **143**, 394–400.
- 10 P. Kubiak, T. Froeschl, N. Huesing, U. Hoermann, U. Kaiser, R. Schiller, C. K. Weiss, K. Landfester and M. Wohlfahrt-Mehrens, *Small*, 2011, **7**, 1690–1696.
- 11 L. Kavan, *Chem. Rec.*, 2012, **12**, 131–142.
- 12 B. L. Cushing, V. L. Kolesnichenko and C. J. O'Connor, *Chem. Rev.*, 2004, **104**, 3893–3946.
- 13 X. Chen and S. S. Mao, *Chem. Rev.*, 2007, **107**, 2891–2959.
- 14 F. J. Heiligtag, M. D. Rossell, M. J. Suess and M. Niederberger, *J. Mater. Chem.*, 2011, **21**, 16893–16899.
- 15 G. Frenzer and W. F. Maier, *Annual Review of Materials Research*, 2006, vol. 36, pp. 281–331.



- 16 C. Z. Yu, B. Z. Tian and D. Y. Zhao, *Curr. Opin. Solid State Mater. Sci.*, 2003, **7**, 191–197.
- 17 B. Mandlmeier, J. M. Szeifert, D. Fattakhova-Rohlfing, H. Amenitsch and T. Bein, *J. Am. Chem. Soc.*, 2011, **133**, 17274–17282.
- 18 K. Kabra, R. Chaudhary and R. L. Sawhney, *Ind. Eng. Chem. Res.*, 2004, **43**, 7683–7696.
- 19 H. Zhang and J. F. Banfield, *J. Mater. Chem.*, 1998, **8**, 2073–2076.
- 20 R. Marchand, L. Brohan and M. Tournoux, *Mater. Res. Bull.*, 1980, **15**, 1129–1133.
- 21 M. Latroche, L. Brohan, R. Marchand and M. Tournoux, *J. Solid State Chem.*, 1989, **81**, 78–82.
- 22 J. Akimoto, Y. Gotoh, Y. Oosawa, N. Nonose, T. Kumagai, K. Aoki and H. Takei, *J. Solid State Chem.*, 1994, **113**, 27–36.
- 23 J. F. Banfield, D. R. Veblen and D. J. Smith, *Am. Mineral.*, 1991, **76**, 343–353.
- 24 V. Stengl and D. Králová, *Mater. Chem. Phys.*, 2011, **129**, 794–801.
- 25 M. Inada, K. Iwamoto, N. Enomoto and J. Hojo, *J. Ceram. Soc. Jpn.*, 2011, **119**, 451–455.
- 26 C.-E. Liu, A. Rouet, H. Sutrisno, E. Puzenat, H. Terrisse, L. Brohan and M. Richard-Plouet, *Chem. Mater.*, 2008, **20**, 4739–4748.
- 27 Y. Morishinia, M. Kobayashi, V. Petrykin, M. Kakihana and K. Tomita, *J. Ceram. Soc. Jpn.*, 2007, **115**, 826–830.
- 28 J.-P. Jolivet, *Metal Oxide Chemistry and Synthesis: From Solution to Solid State*, 2000.
- 29 C.-S. Fang and Y.-W. Chen, *Mater. Chem. Phys.*, 2003, **78**, 739–745.
- 30 H. K. Park, D. K. Kim and C. H. Kim, *J. Am. Ceram. Soc.*, 1997, **80**, 743–749.
- 31 S. Cassaignon, M. Koelsch and J. P. Jolivet, *J. Phys. Chem. Solids*, 2007, **68**, 695–700.
- 32 M. Pflanzelt, P. Kubiak, M. Fleischhammer and M. Wohlfahrt-Mehrens, *J. Power Sources*, 2011, **196**, 6815–6821.
- 33 J. Yang and J. M. F. Ferreira, *Mater. Res. Bull.*, 1998, **33**, 389–394.
- 34 S. D. Sharma, D. Singh, K. K. Saini, C. Kant, V. Sharma, S. C. Jain and C. P. Sharma, *Appl. Catal., A*, 2006, **314**, 40–46.
- 35 N. Smirnova, A. Eremenko, V. Gayvoronskij, I. Petrik, Y. Gnatyuk, G. Krylova, A. Korchev and A. Chuiko, *J. Sol-Gel Sci. Technol.*, 2004, **32**, 357–362.
- 36 Y. Takahashi and Y. Matsuoka, *J. Mater. Sci.*, 1988, **23**, 2259–2266.
- 37 A. Pottier, C. Chaneac, E. Tronc, L. Mazerolles and J. P. Jolivet, *J. Mater. Chem.*, 2001, **11**, 1116–1121.
- 38 R. Rossmanith, C. K. Weiss, J. Geserick, N. Hüsing, U. Hörmann, U. Kaiser and K. Landfester, *Chem. Mater.*, 2008, **20**, 5768–5780.
- 39 A. Teleki, S. E. Pratsinis, K. Kalyanasundaram and P. I. Gouma, *Sens. Actuators, B*, 2006, **119**, 683–690.
- 40 G. Skandan, Y. J. Chen, N. Glumac and B. H. Kear, *Nanostruct. Mater.*, 1999, **11**, 149–158.
- 41 A. Matthews, *Am. Mineral.*, 1976, **61**, 419–424.
- 42 M. Wu, G. Lin, D. Chen, G. Wang, D. He, S. Feng and R. Xu, *Chem. Mater.*, 2002, **14**, 1974–1980.
- 43 C.-C. Wang and J. Y. Ying, *Chem. Mater.*, 1999, **11**, 3113–3120.
- 44 H. Cheng, J. Ma, Z. Zhao and L. Qi, *Chem. Mater.*, 1995, **7**, 663–671.
- 45 Y. Oguri, R. E. Riman and H. K. Bowen, *J. Mater. Sci.*, 1988, **23**, 2897–2904.
- 46 J. Ovenstone and K. Yanagisawa, *Chem. Mater.*, 1999, **11**, 2770–2774.
- 47 T. Nagase, T. Ebina, T. Iwasaki, K. Hayashi, Y. Onodera and M. Chatterjee, *Chem. Lett.*, 1999, 911–912.
- 48 M. C. Yan, F. Chen, J. L. Zhang and M. Anpo, *J. Phys. Chem. B*, 2005, **109**, 8673–8678.
- 49 Y. Zheng, K. Lv, Z. Wang, K. Deng and M. Li, *J. Mol. Catal. A: Chem.*, 2012, **356**, 137–143.
- 50 P. Zhang, B. Liu, S. Yin, Y. Wang, V. Petrykin, M. Kakihana and T. Sato, *Mater. Chem. Phys.*, 2009, **116**, 269–272.
- 51 A. Gedanken, *Ultrason. Sonochem.*, 2004, **11**, 47–55.
- 52 H. Arami, M. Mazloumi, R. Khalifehzadeh and S. K. Sadrnezhad, *Mater. Lett.*, 2007, **61**, 4559–4561.
- 53 J. C. Yu, L. Z. Zhang, Q. Li, K. W. Kwong, A. W. Xu and J. Lin, *Langmuir*, 2003, **19**, 7673–7675.
- 54 P. S. Awati, S. V. Awate, P. P. Shah and V. Ramaswamy, *Catal. Commun.*, 2003, **4**, 393–400.
- 55 A. Mills, N. Elliott, I. P. Parkin, S. A. O'Neill and R. J. Clark, *J. Photochem. Photobiol., A*, 2002, **151**, 171–179.
- 56 A. Goossens, E.-L. Maloney and J. Schoonman, *Chem. Vap. Deposition*, 1998, **4**, 109–114.
- 57 S. Dilger, C. Hintze, M. Krumm, C. Lizandara-Pueyo, S. Deeb, S. Proch and S. Polarz, *J. Mater. Chem.*, 2010, **20**, 10032–10040.
- 58 D. Mardare, M. Tasca, M. Delibas and G. I. Rusu, *Appl. Surf. Sci.*, 2000, **156**, 200–206.
- 59 S. Meyer, R. Gorges and G. Kreisel, *Thin Solid Films*, 2004, **450**, 276–281.
- 60 W. Wang, B. Gu, L. Liang, W. A. Hamilton and D. J. Wesolowski, *J. Phys. Chem. B*, 2004, **108**, 14789–14792.
- 61 T. Kasuga, M. Hiramatsu, A. Hoson, T. Sekino and K. Niihara, *Langmuir*, 1998, **14**, 3160–3163.
- 62 D. V. Bavykin, J. M. Friedrich and F. C. Walsh, *Adv. Mater.*, 2006, **18**, 2807–2824.
- 63 J. Zhao, Z.-T. Jiang, J. Tan and R. Li, *J. Sol-Gel Sci. Technol.*, 2011, **58**, 436–441.
- 64 J. Konishi, K. Fujita, K. Nakanishi and K. Hirao, *Chem. Mater.*, 2006, **18**, 6069–6074.
- 65 S. O. Baumann, M. J. Elser, M. Auer, J. Bernardi, N. Huesing and O. Diwald, *Langmuir*, 2011, **27**, 1946–1953.
- 66 D. M. Antonelli and J. Y. Ying, *Angew. Chem., Int. Ed. Engl.*, 1995, **34**, 2014–2017.
- 67 Y. Q. Wang, X. H. Tang, L. X. Yin, W. P. Huang, Y. R. Hacohen and A. Gedanken, *Adv. Mater.*, 2000, **12**, 1183–1186.
- 68 H. Yoshitake, T. Sugihara and T. Tatsumi, *Chem. Mater.*, 2002, **14**, 1023–1029.
- 69 B. T. Holland, C. F. Blanford, T. Do and A. Stein, *Chem. Mater.*, 1999, **11**, 795–805.
- 70 G. Soler-Illia, E. L. Crepaldi, D. Grosso and C. Sanchez, *Curr. Opin. Colloid Interface Sci.*, 2003, **8**, 109–126.
- 71 S. W. Boettcher, J. Fan, C.-K. Tsung, Q. Shi and G. D. Stucky, *Acc. Chem. Res.*, 2007, **40**, 784–792.
- 72 Q. Sheng, Y. Cong, S. Yuan, J. Zhang and M. Anpo, *Microporous Mesoporous Mater.*, 2006, **95**, 220–225.
- 73 B. Smarsly, D. Grosso, T. Brezesinski, N. Pinna, C. Boissiere, M. Antonietti and C. Sanchez, *Chem. Mater.*, 2004, **16**, 2948–2952.
- 74 F. Jia, W. Sun, J. Zhang, Y. Li and B. Yang, *J. Mater. Chem.*, 2012, **22**, 2435–2441.
- 75 P. Hartmann, D.-K. Lee, B. M. Smarsly and J. Janek, *ACS Nano*, 2010, **4**, 3147–3154.
- 76 H. H. Ou and S. L. Lo, *Sep. Purif. Technol.*, 2007, **58**, 179–191.
- 77 S. T. Aruna, S. Tirosh and A. Zaban, *J. Mater. Chem.*, 2000, **10**, 2388–2391.
- 78 J. G. Li, T. Ishigaki and X. D. Sun, *J. Phys. Chem. C*, 2007, **111**, 4969–4976.
- 79 J. Li and D. Xu, *Chem. Commun.*, 2010, **46**, 2301–2303.
- 80 G. Liu, C. Sun, H. G. Yang, S. C. Smith, L. Wang, G. Q. Lu and H.-M. Cheng, *Chem. Commun.*, 2010, **46**, 755–757.
- 81 H. G. Yang, C. H. Sun, S. Z. Qiao, J. Zou, G. Liu, S. C. Smith, H. M. Cheng and G. Q. Lu, *Nature*, 2008, **453**, 638–642.
- 82 P. D. Cozzoli, A. Kornowski and H. Weller, *J. Am. Chem. Soc.*, 2003, **125**, 14539–14548.
- 83 P. D. Cozzoli, M. L. Curri, C. Giannini and A. Agostiano, *Small*, 2006, **2**, 413–421.
- 84 A. B. Corradi, F. Bondioli, B. Focher, A. M. Ferrari, C. Grippo, E. Mariani and C. Villa, *J. Am. Ceram. Soc.*, 2005, **88**, 2639–2641.
- 85 J. Xingtao, H. Wen, Z. Xudong, Z. Hongshi, L. Zhengmao and F. Yingjun, *Nanotechnology*, 2007, **18**, 075602.
- 86 K. Ding, Z. Miao, Z. Liu, Z. Zhang, B. Han, G. An, S. Miao and Y. Xie, *J. Am. Chem. Soc.*, 2007, **129**, 6362–6363.
- 87 D. Q. Zhang, M. C. Wen, P. Zhang, J. Zhu, G. S. Li and H. X. Li, *Langmuir*, 2012, **28**, 4543–4547.
- 88 Z. Jing, D. Guo, W. Wang, S. Zhang, W. Qi and B. Ling, *Solid State Sci.*, 2011, **13**, 1797–1803.
- 89 J. C. Colmenares, M. A. Aramendia, A. Marinas, J. M. Marinas and F. J. Urbano, *J. Mol. Catal. A: Chem.*, 2010, **331**, 58–63.
- 90 E. Ohayon and A. Gedanken, *Ultrason. Sonochem.*, 2010, **17**, 173–178.
- 91 D. A. H. Hanaor and C. C. Sorrell, *J. Mater. Sci.*, 2011, **46**, 855–874.

- 92 V. G. Kessler, G. I. Spijksma, G. A. Seisenbaeva, S. Hakansson, D. H. A. Blank and H. J. M. Bouwmeester, *J. Sol-Gel Sci. Technol.*, 2006, **40**, 163–179.
- 93 U. Schubert, *J. Mater. Chem.*, 2005, **15**, 3701–3715.
- 94 U. Schubert, *Acc. Chem. Res.*, 2007, **40**, 730–737.
- 95 D. B. Zhang, L. M. Qi, J. M. Ma and H. M. Cheng, *J. Mater. Chem.*, 2002, **12**, 3677–3680.
- 96 A. S. Pottier, S. Cassaignon, C. Chaneac, F. Villain, E. Tronc and J. P. Jolivet, *J. Mater. Chem.*, 2003, **13**, 877–882.
- 97 J. Beusen, M. K. Van Bael, H. Van den Rul, J. D'Haen and J. Mullens, *J. Eur. Ceram. Soc.*, 2007, **27**, 4529–4535.
- 98 E. Nilsson, H. Furusho, O. Terasaki and A. E. C. Palmqvist, *J. Mater. Res.*, 2011, **26**, 288–295.
- 99 S. Han, S.-H. Choi, S.-S. Kim, M. Cho, B. Jang, D.-Y. Kim, J. Yoon and T. Hyeon, *Small*, 2005, **1**, 812–816.
- 100 N. Kröger, M. B. Dickerson, G. Ahmad, Y. Cai, M. S. Haluska, K. H. Sandhage, N. Poulsen and V. C. Sheppard, *Angew. Chem., Int. Ed.*, 2006, **45**, 7239–7243.
- 101 M. Niederberger, G. Garnweitner, J. Buha, J. Polleux, J. Ba and N. Pinna, *J. Sol-Gel Sci. Technol.*, 2006, **40**, 259–266.
- 102 M. Niederberger, M. H. Bartl and G. D. Stucky, *Chem. Mater.*, 2002, **14**, 4364–4370.
- 103 T. J. Trentler, T. E. Denler, J. F. Bertone, A. Agrawal and V. L. Colvin, *J. Am. Chem. Soc.*, 1999, **121**, 1613–1614.
- 104 N. Huesing, B. Launay, D. Doshi and G. Kickelbick, *Chem. Mater.*, 2002, **14**, 2429–2432.
- 105 P. Kubiak, J. Geserick, N. Huesing and M. Wohlfahrt-Mehrens, *J. Power Sources*, 2008, **175**, 510–516.
- 106 J. Park, J. Joo, S. G. Kwon, Y. Jang and T. Hyeon, *Angew. Chem., Int. Ed.*, 2007, **46**, 4630–4660.
- 107 C. Liu, X. Wu, T. Klemmer, N. Shukla, X. Yang, D. Weller, A. G. Roy, M. Tanase and D. Laughlin, *J. Phys. Chem. B*, 2004, **108**, 6121–6123.
- 108 X. Jiang, Y. Wang, T. Herricks and Y. Xia, *J. Mater. Chem.*, 2004, **14**, 695–703.
- 109 R. E. Reeves and L. W. Mazzeno, *J. Am. Chem. Soc.*, 1954, **76**, 2533–2536.
- 110 D. Wang, R. Yu, N. Kumada and N. Kinomura, *Chem. Mater.*, 1999, **11**, 2008–2012.
- 111 A. Yamamoto and S. Kambara, *J. Am. Chem. Soc.*, 1959, **81**, 2663–2667.
- 112 A. D. Tinoco, E. V. Eames, C. D. Incarvito and A. M. Valentine, *Inorg. Chem.*, 2008, **47**, 8380–8390.
- 113 H. Thoms, M. Eppe, M. Froeba, J. Wong and A. Reller, *J. Mater. Chem.*, 1998, **8**, 1447–1451.
- 114 H. K. Yu, T. H. Eun, G.-R. Yi and S.-M. Yang, *J. Colloid Interface Sci.*, 2007, **316**, 175–182.
- 115 Q. Li, B. Liu, Y. Li, R. Liu, X. Li, D. Li, S. Yu, D. Liu, P. Wang, B. Li, B. Zou, T. Cui and G. Zou, *J. Alloys Compd.*, 2009, **471**, 477–480.
- 116 V. Krasil'nikov, A. Shtin, O. Gyrdasova, E. Polyakov and G. Shveikin, *Russ. J. Inorg. Chem.*, 2008, **53**, 1065–1069.
- 117 L. Saadoun, J. A. Ayllón, J. Jiménez-Becerril, J. Peral, X. Domènech and R. Rodríguez-Clemente, *Appl. Catal., B*, 1999, **21**, 269–277.
- 118 M. Pal, J. García Serrano, P. Santiago and U. Pal, *J. Phys. Chem. C*, 2006, **111**, 96–102.
- 119 P. Kubiak, M. Pfanzelt, J. Geserick, U. Hoermann, N. Huesing, U. Kaiser and M. Wohlfahrt-Mehrens, *J. Power Sources*, 2009, **194**, 1099–1104.
- 120 R. Schiller, C. K. Weiss, J. Geserick, N. Huesing and K. Landfester, *Chem. Mater.*, 2009, **21**, 5088–5098.
- 121 R. Schiller, C. K. Weiss and K. Landfester, *Nanotechnology*, 2010, **21**, 405603.
- 122 N. Nabih, R. Schiller, I. Lieberwirth, E. Kockrick, R. Frind, S. Kaskel, C. K. Weiss and K. Landfester, *Nanotechnology*, 2011, **22**, 135606.
- 123 K. Landfester and C. K. Weiss, in *Modern Techniques for Nano- and Microreactors/Reactions*, ed. F. Caruso, 2010, vol. 229, pp. 1–49.
- 124 K. Landfester, *Angew. Chem., Int. Ed.*, 2009, **48**, 4488–4507.
- 125 M. Sanchez-Dominguez, L. F. Liotta, G. Di Carlo, G. Pantaleo, A. M. Venezia, C. Solans and M. Boutonnet, *Catal. Today*, 2010, **158**, 35–43.
- 126 S. S. Hong, M. S. Lee, G. D. Lee, K. T. Lim and B. J. Ha, *Mater. Lett.*, 2003, **57**, 2975–2979.
- 127 S. S. Hong, M. S. Lee, C. S. Ju, G. D. Lee, S. S. Park and K. T. Lim, *Catal. Today*, 2004, **93–5**, 871–876.
- 128 X. Shen, J. Zhang and B. Tian, *J. Hazard. Mater.*, 2011, **192**, 651–657.
- 129 F. A. Deorsola and D. Vallauri, *Powder Technol.*, 2009, **190**, 304–309.
- 130 L. Xuebing, L. Tanwei, W. Changzheng and Z. Zude, *J. Nanopart. Res.*, 2007, **9**, 1081–1086.
- 131 C. E. Zubieta, J. F. A. Soltero-Martinez, C. V. Luengo and P. C. Schulz, *Powder Technol.*, 2011, **212**, 410–417.
- 132 C. Zurmuehl, R. Popescu, D. Gerthsen and C. Feldmann, *Solid State Sci.*, 2011, **13**, 1505–1509.
- 133 J. Lin, Y. Lin, P. Liu, M. J. Meziani, L. F. Allard and Y. P. Sun, *J. Am. Chem. Soc.*, 2002, **124**, 11514–11518.
- 134 P. D. Moran, J. R. Bartlett, J. L. Woolfrey, G. A. Bowmaker and R. P. Cooney, *J. Sol-Gel Sci. Technol.*, 1997, **8**, 65–69.
- 135 M. Xu, W. J. B. Long, A. H. Huang, Y. J. Luo, S. H. Feng and R. R. Xu, *Langmuir*, 1999, **15**, 8822–8825.
- 136 M. Andersson, A. Kiselev, L. Oesterlund and A. E. C. Palmqvist, *J. Phys. Chem. C*, 2007, **111**, 6789–6797.
- 137 D. Holzinger and G. Kickelbick, *Chem. Mater.*, 2003, **15**, 4944–4948.
- 138 Z. Yang, D. Choi, S. Kerisit, K. M. Rosso, D. Wang, J. Zhang, G. Graff and J. Liu, *J. Power Sources*, 2009, **192**, 588–598.
- 139 D. W. Murphy, R. J. Cava, S. M. Zahurak and A. Santoro, *Solid State Ionics*, 1983, **9–10**, 413–417.
- 140 B. Zachau-Christiansen, K. West, T. Jacobsen and S. Atlung, *Solid State Ionics*, 1988, **28**, 1176–1182.
- 141 D. Dambournet, I. Belharouak and K. Amine, *Chem. Mater.*, 2010, **22**, 1173–1179.
- 142 T. Ohzuku, T. Kodama and T. Hirai, *J. Power Sources*, 1985, **14**, 153–166.
- 143 S. Y. Huang, L. Kavan, I. Exnar and M. Graetzel, *J. Electrochem. Soc.*, 1995, **142**, L142–L144.
- 144 Y. S. Hu, L. Kienle, Y. G. Guo and J. Maier, *Adv. Mater.*, 2006, **18**, 1421–1426.
- 145 M. A. Reddy, M. S. Kishore, V. Pralong, V. Caignaert, U. V. Varadaraju and B. Raveau, *Electrochem. Commun.*, 2006, **8**, 1299–1303.
- 146 A. R. Armstrong, G. Armstrong, J. Canales, R. Garcia and P. G. Bruce, *Adv. Mater.*, 2005, **17**, 862–865.
- 147 A. R. Armstrong, G. Armstrong, J. Canales and P. G. Bruce, *J. Power Sources*, 2005, **146**, 501–506.
- 148 A. R. Armstrong, G. Armstrong, J. Canales and P. G. Bruce, *Angew. Chem., Int. Ed.*, 2004, **43**, 2286–2288.
- 149 M. Zukalova, M. Kalbac, L. Kavan, I. Exnar and M. Graetzel, *Chem. Mater.*, 2005, **17**, 1248–1255.
- 150 M. Inaba, Y. Oba, F. Niina, Y. Murota, Y. Ogino, A. Tasaka and K. Hirota, *J. Power Sources*, 2009, **189**, 580–584.
- 151 J. Jitputti, Y. Suzuki and S. Yoshikawa, *Catal. Commun.*, 2008, **9**, 1265–1271.
- 152 M. V. Koudriachova, *J. Nano Res.*, 2010, **11**, 159–164.
- 153 Q. Li, J. Zhang, B. Liu, M. Li, R. Liu, X. Li, H. Ma, S. Yu, L. Wang, Y. Zou, Z. Li, B. Zou, T. Cui and G. Zou, *Inorg. Chem.*, 2008, **47**, 9870–9873.
- 154 J. M. Li, W. Wan, H. H. Zhou, J. J. Li and D. S. Xu, *Chem. Commun.*, 2011, **47**, 3439–3441.
- 155 B. Liu, D. Deng, J. Y. Lee and E. S. Aydil, *J. Mater. Res.*, 2010, **25**, 1588–1594.
- 156 S.-T. Myung, N. Takahashi, S. Komaba, C. S. Yoon, Y.-K. Sun, K. Amine and H. Yashiro, *Adv. Funct. Mater.*, 2011, **21**, 3231–3241.
- 157 T. Okumura, T. Fukutsuka, A. Yanagihara, Y. Orikasa, H. Arai, Z. Ogumi and Y. Uchimoto, *Chem. Mater.*, 2011, **23**, 3636–3644.
- 158 L. Qi, Y. Liu and C. Li, *Appl. Surf. Sci.*, 2010, **257**, 1660–1665.
- 159 M. Wilkening, C. Lyness, A. R. Armstrong and P. G. Bruce, *J. Phys. Chem. C*, 2009, **113**, 4741–4744.
- 160 M. Wilkening, J. Heine, C. Lyness, A. R. Armstrong and P. G. Bruce, *Phys. Rev. B: Condens. Matter Mater. Phys.*, 2009, **80**, 064302.
- 161 Z. X. Yang, G. D. Du, Z. P. Guo, X. B. Yu, Z. X. Chen, T. L. Guo and H. K. Liu, *J. Mater. Chem.*, 2011, **21**, 8591–8596.

- 162 B. Zhao, F. Chen, H. Liu and J. Zhang, *J. Phys. Chem. Solids*, 2011, **72**, 201–206.
- 163 D. H. Lee, J. G. Park, K. J. Choi, H. J. Choi and D. W. Kim, *Eur. J. Inorg. Chem.*, 2008, 878–882.
- 164 M. A. Reddy, M. S. Kishore, V. Pralong, U. V. Varadaraju and B. Raveau, *Electrochem. Solid-State Lett.*, 2007, **10**, A29–A31.
- 165 R. van de Krol, A. Goossens and E. A. Meulenkaamp, *J. Electrochem. Soc.*, 1999, **146**, 3150–3154.
- 166 A. Stashans, S. Lunell, R. Bergstrom, A. Hagfeldt and S. E. Lindquist, *Phys. Rev. B: Condens. Matter*, 1996, **53**, 159–170.
- 167 H. Lindstrom, S. Sodergren, A. Solbrand, H. Rensmo, J. Hjelm, A. Hagfeldt and S. E. Lindquist, *J. Phys. Chem. B*, 1997, **101**, 7710–7716.
- 168 M. Wagemaker, A. P. M. Kentgens and F. M. Mulder, *Nature*, 2002, **418**, 397–399.
- 169 R. Baddour-Hadjean, S. Bach, M. Smirnov and J. P. Pereira-Ramos, *J. Raman Spectrosc.*, 2004, **35**, 577–585.
- 170 M. Wagemaker, W. J. H. Borghols, E. R. H. van Eck, A. P. M. Kentgens, G. L. Kearley and F. M. Mulder, *Chem.–Eur. J.*, 2007, **13**, 2023–2028.
- 171 M. Wagemaker, W. J. H. Borghols and F. M. Mulder, *J. Am. Chem. Soc.*, 2007, **129**, 4323–4327.
- 172 J. Wang, J. Polleux, J. Lim and B. Dunn, *J. Phys. Chem. C*, 2007, **111**, 14925–14931.
- 173 G. Sudant, E. Baudrin, D. Larcher and J. M. Tarascon, *J. Mater. Chem.*, 2005, **15**, 1263–1269.
- 174 C. Jiang, M. Wei, Z. Qi, T. Kudo, I. Honma and H. Zhou, *J. Power Sources*, 2007, **166**, 239–243.
- 175 L. Kavan, J. Rathousky, M. Graetzel, V. Shklover and A. Zukal, *J. Phys. Chem. B*, 2000, **104**, 12012–12020.
- 176 J. R. Li, Z. L. Tang and Z. T. Zhang, *Electrochem. Solid-State Lett.*, 2005, **8**, A316–A319.
- 177 S. Panero, B. Scrosati, M. Wachtler and F. Croce, *J. Power Sources*, 2004, **129**, 90–95.
- 178 P. Poizot, S. Laruelle, S. Grugeon, L. Dupont and J. M. Tarascon, *Nature*, 2000, **407**, 496–499.
- 179 F. Badway, I. Plitz, S. Grugeon, S. Laruelle, M. Dolle, A. S. Gozdz and J. M. Tarascon, *Electrochem. Solid-State Lett.*, 2002, **5**, A115–A118.
- 180 P. G. Bruce, B. Scrosati and J.-M. Tarascon, *Angew. Chem., Int. Ed.*, 2008, **47**, 2930–2946.
- 181 L. Kavan, J. Rathousky, M. Graetzel, V. Shklover and A. Zukal, *Microporous Mesoporous Mater.*, 2001, **44**, 653–659.
- 182 I. Moriguchi, R. Hidaka, H. Yamada and T. Kudo, *Solid State Ionics*, 2005, **176**, 2361–2366.
- 183 D. Fattakhova-Rohlfing, M. Wark, T. Brezesinski, B. M. Smarsly and J. Rathousky, *Adv. Funct. Mater.*, 2007, **17**, 123–132.
- 184 K. Saravanan, K. Ananthanarayanan and P. Balaya, *Energy Environ. Sci.*, 2010, **3**, 939–948.
- 185 M. Pfanztel, P. Kubiak, U. Hoermann, U. Kaiser and M. Wohlfahrt-Mehrens, *Ionics*, 2009, **15**, 657–663.
- 186 Y. Ishii, Y. Kanamori, T. Kawashita, I. Mukhopadhyay and S. Kawasaki, *J. Phys. Chem. Solids*, 2010, **71**, 511–514.
- 187 S.-J. Park, H. Kim, Y.-J. Kim and H. Lee, *Electrochim. Acta*, 2011, **56**, 5355–5362.
- 188 I. Moriguchi, R. Hidaka, H. Yamada, T. Kudo, H. Murakami and N. Nakashima, *Adv. Mater.*, 2006, **18**, 69–73.
- 189 D. Wang, D. Choi, J. Li, Z. Yang, Z. Nie, R. Kou, D. Hu, C. Wang, L. V. Saraf, J. Zhang, I. a. Aksay and J. Liu, *ACS Nano*, 2009, **3**, 907–914.
- 190 B.-L. He, B. Dong and H.-L. Li, *Electrochem. Commun.*, 2007, **9**, 425–430.
- 191 Y.-G. Guo, Y.-S. Hu, W. Sigle and J. Maier, *Adv. Mater.*, 2007, **19**, 2087–2091.
- 192 H. S. Zhou, D. L. Li, M. Hibino and I. Honma, *Angew. Chem., Int. Ed.*, 2005, **44**, 797–802.
- 193 B. Erjavec, R. Dominko, P. Umek, S. Sturm, S. Pejovnik, M. Gaberscek and J. Jamnik, *Electrochem. Commun.*, 2008, **10**, 926–929.
- 194 M. Mancini, P. Kubiak, J. Geserick, R. Marassi, N. Huesing and M. Wohlfahrt-Mehrens, *J. Power Sources*, 2009, **189**, 585–589.
- 195 M. Mancini, P. Kubiak, M. Wohlfahrt-Mehrens and R. Marassi, *J. Electrochem. Soc.*, 2010, **157**, A164–A170.
- 196 D. Choi, D. Wang, V. V. Viswanathan, I.-T. Bae, W. Wang, Z. Nie, J.-G. Zhang, G. L. Graff, J. Liu, Z. Yang and T. Duong, *Electrochem. Commun.*, 2010, **12**, 378–381.
- 197 M. Mancini, F. Nobili, R. Tossici, M. Wohlfahrt-Mehrens and R. Marassi, *J. Power Sources*, 2011, **196**, 9665–9671.
- 198 O. Johnson, *Phys. Rev.*, 1964, **136**, A284–A290.
- 199 M. Koudriachova, N. Harrison and S. de Leeuw, *Phys. Rev. Lett.*, 2001, **86**, 1275–1278.
- 200 M. V. Koudriachova, N. M. Harrison and S. W. de Leeuw, *Solid State Ionics*, 2003, **157**, 35–38.
- 201 F. Gligor and S. Deleeuw, *Solid State Ionics*, 2006, **177**, 2741–2746.
- 202 M. V. Koudriachova, *J. Power Sources*, 2011, **196**, 6898–6901.
- 203 E. Baudrin, S. Cassaignon, M. Koelsch, J. P. Jolivet, L. Dupont and J. M. Tarascon, *Electrochem. Commun.*, 2007, **9**, 337–342.
- 204 S. Bach, J. P. Pereira-Ramos and P. Willman, *Electrochim. Acta*, 2010, **55**, 4952–4959.
- 205 W. J. Macklin and R. J. Neat, *Solid State Ionics*, 1992, **56**, 694–700.
- 206 L. Kavan, D. Fattakhova and P. Krtil, *J. Electrochem. Soc.*, 1999, **146**, 1375–1379.
- 207 A. Beltrán, L. Gracia and J. Andrés, *J. Phys. Chem. B*, 2006, **110**, 23417–23423.
- 208 K. Madhusudan Reddy, S. V. Manorama and A. Ramachandra Reddy, *Mater. Chem. Phys.*, 2003, **78**, 239–245.
- 209 T. Ohzuku, Z. Takehara and S. Yoshizawa, *Electrochim. Acta*, 1979, **24**, 219–222.
- 210 F. Bonino, L. Busani, M. Lazzari, M. Manstretta, B. Rivolta and B. Scrosati, *J. Power Sources*, 1981, **6**, 261–270.
- 211 C. Jiang, I. Honma, T. Kudo and H. Zhou, *Electrochem. Solid-State Lett.*, 2007, **10**, A127–A127.
- 212 D. Wang, D. Choi, Z. Yang, V. V. Viswanathan, Z. Nie, C. Wang, Y. Song, J. G. Zhang and J. Liu, *Chem. Mater.*, 2008, **20**, 3435–3442.
- 213 H. Qiao, Y. Wang, L. Xiao and L. Zhang, *Electrochem. Commun.*, 2008, **10**, 1280–1283.
- 214 H. Qiao, D. Tao, Y. Wang, Y. Cai, F. Huang, X. Yang, J. Wei and Q. Wei, *Chem. Phys. Lett.*, 2010, **490**, 180–183.
- 215 M. Pfanztel, P. Kubiak and M. Wohlfahrt-Mehrens, *Electrochem. Solid-State Lett.*, 2010, **13**, A91–A91.
- 216 E. P. Roth and D. H. Doughty, *J. Power Sources*, 2004, **128**, 308–318.
- 217 H. H. Lee, C. C. Wan and Y. Y. Wang, *J. Electrochem. Soc.*, 2004, **151**, A542–A542.
- 218 H. Yang, H. Bang, K. Amine and J. Prakash, *J. Electrochem. Soc.*, 2005, **152**, A73–A73.
- 219 Q. Wang, J. Sun, X. Yao and C. Chen, *J. Electrochem. Soc.*, 2006, **153**, A329–A329.
- 220 M. Marinaro, M. Pfanztel, P. Kubiak, R. Marassi and M. Wohlfahrt-Mehrens, *J. Power Sources*, 2011, **196**, 9825–9829.
- 221 F. Nobili, S. Dsoke, M. Mancini, R. Tossici and R. Marassi, *J. Power Sources*, 2008, **180**, 845–851.
- 222 S. Zhang, *Electrochim. Acta*, 2002, **48**, 241–246.
- 223 J. S. Chen and X. W. Lou, *J. Power Sources*, 2010, **195**, 2905–2908.
- 224 R. B. Khomane, *J. Colloid Interface Sci.*, 2011, **356**, 369–372.
- 225 U. Hörmann, M. Pfanztel, P. Kubiak, T. Froeschl, M. Wohlfahrt-Mehrens, N. Huesing and U. Kaiser, in *Material Science*, ed. W. Jäger, Kiel, Germany, 2011, vol. 3.
- 226 J. D. Eshelby, *J. Appl. Phys.*, 1953, **24**, 176–179.
- 227 J. D. Eshelby, *Philos. Mag.*, 1958, **3**, 440–447.
- 228 S. Amelinckx, *Philos. Mag.*, 1958, **3**, 425–428.
- 229 W. J. H. Borghols, M. Wagemaker, U. Lafont, E. M. Kelder and F. M. Mulder, *Chem. Mater.*, 2008, **20**, 2949–2955.
- 230 L. Benco, J. L. Barras, C. A. Daul and E. Deiss, *Inorg. Chem.*, 1999, **38**, 20–28.
- 231 M. V. Koudriachova, S. W. de Leeuw and N. M. Harrison, *Chem. Phys. Lett.*, 2003, **371**, 150–156.
- 232 N. A. Milne, M. Skyllas-Kazacos and V. Luca, *J. Phys. Chem. C*, 2009, **113**, 12983–12995.
- 233 B. Ohtani, *Chem. Lett.*, 2008, **37**, 217–229.
- 234 S. Monticone, R. Tufeu, A. V. Kanaev, E. Scolan and C. Sanchez, *Appl. Surf. Sci.*, 2000, **162**, 565–570.
- 235 U. Hoermann, U. Kaiser, M. Albrecht, J. Geserick and N. Huesing, in *16th International Conference on Microscopy of Semiconducting Materials*, ed. T. Walther, P. D. Nellist, J. L. Hutchison and A. G. Cullis, 2010, vol. 209.



- 236 H. Gnaser, B. Huber and C. Ziegler, *Encycl. Nanosci. Nanotechnol.*, 2004, **6**, 505–535.
- 237 C. Kormann, D. W. Bahnemann and M. R. Hoffmann, *J. Phys. Chem.*, 1988, **92**, 5196–5201.
- 238 R. R. Hasiguti, *Annu. Rev. Mater. Sci.*, 1972, **2**, 69–92.
- 239 R. Bacsa, J. Kiwi, T. Ohno, P. Albers and V. Nadtochenko, *J. Phys. Chem. B*, 2005, **109**, 5994–6003.
- 240 C. M. Wang, Z. G. Yang, S. Thevuthasan, J. Liu, D. R. Baer, D. Choi, D. H. Wang, J. G. Zhang, L. V. Saraf and Z. M. Nie, *Appl. Phys. Lett.*, 2009, **94**, 233116.
- 241 M. Vijayakumar, S. Kerisit, C. Wang, Z. Nie, K. M. Rosso, Z. Yang, G. Graff, J. Liu and J. Hu, *J. Phys. Chem. C*, 2009, **113**, 14567–14574.
- 242 C.-M. Wang, W. Xu, J. Liu, J.-G. Zhang, L. V. Saraf, B. W. Arey, D. Choi, Z.-G. Yang, J. Xiao, S. Thevuthasan and D. R. Baer, *Nano Lett.*, 2011, **11**, 1874–1880.
- 243 X. H. Liu and J. Y. Huang, *Energy Environ. Sci.*, 2011, **4**, 3844–3860.
- 244 H. Ghassemi, M. Au, N. Chen, P. A. Heiden and R. S. Yassar, *ACS Nano*, 2011, **5**, 7805–7811.
- 245 G. S. Li, J. Boerio-Goates, B. F. Woodfield and L. P. Li, *Appl. Phys. Lett.*, 2004, **85**, 2059–2061.
- 246 L. De Caro, E. Carlino, G. Caputo, P. D. Cozzoli and C. Giannini, *Nat. Nanotechnol.*, 2010, **5**, 360–365.
- 247 Z. X. Huang, P. Thomson and S. L. Di, *J. Phys. Chem. Solids*, 2007, **68**, 530–535.
- 248 V. M. Huxter, A. Lee, S. S. Lo and G. D. Scholes, *Nano Lett.*, 2009, **9**, 405–409.
- 249 S. Tsunekawa, K. Ishikawa, Z. Q. Li, Y. Kawazoe and A. Kasuya, *Phys. Rev. Lett.*, 2000, **85**, 3440–3443.
- 250 M. V. Koudriachova, N. M. Harrison and S. W. de Leeuw, *Phys. Rev. B: Condens. Matter*, 2002, **65**, 235423.
- 251 S. Kerisit, K. M. Rosso, Z. G. Yang and J. Liu, *J. Phys. Chem. C*, 2009, **113**, 20998–21007.
- 252 J. G. Traylor, H. G. Smith, R. M. Nicklow and M. K. Wilkinson, *Phys. Rev. B: Solid State*, 1971, **3**, 3457–3472.
- 253 L. Gerward and J. S. Olsen, *J. Appl. Crystallogr.*, 1997, **30**, 259–264.
- 254 T. Arlt, M. Bermejo, M. A. Blanco, L. Gerward, J. Z. Jiang, J. S. Olsen and J. M. Recio, *Phys. Rev. B: Condens. Matter*, 2000, **61**, 14414–14419.
- 255 S. D. Mo and W. Y. Ching, *Phys. Rev. B: Condens. Matter*, 1995, **51**, 13023–13032.
- 256 B. Chen, H. Zhang, K. A. Dunphy-Guzman, D. Spagnoli, M. B. Kruger, D. V. S. Muthu, M. Kunz, S. Fakra, J. Z. Hu, Q. Z. Guo and J. F. Banfield, *Phys. Rev. B: Condens. Matter Mater. Phys.*, 2009, **79**, 235403.
- 257 M. J. Mayo, R. W. Siegel, A. Narayanasamy and W. D. Nix, *J. Mater. Res.*, 1990, **5**, 1073–1082.
- 258 A. Hallil, E. Amzallag, S. Landron and R. Tetot, *Surf. Sci.*, 2011, **605**, 738–745.
- 259 U. Diebold, *Surf. Sci. Rep.*, 2003, **48**, 53–229.
- 260 D. J. Shu, S. T. Ge, M. Wang and N. B. Ming, *Phys. Rev. Lett.*, 2008, **101**, 116102.
- 261 R. Kern and P. Muller, *Surf. Sci.*, 1997, **392**, 103–133.
- 262 D. J. Eaglesham and M. Cerullo, *Phys. Rev. Lett.*, 1990, **64**, 1943–1946.
- 263 S. A. Chaparro, Y. Zhang, J. Drucker, D. Chandrasekhar and D. J. Smith, *J. Appl. Phys.*, 2000, **87**, 2245–2254.
- 264 H. P. Strunk, M. Albrecht, S. Christiansen, W. Dorsch, U. Hoermann, B. Jahn and T. Remmele, *Phys. Status Solidi A*, 1999, **171**, 215–225.
- 265 T. Wiebach, M. Schmidbauer, M. Hanke, H. Raidt, R. Kohler and H. Wawra, *Phys. Rev. B: Condens. Matter*, 2000, **61**, 5571–5578.
- 266 M. Albrecht, S. Christiansen, J. Michler, W. Dorsch, H. P. Strunk, P. O. Hansson and E. Bauser, *Appl. Phys. Lett.*, 1995, **67**, 1232–1234.
- 267 J. Tersoff, *Phys. Rev. Lett.*, 1995, **74**, 5080–5083.
- 268 M. Wagemaker, D. Lutzenkirchen-Hecht, P. Keil, A. A. van Well and R. Frahm, *Phys. Rev. B: Condens. Matter Mater. Phys.*, 2003, **336**, 118–123.
- 269 M. V. Koudriachova, *J. Solid State Electrochem.*, 2010, **14**, 549–553.
- 270 A. Fujishima, T. N. Rao and D. A. Tryk, *J. Photochem. Photobiol., C*, 2000, **1**, 1–21.
- 271 M. A. Vannice, S. Y. Wang and S. H. Moon, *J. Catal.*, 1981, **71**, 152–166.
- 272 G. C. Bond, C. Louis and D. T. Thompson, *Catalysis by Gold*, Imperial Press, London, 2007.
- 273 G. C. Bond, *Gold Bull.*, 1972, **5**, 11–13.
- 274 G. J. Hutchings and R. Joffe, *Appl. Catal.*, 1986, **20**, 215–218.
- 275 M. Haruta, *Catal. Surv. Jpn.*, 1997, **1**, 61–73.
- 276 D. Cameron, R. Holliday and D. Thompson, *J. Power Sources*, 2003, **118**, 298–303.
- 277 Q. Fu, W. Deng, H. Saltsburg and M. Flytzani-Stephanopoulos, *Appl. Catal., B*, 2005, **56**, 57–68.
- 278 W. Deng, J. De Jesus, H. Saltsburg and M. Flytzani-Stephanopoulos, *Appl. Catal., A*, 2005, **291**, 126–135.
- 279 G. Mul, A. Zwijnenburg, B. van der Linden, M. Makkee and J. A. Moulijn, *J. Catal.*, 2001, **201**, 128–137.
- 280 A. Ueda, T. Oshima and M. Haruta, *Appl. Catal., B*, 1997, **12**, 81–93.
- 281 C. W. Corti, R. J. Holliday and D. T. Thompson, *Top. Catal.*, 2007, **44**, 331–343.
- 282 M. J. Kahlich, H. A. Gasteiger and R. J. Behm, *J. Catal.*, 1999, **182**, 430–440.
- 283 B. Hoehlein, P. Biedermann, T. Grube and R. Menzer, *J. Power Sources*, 1999, **84**, 203–213.
- 284 L. F. Brown, *Int. J. Hydrogen Energy*, 2001, **26**, 381–397.
- 285 D. L. Trimm and Z. I. Onsan, *Catal. Rev. Sci. Eng.*, 2001, **43**, 31–84.
- 286 F. Joensen and J. R. Rostrup-Nielsen, *J. Power Sources*, 2002, **105**, 195–201.
- 287 J. D. Holladay, J. Hu, D. L. King and Y. Wang, *Catal. Today*, 2009, **139**, 244–260.
- 288 B. Schumacher, Y. Denkwitz, V. Plzak, M. Kinne and R. J. Behm, *J. Catal.*, 2004, **224**, 449–462.
- 289 P. Konova, A. Naydenov, C. Venkov, D. Mehandjiev, D. Andreeva and T. Tabakova, *J. Mol. Catal. A: Chem.*, 2004, **213**, 235–240.
- 290 F. Moreau and G. C. Bond, *Top. Catal.*, 2007, **44**, 95–101.
- 291 M. Okumura, S. Nakamura, S. Tsubota, T. Nakamura, M. Azuma and M. Haruta, *Catal. Lett.*, 1998, **51**, 53–58.
- 292 M. M. Schubert, S. Hackenberg, A. C. van Veen, M. Muhler, V. Plzak and R. J. Behm, *J. Catal.*, 2001, **197**, 113.
- 293 M. A. Bollinger and M. A. Vannice, *Appl. Catal., B*, 1996, **8**, 417–443.
- 294 F. Bocuzzi, A. Chiorino, S. Tsubota and M. Haruta, *J. Phys. Chem.*, 1996, **100**, 3625–3631.
- 295 F. Bocuzzi, A. Chiorino and M. Manzoli, *Mater. Sci. Eng., C*, 2001, **15**, 215–217.
- 296 J. R. Sanchez and J. W. Evans, *Phys. Rev. B: Condens. Matter*, 1999, **59**, 3224–3233.
- 297 C. K. Costello, M. C. Kung, H. S. Oh, Y. Wang and H. H. Kung, *Appl. Catal., A*, 2002, **232**, 159–168.
- 298 J. Guzman and B. C. Gates, *J. Phys. Chem. B*, 2002, **106**, 7659–7665.
- 299 E. D. Park and J. S. Lee, *J. Catal.*, 1999, **186**, 1–11.
- 300 T. I. Valdez and S. R. Narayanan, in *Proceedings of the Second International Symposium on Proton Conducting Membrane Fuel Cell II*, ed. S. F. Gottesfeld, 1999, vol. 98, pp. 380–387.
- 301 T. V. W. Janssens, A. Carlsson, A. Puig-Molina and B. S. Clausen, *J. Catal.*, 2006, **240**, 108–113.
- 302 T. V. W. Janssens, B. S. Clausen, B. Hvolbaek, H. Falsig, C. H. Christensen, T. Bligaard and J. K. Nørskov, *Top. Catal.*, 2007, **44**, 15–26.
- 303 M. Kotobuki, R. Leppelt, D. Hansgen, D. Widmann and R. J. Behm, *J. Catal.*, 2009, **264**, 67–76.
- 304 V. A. Bondzie, S. C. Parker and C. T. Campbell, *J. Vac. Sci. Technol., A*, 1999, **17**, 1717–1720.
- 305 Z. P. Liu, X. Q. Gong, J. Kohanoff, C. Sanchez and P. Hu, *Phys. Rev. Lett.*, 2003, **91**, 266102–266101.
- 306 L. M. Molina and B. Hammer, *Appl. Catal., A*, 2005, **291**, 21–31.
- 307 I. N. Remediakis, N. Lopez and J. K. Nørskov, *Appl. Catal., A*, 2005, **291**, 13–20.
- 308 M. Boronat and A. Corma, *Dalton Trans.*, 2010, **39**, 8538–8546.
- 309 I. X. Green, W. Tang, M. Neurock and J. T. Yates, *Science*, 2011, **333**, 736–739.

- 310 D. Widmann and R. J. Behm, *Angew. Chem., Int. Ed.*, 2011, **50**, 10241–10245.
- 311 N. Lopez and J. K. Norskov, *J. Am. Chem. Soc.*, 2002, **124**, 11262–11263.
- 312 M. S. Chen and D. W. Goodman, *Science*, 2004, **306**, 252–255.
- 313 J. D. Grunwaldt, M. Maciejewski, O. S. Becker, P. Fabrizioli and A. Baiker, *J. Catal.*, 1999, **186**, 458–469.
- 314 S. D. Lin, M. A. Bollinger and M. A. Vannice, *Catal. Lett.*, 1993, **17**, 245–262.
- 315 H. Sakurai, T. Akita, S. Tsubota, M. Kiuchi and M. Haruta, *Appl. Catal., A*, 2005, **291**, 179–189.
- 316 D. Widmann, Y. Liu, F. Schueth and R. J. Behm, *J. Catal.*, 2010, **276**, 292–305.
- 317 M. Comotti, W. C. Li, B. Spliethoff and F. Schueth, *J. Am. Chem. Soc.*, 2006, **128**, 917–924.
- 318 M. Date, M. Okumura, S. Tsubota and M. Haruta, *Angew. Chem., Int. Ed.*, 2004, **43**, 2129–2132.
- 319 C. K. Costello, J. H. Yang, H. Y. Law, Y. Wang, J. N. Lin, L. D. Marks, M. C. Kung and H. H. Kung, *Appl. Catal., A*, 2003, **243**, 15–24.
- 320 F. Gao, T. E. Wood and D. W. Goodman, *Catal. Lett.*, 2010, **134**, 9–12.
- 321 R. Zanella, S. Giorgio, C. H. Shin, C. R. Henry and C. Louis, *J. Catal.*, 2004, **222**, 357–367.
- 322 Y. Denkwitz, Z. Zhao, U. Hörmann, U. Kaiser, V. Plzak and R. J. Behm, *J. Catal.*, 2007, **251**, 363–373.
- 323 H. H. Kung, M. C. Kung and C. K. Costello, *J. Catal.*, 2003, **216**, 425–432.
- 324 S. H. Overbury, L. Ortiz-Soto, H. Zhu, B. Lee, M. D. Amiridis and S. Dai, *Catal. Lett.*, 2004, **95**, 99–106.
- 325 D. Wang, Z. Ma, S. Dai, J. Liu, Z. Nie, M. H. Engelhard, Q. Huo, C. Wang and R. Kou, *J. Phys. Chem. C*, 2008, **112**, 13499–13509.
- 326 W. F. Yan, S. M. Mahurin, B. Chen, S. H. Overbury and S. Dai, *J. Phys. Chem. B*, 2005, **109**, 15489–15496.
- 327 V. S. Narkhede, A. DeToni, V. V. Narkhede, M. Guraya, J. W. Niemantsverdriet, M. W. E. van den Berg, W. Gruenert and H. Gies, *Microporous Mesoporous Mater.*, 2009, **118**, 52–60.
- 328 M. Haruta, N. Yamada, T. Kobayashi and S. Iijima, *J. Catal.*, 1989, **115**, 301–309.
- 329 M. Haruta, S. Tsubota, T. Kobayashi, H. Kageyama, M. J. Genet and B. Delmon, *J. Catal.*, 1993, **144**, 175–192.
- 330 M. Okumura, K. Tanaka, A. Ueda and M. Haruta, *Solid State Ionics*, 1997, **95**, 143–149.
- 331 D. B. Akolekar and S. K. Bhargava, *J. Mol. Catal. A: Chem.*, 2005, **236**, 77–86.
- 332 Y. Tai, W. Yamaguchi, M. Okada, F. Ohashi, K. Shimizu, A. Satsuma, K. Tajiri and H. Kageyama, *J. Catal.*, 2010, **270**, 234–241.
- 333 S. Gaur, J. T. Miller, D. Stellwagen, A. Sanampudi, C. S. S. R. Kumar and J. J. Spivey, *Phys. Chem. Chem. Phys.*, 2011, **14**, 1627–1634.
- 334 A. Corma and H. Garcia, *Chem. Soc. Rev.*, 2008, **37**, 2096–2126.
- 335 R. Zanella, L. Delannoy and C. Louis, *Appl. Catal., A*, 2005, **291**, 62–72.
- 336 G. R. Bamwenda, S. Tsubota, T. Nakamura and M. Haruta, *Catal. Lett.*, 1997, **44**, 83–87.
- 337 G. Mul and J. A. Moulijn, in *Supported Metals in Catalysis*, ed. J. A. Anderson and M. F. Garcia, Imperial College Press, London, 2005, vol. 5, pp. 1–32.
- 338 A. I. Kozlov, A. P. Kozlova, H. Liu and Y. Iwasawa, *Appl. Catal., A*, 1999, **182**, 9–28.
- 339 M. A. Centeno, M. Paulis, M. Montes and J. A. Odriozola, *Appl. Catal., A*, 2002, **234**, 65–78.
- 340 J. P. Brunelle, *Pure Appl. Chem.*, 1978, **50**, 1211–1229.
- 341 C. K. Chang, Y. J. Chen and C. T. Yeh, *Appl. Catal., A*, 1998, **174**, 13–23.
- 342 R. Zanella, S. Giorgio, C. R. Henry and C. Louis, *J. Phys. Chem. B*, 2002, **106**, 7634–7642.
- 343 Y. Denkwitz, J. Geserick, U. Hörmann, V. Plzak, U. Kaiser, N. Huesing and R. J. Behm, *Catal. Lett.*, 2007, **119**, 199–208.
- 344 V. Plzak, J. Garche and R. J. Behm, *Eur. Fuel Cell News*, 2003, **10**, 8–11.
- 345 V. Schwartz, D. R. Mullins, W. F. Yan, B. Chen, S. Dai and S. H. Overbury, *J. Phys. Chem. B*, 2004, **108**, 15782–15790.
- 346 W. Yan, B. Chen, S. M. Mahurin, V. Schwartz, D. R. Mullins, A. R. Lupini, S. J. Pennycook, S. Dai and S. H. Overbury, *J. Phys. Chem. B*, 2005, **109**, 10676–10685.
- 347 B. J. Morgan and G. W. Watson, *J. Phys. Chem. C*, 2010, **114**, 2321–2328.
- 348 Z. Zheng, J. Teo, X. Chen, H. Liu, Y. Yuan, E. R. Waclawik, Z. Zhong and H. Zhu, *Chem.–Eur. J.*, 2010, **16**, 1202–1211.
- 349 Y. Denkwitz, M. Makosch, J. Geserick, U. Hörmann, S. Selve, U. Kaiser, N. Huesing and R. J. Behm, *Appl. Catal., B*, 2009, **91**, 470–480.
- 350 J. Strunk, W. C. Vining and A. T. Bell, *J. Phys. Chem. C*, 2010, **114**, 16937–16945.
- 351 H. Zhu, C. Liang, W. Yan, S. H. Overbury and S. Dai, *J. Phys. Chem. B*, 2006, **110**, 10842–10848.
- 352 C. M. Yang, P. H. Liu, Y. F. Ho, C. Y. Chiu and K. J. Chao, *Chem. Mater.*, 2003, **15**, 275–280.
- 353 S. Sundararajan, Ulm University, 2012.
- 354 C. G. Long, J. D. Gilbertson, G. Vijayaraghavan, K. J. Stevenson, C. J. Pursell and B. D. Chandler, *J. Am. Chem. Soc.*, 2008, **130**, 10103–10115.
- 355 M. Comotti, C. Della Pina, R. Matarrese and M. Rossi, *Angew. Chem.*, 2004, **116**, 5936–5939.
- 356 J. Geserick, N. Huesing, R. Rosmanith, C. K. Weiss, K. Landfester, Y. Denkwitz, R. J. Behm, U. Hörmann and U. Kaiser, *Mater. Res. Soc. Symp. Proc.*, 2007, **1007**, S04–13.
- 357 M. Comotti, C. Weidenthaler, W. C. Li and F. Schueth, *Top. Catal.*, 2007, **44**, 275–284.
- 358 F. Moreau and G. C. Bond, *Appl. Catal., A*, 2006, **302**, 110–117.
- 359 F. Moreau and G. C. Bond, *Catal. Today*, 2007, **122**, 215–221.
- 360 Y. Zhu, W. Li, Y. Zhou, X. Lu, X. Feng and Z. Yang, *Catal. Lett.*, 2009, **127**, 406–410.
- 361 A. Beck, G. Magesh, B. Kuppan, Z. Schay, O. Geszti, T. Benkó, R. P. Viswanath, P. Selvam, B. Viswanathan and L. Gucci, *Catal. Today*, 2011, **164**, 325–331.
- 362 X. Bokhimi, R. Zanella and C. Angeles-Chavez, *J. Phys. Chem. C*, 2010, **114**, 14101–14109.
- 363 M. Bandyopadhyay, O. Korsak, M. W. E. van den Berg, W. Gruenert, A. Birkner, W. Li, F. Schueth and H. Gies, *Microporous Mesoporous Mater.*, 2006, **89**, 158–163.
- 364 M. W. E. van den Berg, A. De Toni, M. Bandyopadhyay, H. Gies and W. Gruenert, *Appl. Catal., A*, 2011, **391**, 268–280.
- 365 Gold reference catalysts, *Gold Bull.*, 2003, **36**, 24–24.
- 366 C. L. Peza-Ledesma, L. Escamilla-Perea, R. Nava, B. Pawelec and J. L. G. Fierro, *Appl. Catal., A*, 2010, **375**, 37–48.
- 367 A. Beck, A. Horvath, G. Stefler, R. Katona, O. Geszti, G. Tolnai, L. F. Liotta and L. Gucci, *Catal. Today*, 2008, **139**, 180–187.
- 368 W. Yan, B. Chen, S. M. Mahurin, E. W. Hagaman, S. Dai and S. H. Overbury, *J. Phys. Chem. B*, 2004, **108**, 2793–2796.
- 369 H. Zhu, Z. Ma, S. H. Overbury and S. Dai, *Catal. Lett.*, 2008, **116**, 128–135.
- 370 Z. Ma, S. Brown, J. Y. Howe, S. H. Overbury and D. Sheng, *J. Phys. Chem. C*, 2008, **112**, 9448–9457.
- 371 A. N. Pestryakov, N. Bogdanchikova, A. Simakov, I. Tuzovskaya, F. Jentoft, M. Farias and A. Díaz, *Surf. Sci.*, 2007, **601**, 3792–3795.
- 372 S. Jafari, H. Asilian Mahabady and H. Kazemian, *Catal. Lett.*, 2009, **128**, 57–63.
- 373 J. Huang, L. C. Wang, Y. M. Liu, Y. Cao, H. Y. He and K. N. Fan, *Appl. Catal., B*, 2011, **101**, 560–569.
- 374 C. J. Jia, Y. Liu, M. Schwickardi, C. Weidenthaler, B. Spliethoff, W. Schmidt and F. Schueth, *Appl. Catal., A*, 2010, **386**, 94–100.
- 375 Z. Ma, H. Yin, S. Overbury and S. Dai, *Catal. Lett.*, 2008, **126**, 20–30.
- 376 Y. Chen, B. Zhu, M. Yao, S. Wang and S. Zhang, *Catal. Commun.*, 2010, **11**, 1003–1007.
- 377 C. Sesar, Ulm University, 2012.
- 378 Y. Denkwitz, B. Schumacher, G. Kucerova and R. J. Behm, *J. Catal.*, 2009, **267**, 78–88.
- 379 M. Ruszel, B. Grzybowska, M. Llaniecki and M. Wójtowski, *Catal. Commun.*, 2007, **8**, 1284–1286.
- 380 L. H. Chang, N. Sasirekha and Y. W. Chen, *Catal. Commun.*, 2007, **8**, 1702–1710.
- 381 I. X. Green, W. Tang, M. Neurock and J. T. Yates, *Angew. Chem., Int. Ed.*, 2011, **50**, 10186–10189.
- 382 G. B. Hoflund, S. D. Gardner, D. R. Schryer, B. T. Upchurch and E. J. Kielin, *Appl. Catal., B*, 1995, **6**, 117–126.

- 
- 383 T. A. Zepeda, A. Martinez-Hernández, R. Guil-López and B. Pawelec, *Appl. Catal., B*, 2010, **100**, 450–462.
- 384 A. Beck, A. Horvath, G. Stefler, M. Scurrell and L. Guzzi, *Top. Catal.*, 2009, **52**, 912–919.
- 385 M. Haruta, *Gold Bull.*, 2004, **37**, 27–36.
- 386 M. Haruta, *J. New Mater. Electrochem. Syst.*, 2004, **7**, 163–172.
- 387 Y. F. Yang, P. Sangeetha and Y. W. Chen, *Ind. Eng. Chem. Res.*, 2009, **48**, 10402–10407.
- 388 L. F. Liotta, G. Di Carlo, G. Pantaleo and A. M. Venezia, *Catal. Today*, 2010, **158**, 56–62.
- 389 K. Ruth, M. Hayes, R. Burch, S. Tsubota and M. Haruta, *Appl. Catal., B*, 2000, **24**, L133–L138.
- 390 M. Manzoli, A. Chiorino and F. Boccuzzi, *Appl. Catal., B*, 2004, **52**, 259–266.
- 391 T. A. Ntho, J. A. Anderson and M. S. Scurrell, *J. Catal.*, 2009, **261**, 94–100.
- 392 F. Moreau, G. C. Bond, B. van der Linden, B. A. A. Silberova and M. Makkee, *Appl. Catal., A*, 2008, **347**, 208–215.
- 393 M. C. Kung, R. J. Davis and H. H. Kung, *J. Phys. Chem. C*, 2007, **111**, 11767–11775.
- 394 L. Piccolo, H. Daly, A. Valcarcel and F. C. Meunier, *Appl. Catal., B*, 2009, **86**, 190–195.
- 395 X. Jiang, T. Herricks and Y. Xia, *Adv. Mater.*, 2003, **15**, 1205–1209.
- 396 K. Christmann, S. Schwede, S. Schubert and W. Kudernatsch, *ChemPhysChem*, 2010, **11**, 1344–1363.